MASTER OF SCIENCE THESIS

Strain Rate Dependent 3-Point Bending Test and Simulation of a Unidirectional Carbon/Epoxy Composite

Riccardo Righi

Faculty of Aerospace Engineering · Delft University of Technology

MSCCONFIDENTIAL

Strain Rate Dependent 3-Point Bending Test and Simulation of a Unidirectional Carbon/Epoxy Composite

Master of Science Thesis

For obtaining the degree of Master of Science in Aerospace Engineering
at Delft University of Technology

Riccardo Righi

20th March 2017

Faculty of Aerospace Engineering · Delft University of Technology

The work in this thesis was supported by Audi AG. Their cooperation is gratefully acknowledged.

Copyright © Riccardo Righi
All rights reserved.

Delft University of Technology
Faculty of Aerospace Engineering
Department of Aerospace Structures and Materials

GRADUATION COMMITTEE

Dated: 20th March 2017

Chair holder:

Dr. Sergio Turteltaub

Committee members:

Dr. Christos Kassapoglou

Dr. ir. Sotiris Koussios

Ing. Tobias Schmack

Merkblatt

Sperrvermerk für bei der AUDI AG erstellte Diplomarbeiten, Bachelor- und Masterarbeiten, Semesterarbeiten, Studienarbeiten

Für in deutscher Sprache verfasste Arbeiten:

Sperrvermerk

Die vorgelegte Abschlussarbeit basiert auf internen, vertraulichen Daten und Informationen des Unternehmens AUDI AG.

Die Abschlussarbeit darf nur dem Erst- und Zweitgutachter sowie befugten Mitgliedern der Prüfungsorgane zugänglich gemacht werden. Eine Veröffentlichung und Vervielfältigung der Abschlussarbeit ist – auch in Auszügen – nicht gestattet.
Eine Einsichtnahme der Arbeit durch Unbefugte bedarf einer ausdrücklichen Genehmigung durch den Verfasser und das Unternehmen.

Für in englischer Sprache verfasste Arbeiten:

Confidentiality Note

The thesis as presented is based on internal, confidential data and information of the company AUDI AG.

The thesis may only be made available to the first and second examiner as well as to authorised members of the examination boards. Publication and duplication of the thesis – including excerpts thereof – shall not be permitted.
The explicit permission of the author and the company shall be required before the thesis may be inspected by unauthorised parties.

Summary

Fibre reinforced composites have been increasingly used in the automotive industry thanks to their lightness and high specific properties, which make it possible to reduce vehicles weight. Lighter vehicles have the benefit of producing fewer emissions and therefore being less polluting. However, the crashworthiness of vehicles built with lighter materials needs to be assessed, in order to ensure passengers safety. Crashworthiness is assessed with a series of crash tests and finite element simulations performed on the full vehicle and its components. Crashes are highly dynamical events, which result in loading the structure at several strain rates. As most materials show strain rate dependency of mechanical properties, it is crucial to fully understand the strain rate effect on composites material properties so that these materials can be used in automotive production while ensuring that passengers safety standards are met.

In order to perform a finite element simulation, material cards, which contain mechanical properties of materials, have to be produced. It is important that the correct material behaviour is replicated by material cards to obtain reliable simulation results. A well-established method to calibrate the quasi-static properties of the material cards used for finite element simulations is the comparison of laboratory tests with finite element simulation results of a 3-point bending test. As crashes are highly dynamical events, material cards that take into account the strain rate effect on the material properties would be more accurate and a similar procedure for the comparison of laboratory test with finite element simulation of a strain rate dependent 3-point bending test must be undertaken to calibrate them. This study starts by reviewing the existing literature, which shows that accepted standards are not available on the strain rate dependent testing of fibre reinforced composites. An evaluation of tests such as the strain-rate dependent 3-point bending test is therefore needed to obtain reliable data, necessary to validate a material card that considers the strain-rate effect on the composite material properties.

The first aim of this thesis has been to implement a strain rate dependent 3-point bending test setup for the servo-hydraulic testing machine available at Audi AG, where the research has taken place. This has allowed obtaining reliable test results which have then been used to validate the material card. This study presents a test setup created to perform the strain-rate dependent 3-point bending tests and a simulation model created to validate material cards that take into account the strain rate dependency of the material properties of composites

materials. The fixture to perform the tests was designed and high speed cameras were used to record the experiments. This allowed obtaining test results in terms of force-midpoint displacement curves. Tests were performed using unidirectional carbon/epoxy specimens with different thickness, two different support spans and the impactor velocity up to 10 m/s. The results showed that the maximum force at failure and the maximum displacement at failure increased with increasing impactor velocity. It was also observed that after initial impact the specimen detached from the impactor, especially at high testing velocity. This event induced vibrations in the specimen and, as a result, a variation in the test results was observed. It was therefore decided to implement a Matlab tool to allow the estimation of the maximum testing velocity below which it was possible to obtain a low variation in test results, for a specific value of the specimen's global stiffness.

The second aim of the study has been to create the finite element model to simulate strain rate dependent 3-point bending tests, which has been used for the validation of material cards that consider strain rate dependent material properties. The material card for the finite element simulation was successfully modified to take into account strain rate dependent compressive properties. The 3-point bending model for the finite element simulation was able to correctly predict the increasing trend in the maximum force at failure and the maximum displacement at failure induced by the increase in the impactor velocity. However, it showed some limitations in estimating the correct value of the maximum force and maximum displacement.

In conclusion, the test setup developed allows the correct characterization of the strain rate dependent 3-point bending tests. The study also demonstrates that strain rate effects can successfully be taken into account in finite element simulations.

Acknowledgements

I have been able to work on my thesis thanks to the help and support of many people, whom I would like to thank. Firstly, I would like to thank Dr. Christos Kassapoglou for his thorough support as supervisor from the early stages until the very end of my research project. His guidance and suggestions have been invaluable to widen and deepen the analyses I have worked on for my research. I also would like to thank Ing. Tobias Schmack for his supervision and careful suggestions on how to improve my work while I was conducting the research at Audi AG and after. I have appreciated his trust in me as an intern first and then as a thesis student.

I would also like to thank the engineers at Audi AG for helpful discussions about my research on several occasions during presentations as well as during lunches at the excellent Audi AG canteen. I thank the technicians at the Audi AG laboratory for their support with the use of the testing equipment, which have helped me turn theoretical ideas into reality. Audi interns with whom I shared the office have also been a motivating and cheerful working community.

As part of my experience as a student at TU Delft, I have met fine fellow students such as Andrea Carpi, Tiago Filipe and Andrea Giordano; with whom not only I have been able to deepen my knowledge and understanding of aerospace engineering when studying together, but also to enjoy some memorable time together, to mark the beginning of what I hope will be long lasting friendships.

Finally, I would like to thank my family for their support throughout the period of my studies, from making the experience of studying and working in two different foreign countries possible, always providing day-to-day encouragement and support to fulfil my academic aspirations.

Delft, University of Technology
20th March 2017

Riccardo Righi

Table of Contents

Summary **ix**

Acknowledgements **xi**

List of Figures **xvii**

List of Tables **xx**

Nomenclature **xxiii**

1 Introduction **1**

2 Literature Review **3**

2.1 Strain Rate Dependent Behaviour in Fibre Reinforced Composites 3
  2.1.1 Tension 3
  2.1.2 Compression 5
  2.1.3 Shear 8
  2.1.4 Summary 12
2.2 Finite Element Simulation 13
  2.2.1 Material Card Calibration 13
  2.2.2 Material Card Validation 14
2.3 Composites 3-Point Bending Tests 15
  2.3.1 Quasi-static Tests 15
  2.3.2 Dynamic Tests 16
  2.3.3 Summary 20
2.4 Thesis Objective and Research Questions 21
2.5 Conclusions 22

3 Strain Rate Dependent 3-Point Bending Test 25
3.1 Testing Equipment 25
3.1.1 Instron High Strain Rate VHS 25
3.1.2 Optical Measurements 27
3.1.3 Material 29
3.2 Fixture 31
3.2.1 Design 31
3.2.2 Force Measurement System 33
3.3 Test Results 36
3.3.1 Specimen Geometry and Testing Parameters 36
3.3.2 Force Signal 37
3.3.3 Contact Impactor-Specimen 38
3.3.4 Fracture Mechanism 42
3.3.5 Maximum Force 46
3.3.6 Maximum Displacement 49
3.3.7 Coefficient of Variation 52
3.4 Conclusions 55

4 Estimation of the Maximum Testing Velocity 57
4.1 Motivation 57
4.2 Approach 59
4.2.1 Global Beam Stiffness 59
4.2.2 Linear Regression of the Force-Displacement Curve 61
4.3 Coefficient of Determination - R^2 62
4.4 Maximum Allowed Testing Velocity 65
4.5 Matlab Graphical User Interface 72
4.6 Conclusions 74

5 Finite Element Simulation 75
5.1 Introduction 75
5.2 Strain Rate Dependent Model in PAM-CRASH 76
5.2.1 Choice of the Ply Model Type 78
5.3 Strain Rate Dependent Compressive Properties 80
5.3.1 Compressive Strain 81
5.4 Calibration of the Strain Rate Properties 85
5.5 3-Point-Bending Simulation Model 88
5.5.1 Maximum Force 90
5.5.2 Maximum Displacement 90
5.5.3 Comparison with Test Results 93
5.6 Conclusions 94

6 Conclusions and Recommendations 97
6.1 Conclusions 97
6.2 Recommendations 99

References 101

Fixture Calibration 105

Strain Rate Computation 111

List of Figures

2.1 Longitudinal tensile stress vs. strain curve for UD carbon/epoxy composites at quasi-static and high strain rates [7]. 4

2.2 Transverse tensile stress vs. strain curve for UD carbon/epoxy composites at quasi-static and high strain rates [8]. 5

2.3 Longitudinal (a) and transverse (b) strain rate compressive behaviour [10]. 6

2.4 Longitudinal (a) and transverse (b) strain rate compressive behaviour [12]. 7

2.5 Longitudinal compressive strength tested in combination of shear and uniaxial load (fixture A) and pure uniaxial load (fixture B) condition [14]. 8

2.6 In-plane shear stress vs. strain curves for $30°$ and $45°$ off-axis specimens [10]. . . 9

2.7 In-plane shear stress vs. strain curves $15°$, $30°$, $45°$ and $60°$ off-axis specimens [15]. 10

2.8 Tensile stress vs. strain curves for ± 45 M7/977-2 carbon/epoxy [8]. 11

2.9 Strain rate effect on in-plane shear properties [7]. 11

2.10 Stress vs. strain for tension and compression tests for quasi-static (a) and high (b) strain rate tests [17]. 12

2.11 Material calibration for tension (a) and compression (b) [18]. 14

2.12 3-point bending validation [26]. 15

2.13 Drop weight tower setup [35]. 17

2.14 Load vs. displacement curve for impact (a) and quasi-static (b) tests [35]. 18

2.15 Pressure gun apparatus for 3-point bending impact [37]. 19

2.16 Force vs. displacement curves for $0°$-specimen tested with 50mm (a) and 30mm (b) support span [38]. 20

3.1 Servo-hydraulic testing machine [39]. 26

3.2 Example of calibration curve. 27
3.3 Test setup (a) and cameras measuring volume (b). 28
3.4 Signal processing on the testing machine. 29
3.5 Positions for thickness (a) and fibre volume (b) measurements. 30
3.6 3-point bending setup [31]. 31
3.7 Fixture design. 33
3.8 Impactor and supports details. 34
3.9 Quarter Wheatstone bridge configuration. 34
3.10 Fixture signal processing. 35
3.11 Specimens geometry. 36
3.12 Filtered force signal. 38
3.13 Comparison between impactor and specimen midpoint displacement for $4\,\mathrm{mm}$ thick specimen with geometry A. 39
3.14 Impactor displacement vs. specimen midpoint displacement for specimen geometry A. 40
3.15 Impactor displacement vs. specimen midpoint displacement for specimen geometry B. 41
3.16 Failure mechanism of mid-range thickness specimens. 43
3.17 Failure mechanism of thick specimens. 44
3.18 Maximum force. 47
3.19 Normalised maximum force. 48
3.20 Maximum displacement. 50
3.21 Specimen displacement vs. testing velocity. 51
3.22 Coefficient of variation of the maximum force (a, b) and maximum displacement (c, d) at failure 53
3.23 Mean values of the coefficient of variation of the maximum force (a) and maximum displacement (b) at failure for the testing velocities common to both support spans. 54
3.24 Mean values of all the coefficient of variation of the maximum force (a) and maximum displacement (b) at failure for the testing velocities common to both support spans. 54

4.1 Variation of the CV of the maximum force at failure (a) and R^2 (b) according to the testing velocity for tests performed with the support span of $80\,\mathrm{mm}$. 58
4.2 Variation of the CV of the maximum force at failure (a) and R^2 (b) according to the testing velocity for tests performed with the support span of $60\,\mathrm{mm}$. 58
4.3 Simply supported beam. 59

4.4 Deformed simply supported beam. 60
4.5 Support span= $80\,\mathrm{mm}$ 61
4.6 Effect of the testing velocity and the thickness on R^2 62
4.7 R^2-specimen thickness relation for support span of (a) $80\,\mathrm{mm}$ and (b) $60\,\mathrm{mm}$. . 63
4.8 Effect of the support span on R^2. 64
4.9 Effect of the testing velocity on R^2. 64
4.10 Fitting curves for prediction of the maximum allowed testing velocity 66
4.11 Fitting curves for tests performed with the support span of (a) $80\,\mathrm{mm}$ and (b) $60\,\mathrm{mm}$. 67
4.12 Fitting curves for tests performed with the support span of $60\,\mathrm{mm}$. 68
4.13 Estimation of the maximum testing velocity for $R^2 = 0.95$. 69
4.14 Fitting curves for the estimation of the maximum allowed testing velocity for a specific specimen global stiffness value. 69
4.15 Fitting curves for prediction of the maximum allowed testing velocity depending on the specimen global stiffness for the support span of $60\,\mathrm{mm}$ at $R^2 = 0.95$. . . 70
4.16 Estimated maximum testing velocity for (a) $R^2 = 0.95$ and (b) $R^2 = 0.97$. . . . 71
4.17 Matlab graphical user interface. 72
4.18 Output of the Matlab GUI. 73

5.1 AUDI R8 e-tron body [39]. 76
5.2 Compression test results. 81
5.3 Compression test results used to determine the strain rate fitting law for the PAM-CRASH material card. 82
5.4 Interpolation of the compressive fracture strain. 84
5.5 Neperian logarithmic law used to fit the test results in (a) logarithmic and (b) normal scale x-axis. 84
5.6 Single element calibration model. 86
5.7 Effect of the initial and ultimate failure strain on the single element calibration model. 86
5.8 Stress-strain curves of the single element calibration model 87
5.9 Comparison of the compressive fracture strain and strength between the simulation and the test results. 87
5.10 The 3PB simulation model implemented. 89
5.11 Python code for the parametric model. 90
5.12 Maximum force from the 3PB simulation model. 91
5.13 Maximum displacement from the 3PB simulation model. 92

5.14 Relative error between simulation and test results for the maximum force. 93
5.15 Relative error between simulation and test results for the maximum displacement. 94

1 Force-time response for the fixture impactor and the Zwick testing machine. . . . 106

2 Strain rate computed from the ARAMIS analysis. 113
3 Strain rate computed from the analytical analysis. 114

List of Tables

2.1 Mechanical properties obtainable from 3-point bending tests [34]. 16

3.1 Average measurements for plate thickness and fibre volume. 30
3.2 Impactor and supports radius dimensions [31]. 32
3.3 Testing configurations. 37
3.4 Specimen failure mechanism. 45

4.1 Simply supported beam global stiffness. 65

5.1 Advantages and disadvantages for Ply Model Type 1 and 7. 79
5.2 Strain rate compression test results. 82
5.3 Strain rate parameter analysis for UD compression tests. 83
5.4 Coefficients for the fitting laws. 84
5.5 Single element calibration model boundary conditions. 86
5.6 Comparison of test results and material card calibration. 88

1 Fixtures parameters for force measurements. 106
2 Example of calibration table for the impactor fixture. 108

Nomenclature

List of Symbols

Acronyms

CO_2	Carbon dioxide	
3PB	3-point bending	
CBT	Classical beam theory	
CD	Coefficient of determination	
CFRP	Carbon fibre reinforced plastic	
CV	Coefficient of variation	
DIC	Digital image correlation	
FE	Finite element	
FEA	Finite element analysis	
FRC	Fibre reinforced composite	
GUI	Graphical user interface	
LVDT	Linear variable differential transducer	
RGB	Red-green-blue	
SHPB	Split Hopkinson's pressure bar	
UD	Unidirectional	
Greek Symbols		
$\dot{\varepsilon}$	Strain rate	[s^{-1}]
$\dot{\varepsilon}_{11}^{ref}$	Reference strain rate in fibre direction	[s^{-1}]
$\dot{\varepsilon}_{ij}^{ref}$	Reference strain rate	[s^{-1}]
$\dot{\varepsilon}_{qs}$	Quasi-static strain rate	[s^{-1}]
ν_{21}	Poisson's ratio	[$-$]
σ	Stress	[MPa]
σ_{ij}	Stress in the laminate direction	[MPa]

ε	Strain	[−]
ε^{e}_{ij}	Elastic strain in the laminate direction	[−]
ε^{fc}_{qs}	Quasi-static fracture strain	[s^{-1}]
ε^{fc}_{ref}	Reference fracture strain	[−]
ε^{ref}_{11}	Reference fracture strain in fibre direction	[−]

Latin Symbols

$\bar{y}$	Average test force	[N]
$(EI)_{beam}$	Beam stiffness	[Nmm^2]
ln()	Natural logarithm	[−]
A	Fixture necking area	[mm^2]
a, b, c, d	Coefficients for the exponential interpolation law	[−]
A_{WB}	Wheatstone bridge amplification factor	[−]
B	Bridge factor	[−]
b	Width	[mm]
b_r	Relative repeatability	[%]
C_{ij}	ij^{th} entry of the strain rate dependent stiffness matrix	[−]
d	Distance from neutral axis	[mm]
D^{R}_{11}	First coefficient for the fracture strain fitting law	[−]
D_{ij}	First coefficient for PAM-CRASH strain rate fitting law	[−]
d_{ij}	Damage coefficient	[−]
E	Young's modulus	[MPa]
F	Force	[N]
$f(x)$	Exponential interpolation law	[−]
f_i	Test force at point i	[N]
F_Z	Zwick universal testing machine measured force	[N]
F^{R}_{11}	Viscosity function for the fracture strain	[−]
F_{fixt}	Fixture force	[N]
F_{ij}	Viscosity function	[−]
F_{max}	Maximum force at the specimen midpoint	[N]
G_{ij}	Shear modulus	[MPa]
h	Specimen thickness	[mm]
k	Gauge factor	[−]
K_{beam}	Beam global stiffness	[N/mm]
L	Support span	[mm]
m	Linear regression slope	[N/mm]
n^{R}_{11}	Second coefficient for the fracture strain fitting law	[−]
n_{ij}	Second coefficient for PAM-CRASH strain rate fitting law	[−]
$p(x)$	Polynomial interpolation law	[−]
p_n	Coefficients for the polynomial interpolation law	[−]
q	Relative indication error	[%]

R	Resistance	[Ω]
R^2	Coefficient of determination	[−]
R_1	Impactor radius	[mm]
R_2	Support radius	[mm]
S	Conversion factor	[N/V]
S_{calib}	Calibrated conversion factor	[N/V]
sf	Scaling factor	[−]
SS_{res}	Residual sum of squares	[N^2]
SS_{tot}	Total sum of squares	[N^2]
t	Time	[s]
U_{in}	Input voltage	[V]
U_{out}	Output voltage	[V]
v	Velocity	[mm/s]
w	Specimen midpoint displacement	[mm]
y_i	Linear regression force at point i	[N]

Chapter 1

Introduction

Emission requirements for car exhaust gases are becoming more and more rigid. According to the European Commission [1], cars are responsible for the production of approximately 12% of the European Union emissions of carbon dioxide (CO_2), the main greenhouse gas. The European Union has set emission reduction targets for new cars. The target for 2021 is that the fleet average of CO_2 emissions to be achieved by all new cars is 95 grams per kilometre. This has driven the automotive industry to research and design lightweight car components in order to reduce emissions of the vehicles they produce.

The need for weight reduction has led to an increase in the use of Fibre Reinforced Composites (FRC), in particular in the use of Carbon Fibre Reinforced Plastics (CFRPs). These materials have high specific properties that allow a lighter design, compared to other metal components. Therefore, by using CFRP it is possible to obtain weight reduction that results in lower exhaust gas emissions.

The ability to withstand dynamic loading is a very important criterion for automotive vehicle design. Vehicles must ensure passengers' safety by withstanding crashes and to this purpose they are tested according to international standards. One example is the Euro NCAP [2], which determines vehicle safety through a series of tests, such as the front and side crash test. Crashworthiness of composite structures and components is a critical criterion in the design of automotive vehicles. During crashes vehicles are subjected to highly dynamical loading and are designed to absorb the impact energy through dynamic damage and fracture mechanisms. It is known that for most materials the mechanical properties are strain rate dependent. As highly dynamical loading experienced by structures during crashes results in loading them at several strain rates and composite material are replacing metallic structures, it is important to fully understand the effect of the strain rate on the composite materials behaviour.

Finite element analysis are also used to asses the vehicle crashing performance and determine improvements that can be done in the vehicle design. An important step in these analysis is to correctly model the behaviour of the materials used. To this purpose material cards are calibrated and validated by comparing the results from simple simulation model with coupon test results. Comparing the simulation and test results of a 3-point bending (3PB) test is the method employed for validating material cards. This method is well established when considering quasi-static mechanical properties, but it must be performed also when strain rate dependency is taken into account in the material cards.

The research conducted during this thesis has been carried out in collaboration with Audi AG. It deals with the improvement of the material card used for the simulation of carbon fibre composites by taking into account the strain rate effect on material properties. In particular, the test setup for dynamic 3-point bending tests and the simulation model to validate the new material card are the two topics of this research.

Chapter 2 presents a review of the literature, the thesis objective and the two research questions. Chapter 3 addresses the first research question and presents the strain rate dependent 3-point bending tests. Chapter 4 describes the method developed to estimate the maximum testing velocity, below which low variation in the test results is expected. Chapter 5 addresses the second research question, and presents the single element calibration model and the strain rate dependent 3-point bending simulation model. Finally, Chapter 6 draws the conclusions of the research and outlines the recommendations for future work.

Chapter 2

Literature Review

In this chapter the literature reviewed for this thesis is presented. Section 2.1 presents the tensile, compressive and shear strain rate behaviour of unidirectional (UD) carbon/epoxy composites, Section 2.2 shows the methods used to calibrate and validate material cards for finite element (FE) simulations, in Section 2.3 the current state of the art for strain rate dependent 3-point bending tests is presented. The thesis objective and the research questions are discussed in Section 2.4. Finally the conclusion based on the content of this chapter are drawn in Section 2.5.

2.1 Strain Rate Dependent Behaviour in Fibre Reinforced Composites

To characterise the mechanical properties of materials it is necessary to perform a series of tests, and this is an intensive and time consuming process [3]. Fibre Reinforced Composites are anisotropic materials and their properties can depend on several factors, such as moisture, temperature, and strain rate. For this reason, to fully characterise them, a very high number of tests are required. Material characterisation of quasi-static properties have been widely studied in literature and international standards, such as the ISO and ASTM standards, have already been developed. Differently, strain rate dependent material characterisation is still under investigation and standards have not been developed yet. This section reviews the current status of strain rate dependent characterisation of composites material properties. The focus is on the studies of UD composite materials, with a particular emphasis on carbon/epoxy composites.

2.1.1 Tension

In the study of the strain rate dependent tensile properties of composite material, Harding and Welsh [4] were among the first to obtain successful results on the topic. They used a modified version of the tensile split Hopkinson's pressure bar (SHPB) and were able to test

UD carbon/epoxy composites at high strain rates. They discovered that there is no significant strain rate dependency in the longitudinal tensile properties. This is probably because carbon fibre is strain rate insensitive under tensile loading [5, 6]. Zhou et al. [5] demonstrated that T300 and M40S carbon fibre bundles do not show any strain rate effect on the tensile initial elastic modulus, ultimate strength, and fracture strain.

Taniguchi et al. [7] also studied the tensile properties of carbon/epoxy composites in the longitudinal and transverse direction at high strain rates using a split Hopkinson bar. Test results at high strain rate were compared with the quasi-static results, performed with a universal testing machine. In the longitudinal direction, there is no strain rate effect on the strength, as well as on the tensile modulus, in agreement with the observations made by Harding and Welsh. A typical longitudinal tensile behaviour of carbon/epoxy composites at different strain rates is shown in Figure 2.1.

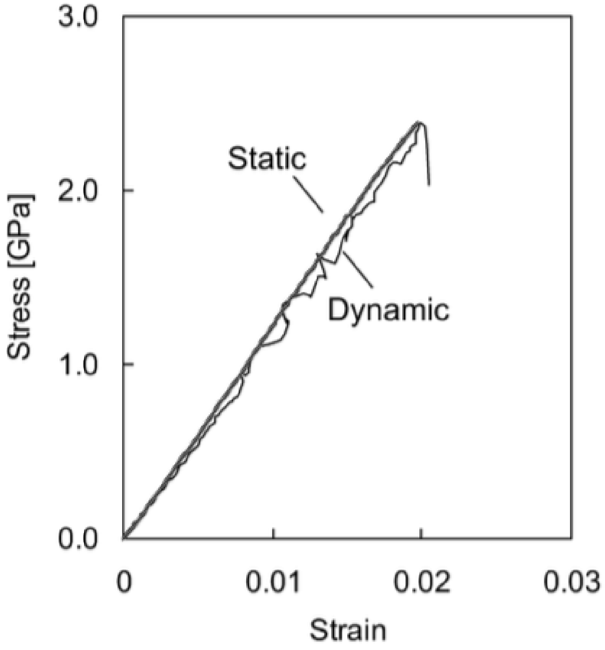

Figure 2.1: Longitudinal tensile stress vs. strain curve for UD carbon/epoxy composites at quasi-static and high strain rates [7].

Gilat et al. [8] performed a study on the transverse tensile properties of IM7/977-2 carbon/epoxy composites. They performed tests at quasi-static (approximately 5×10^{-5} s^{-1}) and moderate (approximately 1 s^{-1}) strain rate using a hydraulic Instron testing machine, while tests at high strain rates (approximately $400 - 600$ s^{-1}) were performed using a tensile split Hopkinson bar. Specimens with the same geometry were used in all the tests, this was done to avoid uncertainties due to size effects. The test results showed that the stress-strain curves for quasi-static and moderate strain rates are almost identical and show a linear behaviour. At high strain rates the curves become non-linear, a higher fracture stress is achieved, and a higher stiffness is measured. This can be seen in Figure 2.2 below.

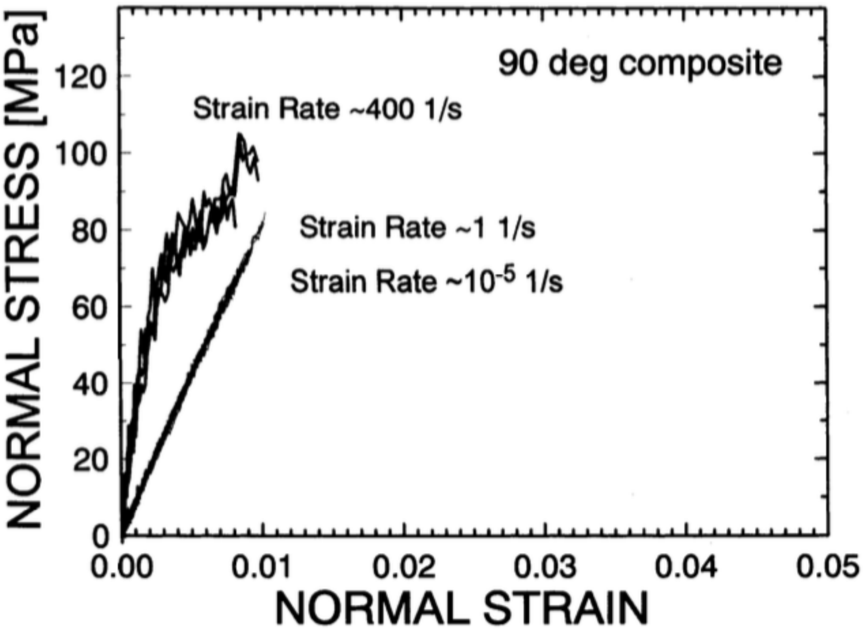

Figure 2.2: Transverse tensile stress vs. strain curve for UD carbon/epoxy composites at quasi-static and high strain rates [8].

A study on transverse tensile properties was also performed by Taniguchi et al. [7]. It was observed that the modulus and strength increase with increasing strain rate. Compared to the quasi-static properties, at high strain rate the transverse modulus increased by 12.5%, while the strength increased by 17.8%. In both studies [7, 8] the failure strain was not affected by the strain rate.

2.1.2 Compression

Composites compressive properties in the longitudinal and transverse direction are affected by the matrix behaviour [9]. It has been shown that the strain rate influences the properties of the polymeric resin, which constitutes a composite material [8]. For this reason, composites in-plane compressive properties have been studied with more consideration and it is possible to find different studies in literature.

Hsiao and Daniel [10, 11] studied the longitudinal and transverse compressive behaviour from low to high strain rates. Tests at a strain rate below 10^{-1} s^{-1} were performed using a hydraulic testing machine, while for tests above 10^{-1} s^{-1} strain rate a drop tower apparatus was used [10]. For strain rates above 500 s^{-1} a SHPB was used. The material tested was the IM6G/3501-6 carbon/epoxy. Comparing the strain rate dependent test results with the quasi-static ones in the longitudinal direction (Figure 2.3a) has shown that the initial modulus increases slightly with the strain rate. Furthermore, at the highest strain rate the strength and the ultimate strain increased 79% and 74% respectively [10].

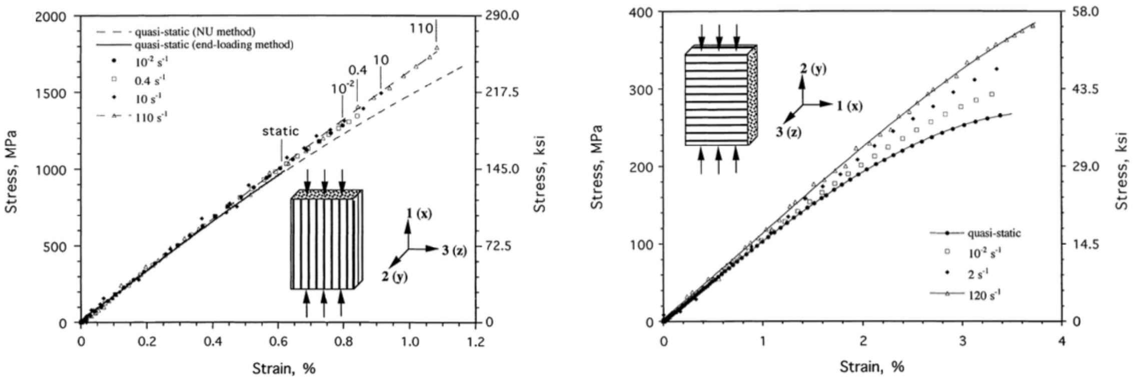

(a) **(b)**

Figure 2.3: Longitudinal (a) and transverse (b) strain rate compressive behaviour [10].

The transverse compressive properties showed a significant strain rate effect [11]. The peak stress was always increasing with the increase of the strain rate. At the highest strain rate of 1800 s^{-1} the initial stiffness increased by 37%, while the strength was nearly twice as much as the quasi-static one. No strain rate effect was measured on the fracture strain.

Hosur et al. [12] used a modified split Hopkinson pressure bar to perform compressive tests at three strain rates, respectively 82, 164 and 827 s^{-1}. The material used was the Panex 33/DA 4518U carbon/epoxy. The unidirectional layup was cured in a compression mould, and small cubic specimens were cut using a diamond saw. Both longitudinal and transverse to fibre tests were performed. Tests in the longitudinal direction showed material stiffening for specimen tested at the three strain rates, compared to the quasi-static behaviour. On the other hand, the stiffening effect slightly reduced at the higher strain rates, as shown in Figure 2.4a. This is in contrast with the findings of Hsiao et al. [11], and it is said to be due to the matrix viscoelastic nature and to the effect of failure modes. The major failure modes observed were shear failure and fragmentation. These failure modes differ form the typical fibre kinking and microbucling observed when testing relatively long rectangular specimens [10, 11, 13, 14] The peak stress was always increasing with the increase of strain rate.

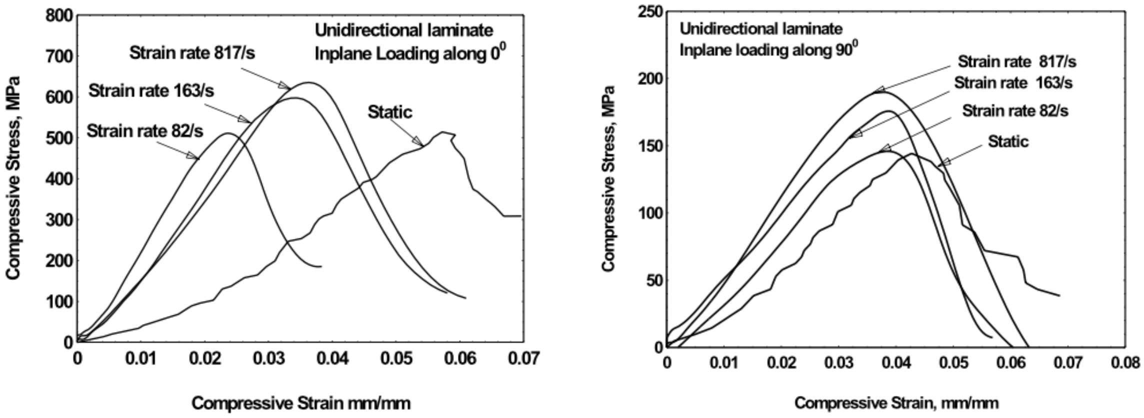

(a) (b)

Figure 2.4: Longitudinal (a) and transverse (b) strain rate compressive behaviour [12].

The compressive behaviour in the transverse direction is shown in Figure 2.4b. For UD composites the transverse behaviour is completely matrix dominated and both the stiffness and the peak stress increase with the increase of the strain rate.

Koerber and Camanho [13] studied the strain rate effect on the longitudinal compressive properties carbon/epoxy IM7-8552 composite. A specific fixture was developed in order to test flat rectangular specimens using the SHPB. The fixture designed allowed to test the specimens under uniaxial load conditions. Dynamic tests were performed at a strain rate of approximately 100 s^{-1}. The results showed that the compressive strength increased by approximately 40%, while the longitudinal compressive modulus did not show dependency on the strain rate. In this study the longitudinal compressive modulus was computed between the range 1000$\mu\varepsilon$ and 3000$\mu\varepsilon$, as stated in the quasi-static norm ASTM D 3410.
The strain rate characterisation of transverse compressive properties of carbon/epoxy IM7-8552 composite was performed by Koerber et al. [15]. Tests at strain rates up to 350 s^{-1} were performed on the SHPB. In this study, tests were recorded using a Photron SA5 high speed camera. For this reason specimens were sprayed using a grey-scale stochastic pattern, making possible to use Digital Image Correlation (DIC) to measure the strain distribution over the whole specimens surface. It was observed a slight increase of 12% in compressive modulus and a considerable increase in yield strength (where yield was defined as 0.02% plastic axial strain) and compressive strength, respectively 83% and 45%. These results are consistent with the ones obtained by Hsiao et al. [11].

In a recent study performed by Schmack et al. [14], the influence of the specimen geometry and the load introduction method on strain rate compressive properties was investigated. The material used is the carbon/epoxy T700-DT120, the plates from which the specimens have been cut were manufactured using the vacuumbag and autoclave method. Longitudinal compressive tests up to strain rates of about 100 s^{-1} were performed using a servo-hydraulic testing machine. Two different fixtures were used. One fixture allowed load introduction in the specimen through a combination of shear and uniaxial load (fixture A), while the other fixture allowed only uniaxial load (fixture B) condition. Each fixture was designed for a specific specimen geometry. Therefore, the two specimen geometries are different in terms of length, width, and thickness (specimen A: 90 × 20 × 3.2mm, and specimen B: 75 × 15 × 2mm). Glass fibre tabs were also glued on the specimens, so another geometry parameter was the gauge length. To measure the strain, the digital image correlation method was used for specimen A, while for specimen B strain gauges were bonded in the specimen gauge areas.

The results obtained in the study performed by Schmack et al. [14] are shown in Figure 2.5. In general, the longitudinal compressive strength was found to increase with increasing strain rate. This result is consistent with previous studies [10, 13]. When testing specimen geometry A in fixture A, the compressive strength increases up to strain rate of 1.37 s^{-1}. At the strain rate of 3.5 s^{-1}, it dropped by approximately 17%, for this reason specimens with geometry B have been tested in fixture A at approximately the same strain rate. In this case no drop in compressive strength was measured. The reason to these two different behaviours is said to be due to a smaller gauge length, which affects the specimen local and global buckling. The longitudinal compressive initial modulus shows a high variance, therefore it is inferred by the authors that there is no significant influence on it due to strain rates.

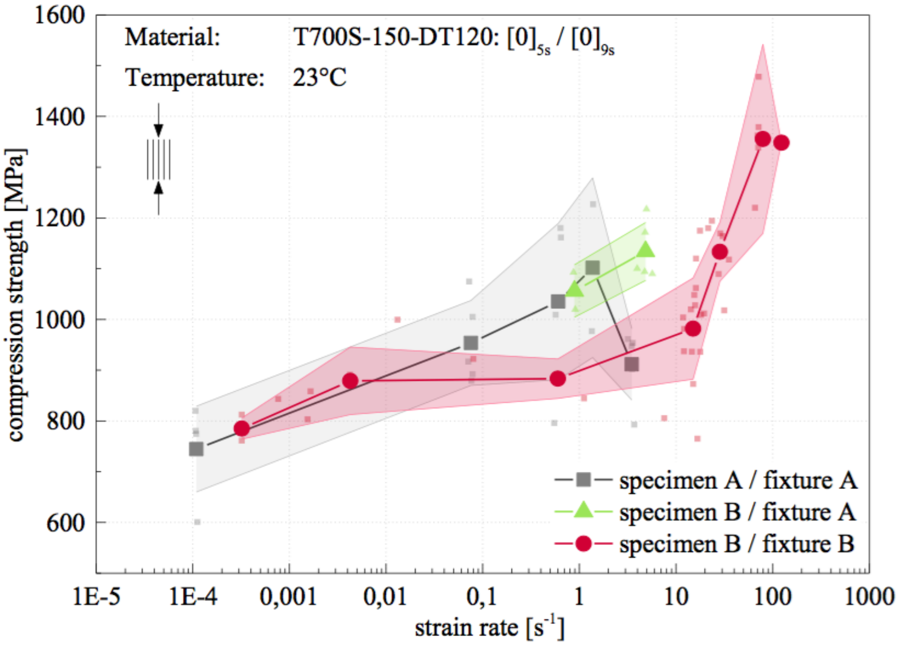

Figure 2.5: Longitudinal compressive strength tested in combination of shear and uniaxial load (fixture A) and pure uniaxial load (fixture B) condition [14].

2.1.3 Shear

Shear properties are strongly influenced by matrix properties [9]. It has been shown in section 2.1.2 that compressive properties of composites -which are affected by matrix behaviour- are sensitive to the strain rate. Therefore, it is expected that also shear properties of composite materials are strain rate dependent. Studies that investigate the effect of the strain rate on composites shear properties are numerous. It has been found in literature that two methods are generally used to characterise shear properties, both for quasi-static and strain rate dependant. One method extrapolates shear properties from off-axis compression tests [10, 15, 16]. The second method obtains shear properties from tensile tests of specimens with ±45° layup [7, 8, 17].

Shear Properties from Off-axis Compression

Hsiao and Daniel [10], besides studying the strain rate compressive behaviour of carbon/epoxy composites, also investigated the strain rate effect on shear properties by means of off-axis compression tests. They used 30° and 45° off-axis specimens, and performed the tests using a drop tower apparatus.
Test results are shown in Figure 2.6. The stress vs. strain curves obtained from the two off-axis angles are non-linear and comparable in the all strain rate range tested, from quasi-static to high strain rates. Compared to quasi-static results, the initial modulus, the yield stress, and the shear strength increased with increasing strain rate. At the highest strain rate the initial modulus increases by 18%, while the shear strength rises by 80%. On the other end, the shear strain decreases with increasing strain rate.

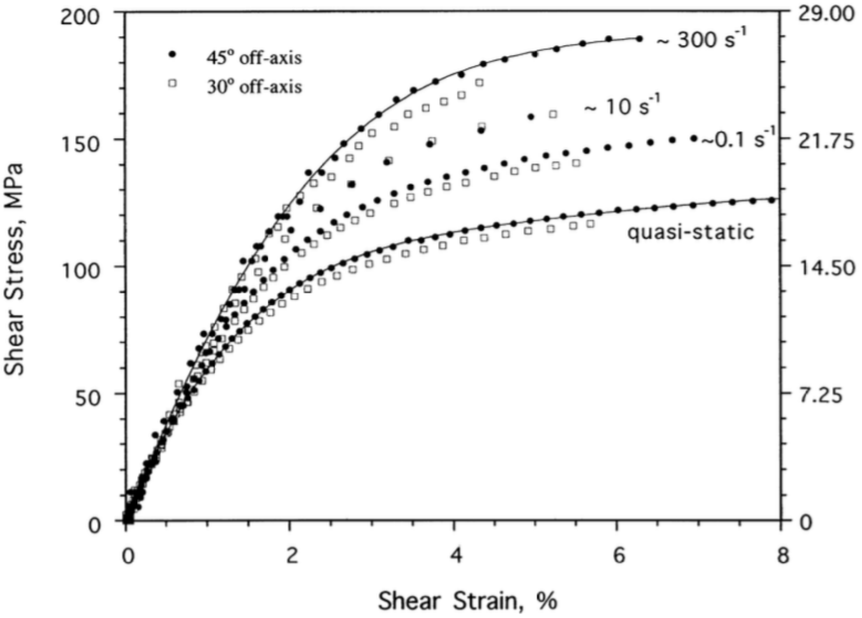

Figure 2.6: In-plane shear stress vs. strain curves for 30° and 45° off-axis specimens [10].

Koerber et al. [15] obtained in-plane shear stress vs. strain data from 15°, 30°, 45° and 60° off-axis compression test. By transforming the stress and strain measured from the global coordinate system into the specimen coordinate system, the authors were able to obtain the in-plane shear response, which is shown in Figure 2.7. The curves show a similar behaviour compared with the results obtained by Hsiao and Daniel [10]. When comparing the two strain rate regimes analysed, the in-plane shear modulus increased by 25%, whilst the in-plane shear yield strength increased by 88%. These two properties were obtained from the 45° off-axis specimens. The shear strength was instead computed from the 15° and 30° off-axis specimens that failed in in-plane shear mode. The shear strength from dynamic tests increased by 42% compared to the quasi-static one. The increase in shear strength is smaller compared with the one obtained by Hsiao and Daniel [10].

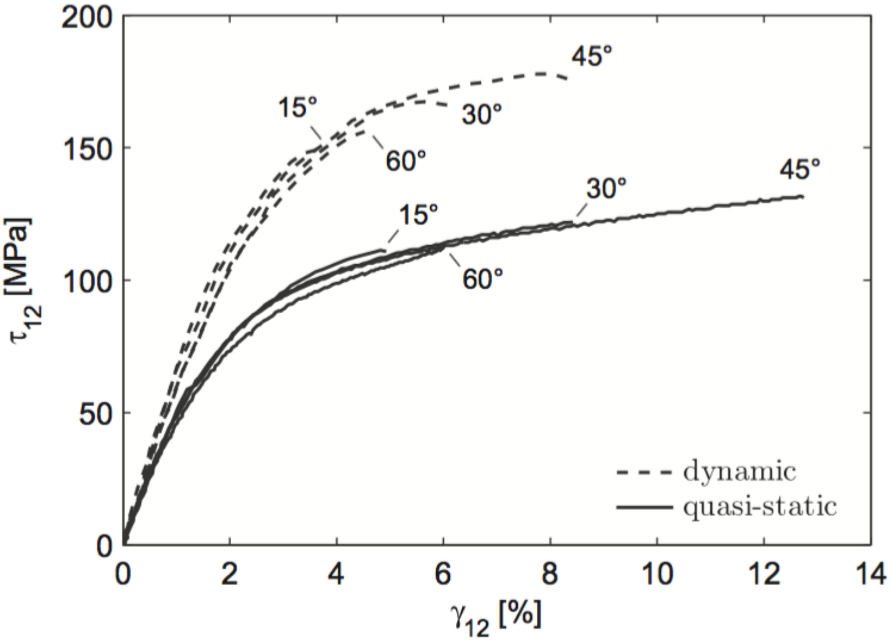

Figure 2.7: In-plane shear stress vs. strain curves 15°, 30°, 45° and 60° off-axis specimens [15].

Daniel et al. [16] investigated the off-axis shear properties of a carbon/epoxy composite AS4/3501-6. A servo-hydraulic testing machine was used to perform tests at quasi-static and average strain rates, and a split Hopkinson bar for tests at high strain rates. Shear properties were obtained from 15°, 30°, 45° and 60° off-axis compression tests. It was found that both the in-plane shear modulus and strength increased linearly with the logarithm of the strain rate.

Shear Properties from ±45° Tension

The results obtained by Gilat et al. [8] are shown in Figure 2.8. Tests at quasi-static and moderate strain rate were performed using an hydraulic testing machine, while tests at high strain rates were performed using a tensile split Hopkinson bar. From the plot, it is possible to see that, at the quasi-static and average strain rates, initial stiffness are equal. The initial stiffness then increases at the high strain rate. The curves for average strain rates show a higher yield stress compared to the quasi-static ones. In general, it is possible to say that both the yield stress and the fracture stress increase with increasing strain rate. This material behaviour displayed and described shows a typical strain rate dependent behaviour.

Taniguchi et al. [7] performed tests at a strain rate of approximately 100 s^{-1} using a tension split Hopkinson bar and carbon/epoxy specimens. The in-plane shear modulus and strength highly increased, both by approximately 77%, compared to quasi-static values. Nonetheless, the shear strain decreased for tests at 100 s^{-1} strain rate, as shown in Figure 2.9.

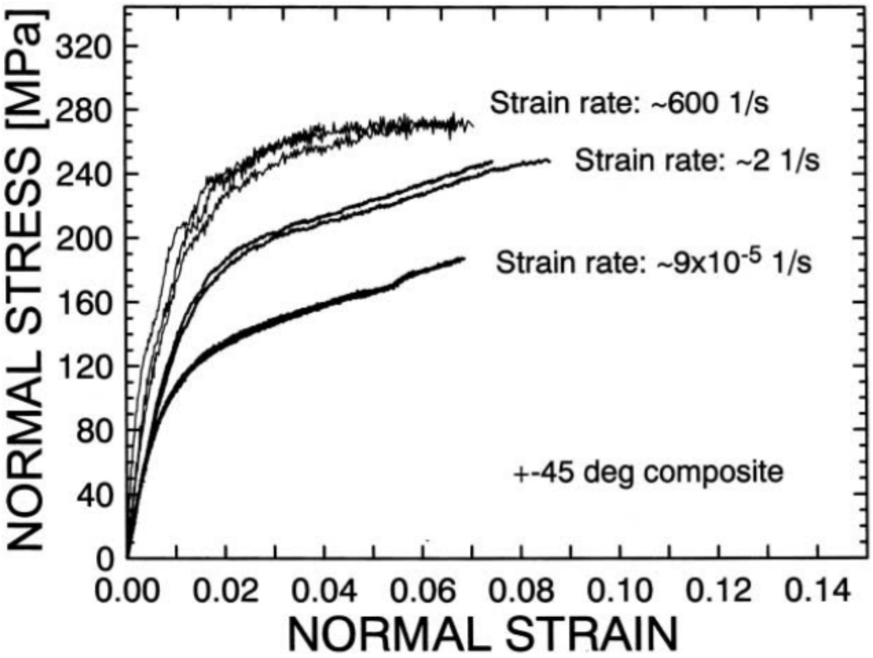

Figure 2.8: Tensile stress vs. strain curves for ±45 M7/977-2 carbon/epoxy [8].

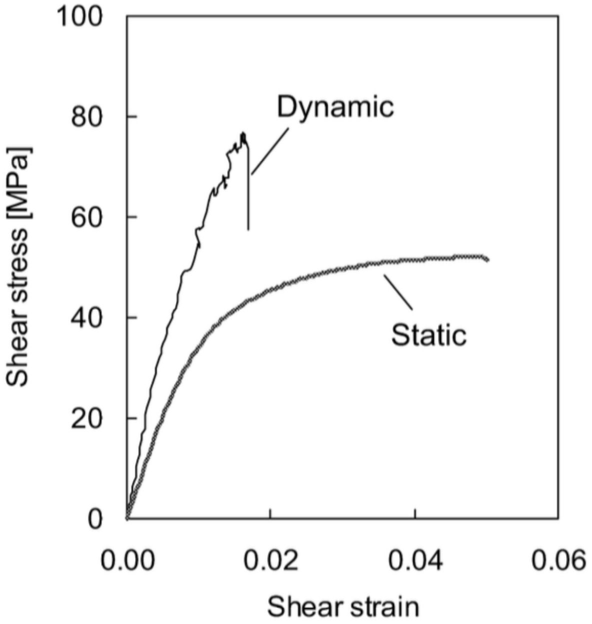

Figure 2.9: Strain rate effect on in-plane shear properties [7].

In a recent study, Cui et al. [17] performed strain rate dependent tensile and compressive tests on ±45 carbon/epoxy composite IM7/8552. Quasi-static tests were performed on a screw driven testing machine, while strain rate dependent tests at 1300 s^{-1} were performed on a split Hopkinson tension and compression bar system. The stress vs. strain curves obtained are shown in Figure 2.10. The shear stiffness and yield strength increases with increasing strain rate, while the fracture strain decreases. At quasi-static rate the material shows a strengthening behaviour after yield, as observed by previous studies [7, 8]. However, at high strain rates softening is observed after the elastic phase. This softening nature was not observed in previous studies, a reason could be that the strain rate considered by Cui et al. is much higher compared with the other studies.

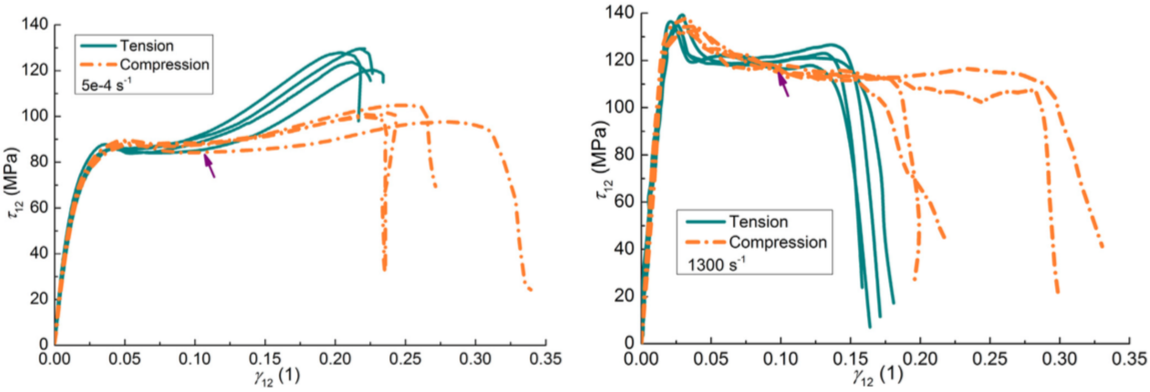

(a) (b)

Figure 2.10: Stress vs. strain for tension and compression tests for quasi-static (a) and high (b) strain rate tests [17].

Of high interest is the comparison made by Cui et al. between the stress vs. strain curves obtained using tensile and compressive tests to obtain shear properties. The results show that the tension and compression curves are very similar up to values of strain close to 10%. After this point the curves move away from each other. Furthermore, at quasi-static rates the hardening process is stronger for specimens tested in tension.

2.1.4 Summary

In this section, the strain rate effect on CFRPs mechanical properties has been described by reviewing the studies available in literature. The focus has been on UD carbon/epoxy composites, as such a material has been used in this research. Strain rate dependency is seen in material properties that are affected by the polymeric matrix [8, 9]. For this reason longitudinal tensile properties do not show strain rate dependency [4, 7]. Longitudinal tension is governed by the fibre behaviour, which in case of carbon fibre is insensitive to the strain rate [5, 6]. Due to this fact, researchers have focused more on determining the influence of the strain rate on compressive and shear properties.

Concerning longitudinal compressive properties, Hosur et al. [12] reported a strain rate dependency of the compressive modulus, in contradiction with the other studies analysed. All studies reported an increase in ultimate strength. However, the load introduction method and the specimen geometry highly affects the outcomes of the tests [14].

In-shear properties can be obtained through two types of tests: off-axis compression and tensile tests on ±45 laminates. In general, it was observed that the initial modulus and the shear strength increased with increasing strain rate. As shown in figure 2.7, the fibre orientation angle strongly affects the shear strength. Therefore, shear properties are normally obtained from specimens with a fibre angle of 30 ° or 45 °. For both methods, in order to obtain the material properties of interest it is first required to transform the stresses and strains from the global to the specimen coordinate system. As shown by Cui et al. [17], both tests are suited to obtain the in-plane shear properties up to strain values of 10%, as shown in Figure 2.10.

To determine strain rate dependent properties of materials servo-hydraulic testing machines, drop towers, or split Hopkinson's pressure bars are used to perform tests. These test setups are suited to study the strain rate dependent behaviour of CFRPs. They allow obtaining stress-strain curves from which the properties of interest are derived, although for shear properties transformations are required to obtain the stresses and strains in the specimen coordinate system. On the other hand, test results are strongly affected by some test parameters such as the specimen geometry or the method used to introduce the load in the specimen. Further investigation on the influence of testing parameters would be needed to better understand the strain rate effect on composite properties.

2.2 Finite Element Simulation

The Finite Element Analysis (FEA) is a widely used method in the industries, such as in the automotive and the aerospace sector, to assess components [18–20] and full-structures [21, 22] crashing performance under critical loading conditions. In the design of a structure, finite element analysis can be used as a step to assess its performances and determine the improvements that can be done in the design before manufacturing a full scale model for testing [23]. In order to obtain trustworthy results form simulation of structures and components, it is important to have reliable material models and material cards [18, 20–22, 24–26].
Several finite element software codes are available in commerce which allow the user to perform the analysis required. In this section, the process which is used to calibrate and validate material cards for finite element simulation will be reviewed. Particular attention will be paid to the procedure used for UD composite materials in the finite element software PAM-CRASH, as this is the software which has been used for FEAs in the thesis.

2.2.1 Material Card Calibration

In a finite element software, the material card is the segment where all the properties of the material used during a simulation are given as an input. A material is characterised by several types of properties, for example mechanical, thermal, acoustic, etc. However, only the calibration of mechanical properties will be considered hereafter, because they are the ones of interest.

The procedure to calibrate the material card is shown in references [18, 20–22, 24–26] and in detail in the PAM-CRASH solver reference manual [27]. The material card for UD composites (*Ply Type 1*) is based on the material model defined by Ladeveze and LeDantec [28].

Once the material properties are input in the material card, a single element model is used to calibrate it [29]. The single element model is composed of a single element, of which the boundary conditions and the applied load allow to simulate the coupon tests conditions. The stress vs. strain curves from the one element calibration are then compared to verify that the material behaves as expected. An example of calibration result is shown in Figure 2.11.

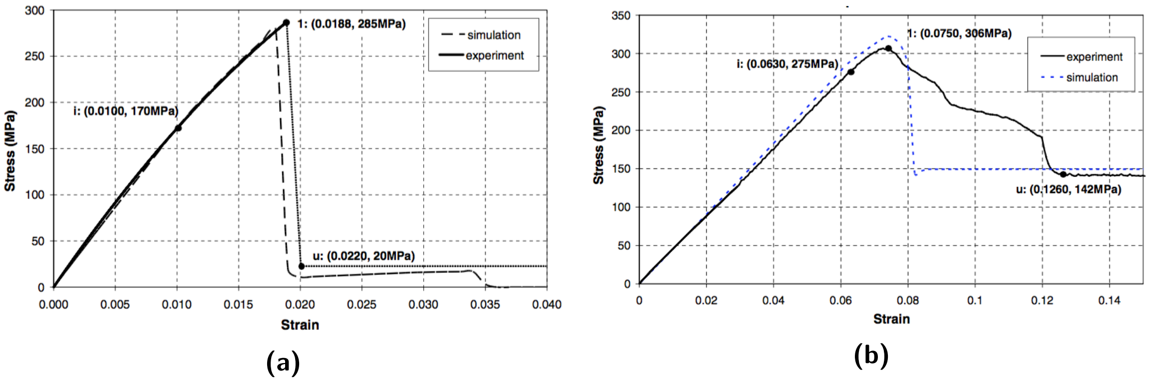

Figure 2.11: Material calibration for tension (a) and compression (b) [18].

To take into account the strain rate effect on material properties, the same steps described above have to be followed. Coupon tests will be performed at different strain rates, and the material card is calibrated at each strain rate tested [24].

2.2.2 Material Card Validation

Before using the material card for simulations of components the calibrated material card is validated through the simulation of a 3PB test [25, 26, 30]. The 3PB model is used because of its simplicity (only the specimen, and a simplified version of the two supports and the impactor are modelled), it is less computationally expensive and geometrically complex compared to a structure. Also the contact between specimen and the support has to be taken into account.

Of interest are the results obtained by Tomlin and Reynolds [26]. Thanks to the 3-point bending validation, the authors were able to understand that the compressive properties used in the material card were not correct. Such properties were taken from literature and not obtained through coupon tests. Despite modifying such properties, the peak strength was still underestimated by the results of the 3PB simulation compared to the test results. Through sensitivity studies they found that the peak strength was completely governed by the tensile strength in fibres direction. The tensile tests were then performed again, the coupon size and the end condition were modified and better test results were obtained. The initial and modified simulation results obtained by Tomlin and Reynolds are shown in Figure 2.12.

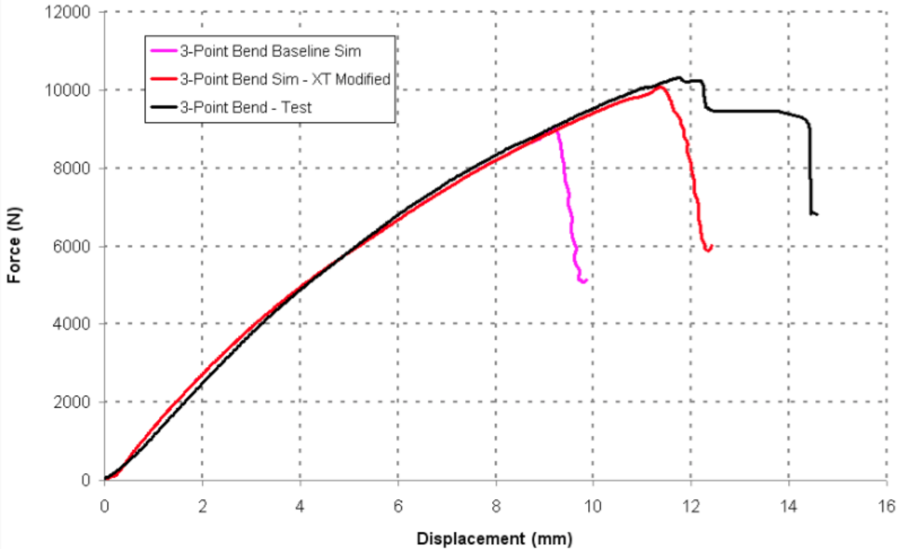

Figure 2.12: 3-point bending validation [26].

2.3 Composites 3-Point Bending Tests

As seen in section 2.2.2, the 3-point bending test can be used to validate material models employed for finite elements simulations. It is therefore important to understand the procedures needed to perform this test and the material properties that can be obtained from it. The test results are used for validation of material cards. Reliable test setup are thus needed for the comparison with the simulation results. In this section, the state of the art of quasi-static and dynamic 3PB test will be reviewed.

2.3.1 Quasi-static Tests

The quasi-static 3-point bending test is state of the art and international standards have been developed. Such standards – for example the DIN EN ISO 14125 [31] – give guidelines regarding the optimal test setup in terms of specimen geometry, supports and impactor radius, support span, and loading rate. As this kind of test allows determining the flexural properties of a material, the equations to determine the material properties of interest are also provided.

Since composites are anisotropic materials, from bending tests it is possible to obtain a wide range of material properties. This is displayed in Table 2.1, where 1, 2 and 3 refer to the laminate reference system.

For example, Mujika et al. [32] were able to obtain the tensile and compressive modulus for two UD carbon/epoxy materials from bending tests. They then checked the tensile modulus obtained with the one resulting from tensile tests on the same material. The two values were in agreement and differed by less than 5%.

Van der Vossen [33] investigated the spatial variability of stiffness in fibre reinforced composites, focusing on specimens used for short beam shear tests. Digital image correlation combined with finite element analysis were used to characterise material properties. The DIC allowed to obtain full field strains from tests, while the FEA was used to obtain nodal stresses at the same positions where strains were computed. By combining the two measurements it was possible to obtain stress vs. strain curves, that were used to determine the variation of the tensile and the compressive stiffness, the Poisson's ratio, and non-linear shear properties across the specimen surface. The method used correctly displays the change in axial stiffness in the specimen from the compressive region to the tensile area. The analysis on the shear properties showed that the shear stiffness increased in the non-linear region where there are compressive transverse stresses in the specimen, suggesting that transverse compressive stresses affect the shear stress-strain behaviour.

Table 2.1: Mechanical properties obtainable from 3-point bending tests [34].

Material Plane	Measured Properties
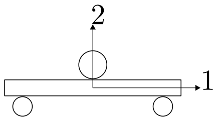	Axial tensile modulus E_{11T} Axial compressive modulus E_{11C} Poisson's ratio ν_{12} Shear modulus G_{12} Secant intercept modulus K_{12} Exponent n_{12}
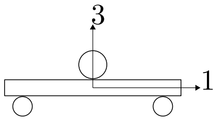	Axial tensile modulus E_{11T} Axial compressive modulus E_{11C} Poisson's ratio ν_{13} Shear modulus G_{13} Secant intercept modulus K_{13} Exponent n_{13}
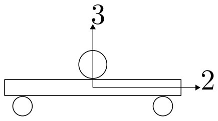	Axial tensile modulus E_{22T} Axial compressive modulus E_{22C} Poisson's ratio ν_{23} Shear modulus G_{23}
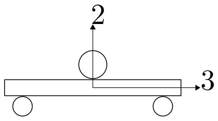	Interlamiar tensile modulus E_{33T} Interlaminar compressive modulus E_{33C} Poisson's ratio ν_{23} Shear modulus G_{23}

2.3.2 Dynamic Tests

It has been shown that for tensile, compressive, and shear tests there are no standards for strain rate dependent tests. The same is valid for bending tests. Strain rate dependent 3-point bending test (also referred to dynamic or impact 3-point bending) is under investigation in the research community. However, a limited amount of studies has been found in literature. One of the first studies was performed by Lifshitz et al. [35]. Low velocity impacts were performed using a drop tower on carbon/epoxy AS4/3502 specimens. The test setup is shown in Figure 2.13.

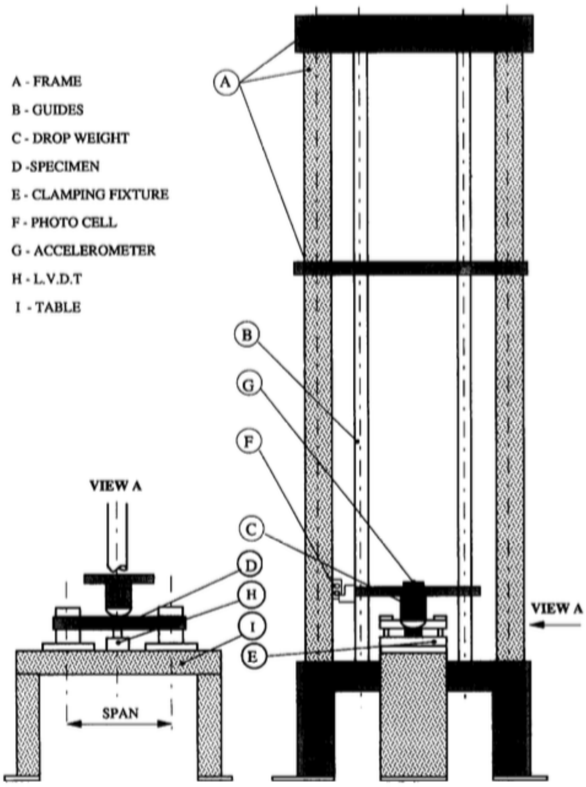

Figure 2.13: Drop weight tower setup [35].

Specimens with different layups were tested, all consisting of a different combination of 0°, 90°, 45°, and −45° layers. The drop weight velocity before impact is measured by a photo cell and an accelerometer measured the striker acceleration during impact. One of the difficulties of this setup is to measure the applied force and the specimen mid-point displacement, as they are derived from the acceleration measured from the accelerometer. The applied force was then computed by multiplying the acceleration by the mass of the dropped weight. The specimen displacement was obtained by integrating the acceleration signal during impact two times. To this purpose the velocity measured from the photo cell was used as initial velocity to determine the velocity during impact. Test results showed that under low velocity impact the beam rigidity was equal to the one obtained from quasi-static tests. The measured failure load and the energy under impact were lower than the one measured from quasi-static tests. An example of load-displacement curve for both quasi-static and impact tests is shown in Figure 2.14.

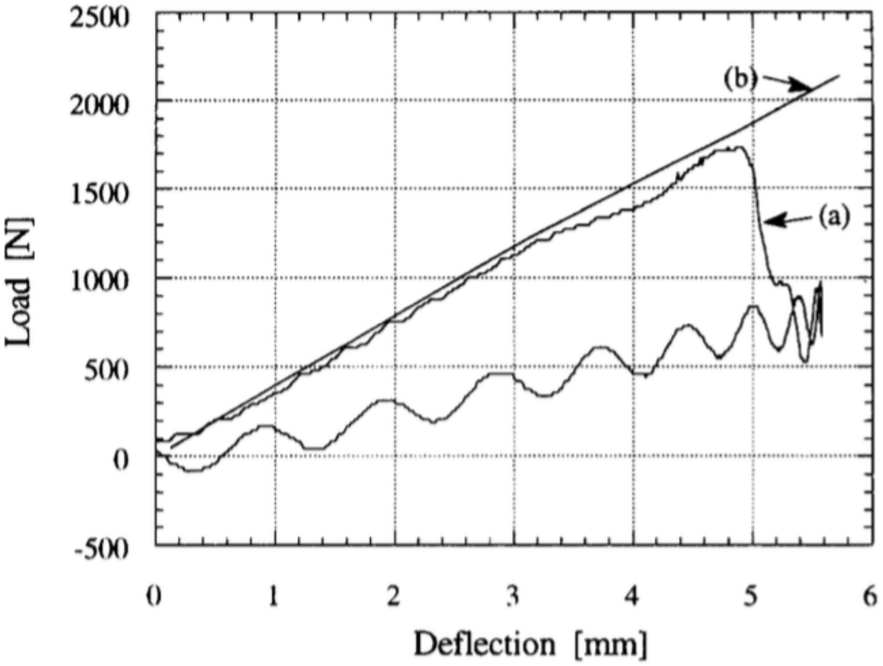

Figure 2.14: Load vs. displacement curve for impact (a) and quasi-static (b) tests [35].

Also Sánchez-Sáez et al. [36] performed 3-point bending impact tests using an instrumented drop weight tower on carbon/epoxy laminates. Test results at room temperature showed that the mechanical strength for dynamic tests was lower compared to the quasi-static values, for all layups tested. This behaviour was also observed by Lifshitz et al. [35]. In both studies the specimens failed initially on the tensile side of the specimen and the main failure mechanism was fibre breakage. The fact that the maximum force of dynamic 3-point bending tests did not increase could be due to the fact the carbon fibres do not have a tensile strain rate dependent behaviour, as demonstrated in Section 2.1.1.

Hallett [37] performed 3PB impact tests using a gas gun apparatus, which is shown in Figure 2.15. A titanium bar fired by compressed air impacts the impactor bar, which then strikes the specimen. The impactor strikes the target in a stress-free state. The impactor velocity before impact was measured by an infra-red timing gate. The force was obtained from a strain gauge bonded to the middle of the impactor. The specimen mid-point deflection was obtained from both measurements from a strain gauge bonded to the specimen side, and from pictures recorded with high-speed cameras. Specimens were obtained from a T300/914 carbon fibre composite with a cross-ply layup. From the recorded pictures it was possible to see that failure initiates by fibre fracture at the back face. The crack then propagates through the specimen thickness and delamination is observed.

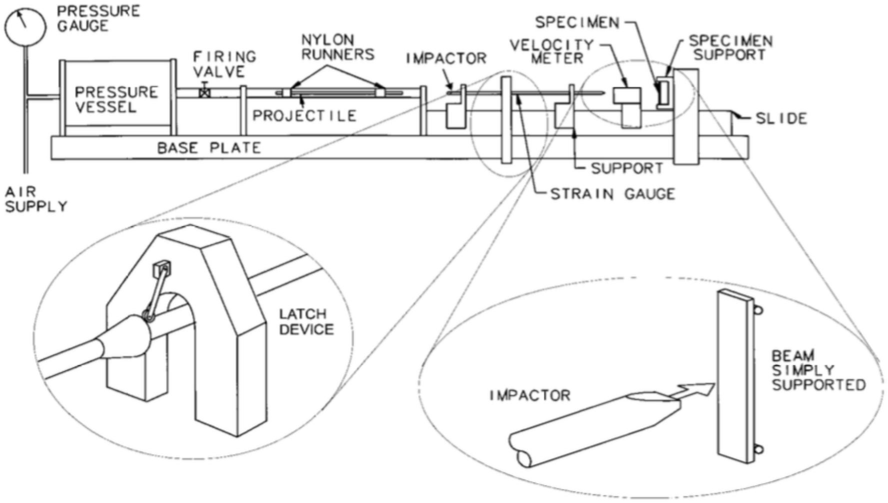
PRESSURE GAUGE
PRESSURE VESSEL
AIR SUPPLY
FIRING VALVE
NYLON RUNNERS
PROJECTILE
BASE PLATE
IMPACTOR
VELOCITY METER
SPECIMEN
SPECIMEN SUPPORT
SLIDE
SUPPORT
STRAIN GAUGE
LATCH DEVICE
IMPACTOR
BEAM SIMPLY SUPPORTED

Figure 2.15: Pressure gun apparatus for 3-point bending impact [37].

Wiegand [38] performed impact bending tests using a gas gun apparatus similar to the one used be Hallett [37], recorded using digital photography. Specimens were cut from a 3mm thick plate, which was manufactured using non-crimp fabric of carbon/epoxy T700/MTM44. Specimens were tested using a support span of 50 mm and 30 mm. All the specimen tested failed with compressive failure as the first failure mode. This was expected by the author as the tensile strength of composites is usually higher than the compressive strength. In most specimens tested failure was initiated by fibre kinking on the impacted side of the specimen.

From Figure 2.16 it is possible to see that the force and displacement at failure increase compared to quasi-static results. This behaviour is shown at both support span tested. This behaviour differs from the one observed in other studies [35, 36]. This could be due to the fact that the specimens tested by Wiegand failed first in compression, and not in tension. As seen in Section 2.1, carbon fibre composites do not show strain rate dependent properties in tension, but strong influence of the strain rate is shown for compressive and plane shear properties.

To corroborate this hypothesis the study made by Carpentier [34] showed a strain rate dependency on shear properties measured from dynamic short-beam shear test. Glass-epoxy specimens were tested using a weight drop tower, at an impactor velocity of 4.4m/s. The results obtained showed that, compared to quasi-static tests, the shear stiffness and the fracture stress increased. This behaviour shows that it is possible to determine the strain rate effect on material properties also from 3PB tests.

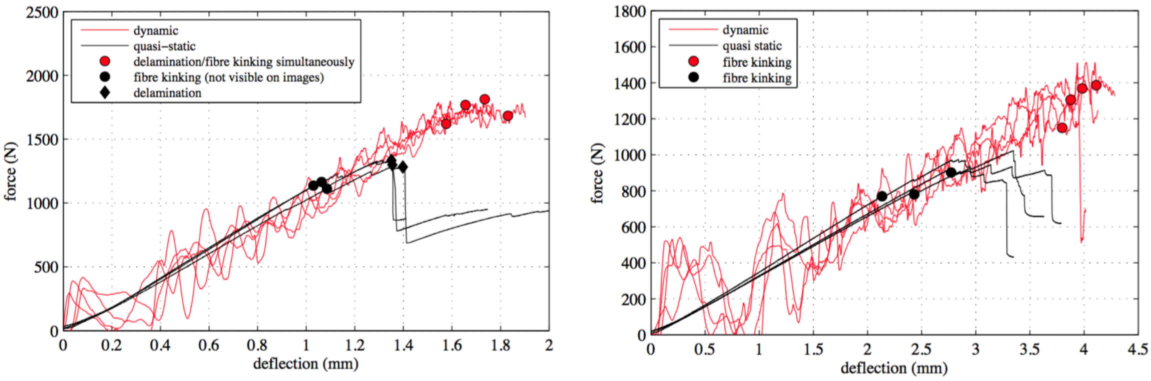

(a) (b)

Figure 2.16: Force vs. displacement curves for 0°-specimen tested with 50mm (a) and 30mm (b) support span [38].

2.3.3 Summary

The literature review has shown that 3-point bending tests can be used to determine a variety of material properties. This type of test is also used to validate material cards for finite element simulation, as shown in Section 2.2.2. It is therefore important to have reliable test setup to perform 3PB tests under quasi-static and dynamic loading conditions. The testing machines used for strain rate dependent tensile and compressive test can be adapted to perform dynamic 3PB tests.

The implementation of such setup comes with challenges that must be tackled. If accelerometers are used to measure the impactor acceleration during testing, the force and displacement are computed from the acceleration signal through multiplication and integration of it [35, 36]. This can introduce errors in the computed variables. The applied force can also be obtained from strains in the impactor rod that are measured from strain gauges bonded on it. However, the strain gauge signal can be influenced by parameters such as the fixture and the specimen natural frequencies, and the stress wave travelling through the impactor rod. Thus, the strain gage signal must be filtered [37, 38].

The use of specimens made of composites further increases the complexity of the dynamic 3PB tests. The specimen layup and the fracture mechanism strongly affects the test results. This could be the reason of conflicting results in literature. When the initial failure mode is compressive or shear, test results for dynamic tests show an increase of fracture force compared to quasi-static results [37, 38]. While specimens that failed in tension showed a decrease in fracture force when tested under dynamic conditions [35, 36]. This can be recollected the composites strain rate dependent behaviour described in Section 2.1. It is therefore required a further investigation to better understand the composites behaviour under dynamic 3PB tests.

2.4 Thesis Objective and Research Questions

The thesis work has taken place at the *Leichtbauzentrum* (Lightweight Design Centre) of *Audi AG*. So far the material cards, used for simulation of composite structure, have not taken into account the strain rate effect on the material mechanical properties. It is now in the company interests to implement the strain rate dependent behaviour in the material cards used. If the increase in mechanical properties due to strain rate effect is taken into account, it could lead to lighter and less conservative design of composites structures. To do that it is required to calibrate and validate the new material cards. The laboratory is equipped with a servo-hydraulic testing machine to perform strain rate dependent tests. As no fixture was already available it was required to design it and the test setup to perform dynamic 3PB tests. The finite element model used for validation of the new material cards is implemented to match the designed test setup. The thesis objective can be stated as follows:

The objective of this Master's thesis is (a) to improve the material card used for finite element simulations of carbon fibre reinforced plastics, dealing with strain rate dependent material properties, (b) by defining an optimal strain rate dependent dynamic 3-point bending test setup and (c) by implementing the strain rate dependent simulation model for validation of the material card.

Based on the literature review, the research questions and sub-questions are the following:

1. Since UD CFRPs show strain rate dependent compressive and shear behaviour, is this behaviour also displayed during strain rate dependent 3-point bending tests??
    - Is the new developed fixture able to measure the applied force during testing?
        - What are the design limitations due to manufacturing constraints?
        - What is the optimal impactor and support radius?
    - What is the best testing configuration -in terms of specimen stiffness- that gives reliable test results?
        - what is the optimal combination of specimen thickness and support span?
2. Can the strain rate dependent material model implemented in the finite element software PAM-CRASH describe correctly the behaviour of the material shown during testing?
    - Which ply type in PAM-CRASH fits best the needs of this project?
        - Is it better Ply Model Type 1 or Ply Model Type 7? (see Section 5.2.1)
    - Are there any limitations imposed by the simulation department?
        - What are the changes required by the already existing finite element model, used for simulation of quasi-static tests, in order to adapt it to the strain rate dependent test setup?
        - Are there any limitations in terms of element size for the specimen mesh?
    - How can a parametric model be implemented where testing parameters -such as specimen thickness and support span- can be easily changed by the user?

In the first research question the optimal test setup to measure the specimen response during testing is addressed. The goal is to define the optimal support radius, specimen thickness and support span that gives reliable results at any testing speed. The first step will be to finalize the supports and impactor design. The force measurement system that will be used is of new design in the company, therefore it must be calibrated and validated before starting with the test plan. Subsequently, the optimal setup will be investigated by changing the specimen thickness and the support span.

In the second question the implementation of the finite element model is addressed. The goal is to implement a simple and computationally inexpensive model for validation of the material card. As a base line the already implemented model used to simulate quasi-static tests will be used. The model should yield accurate results, taking care of the limitations imposed by the simulation department. Parameters such as specimen thickness, support span, and testing speed should be easily changed in the model, as this are the parameters that can be changed during testing.

2.5 Conclusions

Fibre reinforced composites, and in particular carbon fibre reinforced plastics, are finding an increasing use in the automotive industry. Thanks to their properties they allow obtaining lighter design, compared to equivalent metal structures. However, vehicle crashworthiness must not be affected by weight reduction. It is a very important characteristic for the vehicle, as passengers' safety is a priority in car design. Thus, the introduction of CFRPs components in the vehicle design must not affect the vehicle crushing performance. To ensure this, crash tests of components and of full vehicles are performed. During crashes dynamic forces are transferred through the structure. It is therefore important to understand CFRPs behaviour under dynamic loads.

Strain rate dependent tests are performed on specimens to understand the material behaviour under several loading rates. CFRPs show strain rate dependency for compressive [9–15] and shear [7, 8, 10, 15–17] properties. No strain rate effect has been seen for longitudinal tensile properties of UD composites [4, 7]. In general, strain rate dependant behaviour is found on composites properties that are affected by matrix behaviour. Results coming from dynamic 3PB tests must be reliable in order to be compared with the simulation results. Issues have been encountered in literature concerning the force signal measurements and it has been reported that the specimen fracture mechanism highly influences the test outcome [35–38]. Additional analysis are needed to better understand the behaviour of UD carbon fibre composites under 3PB tests.

Finite element models are used to assess structure performances to optimise their design, the strain rate effect on CFRPs material properties should therefore be taken into account to have a more reliable simulation results. Material cards must be calibrated and validated also for strain rate dependent properties. The 3-point bending test is generally used to validate material cards, as it has a simple setup, but induces a complex state of stress in the specimen tested [25, 26, 30]. A similar validation process must be carried out for the strain rate properties.

Review of previous work has shown that there is no accepted standard for rate-dependent testing of composites. There is, therefore, a need for the evaluation of tests like the 3-point bend test in order to determine the optimum parameters (specimen thickness and support span) such that reliable data can be measured from the test setup. This can then be used to validate a material card in the FE model which take into account strain rate dependent material properties, so more accurate material cards are available for simulation of vehicles crash tests. The goal of this Master's thesis is to contribute to improve the composites material card used by Audi AG and to reach a better understanding of the behaviour of unidirectional CFRPs under dynamic 3-point bending test. As specified in details above, its first aim is to implement a dynamic 3-point bending test setup for the available servo-hydraulic testing machine, by designing the fixture and by investigating the effect of test parameters. This will make it possible to obtain reliable test results which will then be used for validating the material card. The second aim is to create the FE model to simulate dynamic 3-point bending tests, which will be used for the validation of material cards that take into account strain rate dependent material properties.

Chapter 3

Strain Rate Dependent 3-Point Bending Test

This chapter discusses the dynamic 3-point bending tests. Section 3.1 presents the equipment used to perform the tests, Section 3.2 gives a description of the designed fixture and the applied load measuring system, in Section 3.3 the test results are presented. Finally, conclusions based on the content of this chapter are drawn in section 3.4.

3.1 Testing Equipment

In this section, the testing equipment used to perform the dynamic 3-point bending tests is presented.

3.1.1 Instron High Strain Rate VHS

As described in Chapter 2, a wide range of testing machines can be used to preform strain rate dependent coupon tests. Servo-hydraulic testing machines and drop towers are used for intermediate strain rates, the split Hopkinson bar is instead used for testing at high strain rates. For the 3-point bending tests performed for this thesis a servo-hydraulic testing machine was used. The testing machine is the High Strain Rate VHS System manufactured by INSTRON, and can be seen in Figure 3.1. Important parameters are the hydraulic piston velocity achievable and the maximum load that the testing machine can apply. The piston can reach a velocity up to 20 m/s for tensile tests and 10 m/s for compressive tests, and the maximum load is 100 kN.

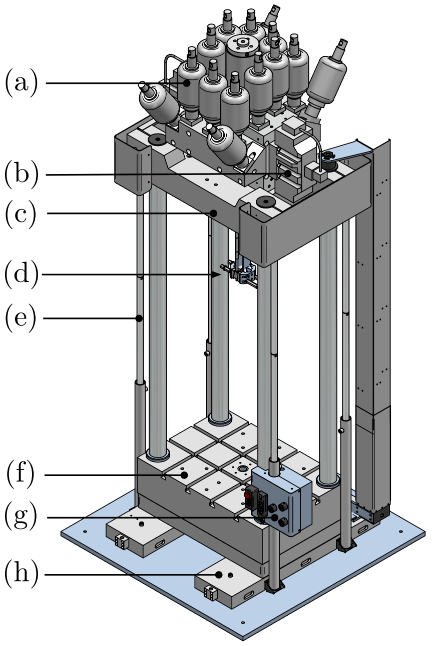

(a) Pressure vessels
(b) Three-way servo valve
(c) Crosshead adjustable in height
(d) Hydraulic piston
(e) Hydraulic cylinder for crosshead height adjustment
(f) Lower base
(g) Control unit for hydraulic piston and crosshead height adjustment
(h) Air suspension

Figure 3.1: Servo-hydraulic testing machine [39].

The kinetic energy needed to perform the test is generated by accelerating the hydraulic piston. Pressured oil is used for this purpose. The oil is compressed to a pressure of 280 bar by a separate pump. It is then collected at the top of the testing machine in the pressure vessels. The pressure vessels are also filled with nitrogen to ensure that the oil keeps the pressure imposed by the pump. To accelerate the piston the three-way servo valves are opened, releasing the high pressured oil in the accelerating circuit.

A special feature of this servo-hydraulic testing machine is the control of the piston velocities for testing speeds higher than 1 m/s. The control is obtained via a calibration curve, therefore a calibration procedure has to be performed to calibrate the servo valves that govern the piston velocity. By changing the valves opening angle, the piston velocity is changed. As the valve opening is defined by a signal voltage, it is important to correctly calibrate the piston testing speed, because it depends on the mass of the piston and of the fixture connected to it. Through the calibration procedure a voltage is given as an input to the testing machine and the equivalent testing speed is measured by a built-in linear variable differential transducer (LVDT). The calibration curve is then obtained through interpolation of the measured points. An example is shown in Figure 3.2, note that the calibration curve might not be linear. For testing velocities lower than 1 m/s a closed-loop control system is available. Four valves are used in this case. The closed-loop control circuit uses the velocity measured by the LVDT to continuously adjust the valves opening angle. The testing speed is always adjusted and kept constant throughout the whole test.

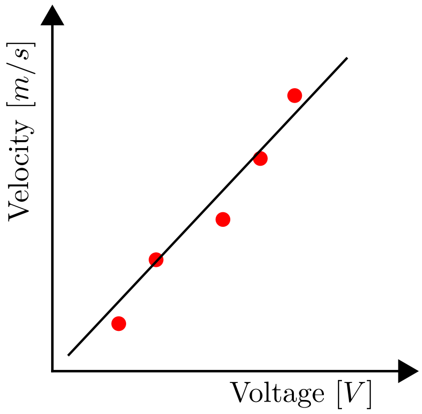

Figure 3.2: Example of calibration curve.

3.1.2 Optical Measurements

Parameters such as the specimen displacement, the strain distribution, and the piston velocity, were recorded and evaluated using high-speed photography. The recording apparatus consisted of two Photron FASCTAM SA-X type 259K-M1 high-speed cameras and the digital image correlation (DIC) software used was ARAMIS® [40], from the company GOM. To measure the parameters of interest the experiment is recorded with the high-speed cameras and the pictures obtained are evaluated using the DIC software. ARAMIS® analysis is based on the gray-scale correlation. The images are given as an input to the software and analysed. ARAMIS® automatically recognises the measuring points. As it is possible to see from Figure 3.3, at least three measuring points are needed so that the software can track them. To improve the specimen surface gray-scale information, all the specimens were painted using a stochastic pattern, which is visible in Figure 3.3.

To obtain the strain distribution and the specimen midpoint displacement it is necessary to create a surface component. The surface component is divided in facets, which are square elements where the gray-scale information of the specimen surface they cover is stored. The facet size depends on the dimension of the black points created by spraying the specimens with the stochastic patterns. Such black dots should have a diameter that ranges between 6 and 9 pixels. The optimal facet size allows fitting three black dots in it. This is important in order to have enough information on the gray-scale pattern in each facet. For the set up employed the optimal facet edge size was between 15 and 20 pixels, so a facet edge size of 15 pixels was used for the analysis. The gray scale information in each facet is saved in its central pixel, so it is important to use an odd number of pixels for the edge size, because it is the only way to get a central pixel in the facet. The optimum gray-scale saturation value for the white areas of the pattern is between 160-180 RGB. To obtain this, it was necessary to find the right combination of shutter speed and camera lenses aperture.
Optical triangulation is at the basis for the strain distribution and displacement of the measuring points calculation. The software is able to compute the coordinates in the three spacial directions (x, y, and z) for all facets and measuring points. The first picture imported is used as the reference stage and it is representative of the undeformed state of the specimen. For the other pictures the software is able to recognize each facet and obtain the displacement

vector. From it, ARAMIS® can obtain the strain distribution.

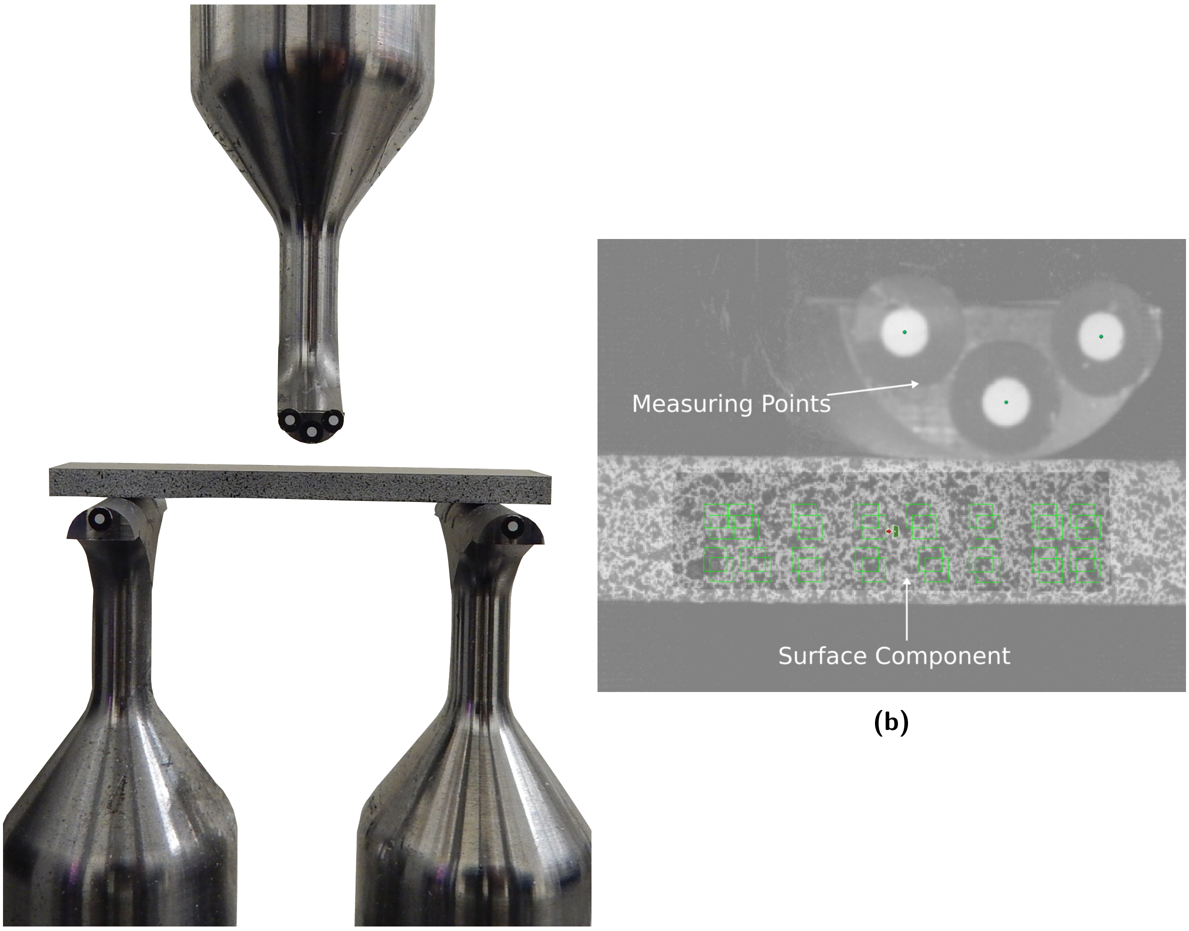

(b)

(a)

Figure 3.3: Test setup (a) and cameras measuring volume (b).

At full screen resolution (1024 × 1024 pixels) the maximum frame rate is limited by the cameras memory, which is 8 GB for each camera [39]. In order to increase the frame rate it is necessary to reduce the measuring volume. Images with a lower resolution occupy less space in the cameras memory, therefore it is possible to save a higher number of pictures compared to full screen resolution. Due to the limited memory, the recording time decreases with increasing frame rate. However, this was not an issue because dynamic tests last for a very short time period. Due to physical constraints imposed by the testing machine, the cameras were placed at a distance of approximately 600 mm from the specimen and lenses with a focal length of 100 mm. Given this setup, it was possible to reduce the measuring volume to 384 × 512 pixels and the frame rate obtained was 45 000 fps.

The high-speed cameras and the testing machine form two separate measuring systems. For the post processing of the data acquired, it is important that the acquisition of data coming from the testing machine and the fixture in it, and the data coming from the high-speed

cameras are synchronised. This is needed so as to correctly characterise material properties that depend on both the data collected by the testing machine and the data collected by the high-speed cameras. One example is the Young's modulus, which depends on the relation between stress (obtained from the force measured by the fixture) and strain (obtained from analysis of the pictures taken from the high-speed cameras).
The synchronisation system was already available, as it had been implemented by Schmack [39]. It was implemented using a high-speed data logger from National Instrument and its configuration is shown in Figure 3.4. The testing machine sends a trigger signal to start of data acquisition of the high-speed cameras. The pictures taken by the cameras are directly sent to the laptop for post processing. The testing machine and the cameras are both connected to the data logger. The testing machine sends the force signal and the sampling trigger signal, while the sampling rate is provided by the high speed camera. The data logger then sends the sampled force signal to the laptop for post processing. This setup ensures that force measurements and pictures are taken at the same sampling rate and that data acquisition starts at the same time in the two measuring systems.

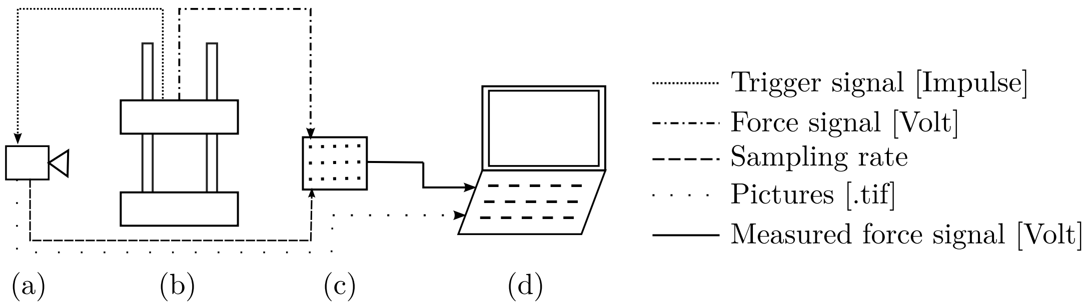

Figure 3.4: Signal processing between the high-speed cameras (a), the testing machine (b), the data logger (c), and the laptop (d) [39].

3.1.3 Material

As material, a commercial high-modulus-carbon-fiber (T700, Toray) with a tensile strength of 4900 MPa [41] was used as a part of the epoxy based prepreg system. The epoxy matrix used is the DT120 from Delta-Tech, with areal weight 150 g/m^2 [42]. Unidirectional (UD) laminates were used to manufacture the tested specimens. As composites are anisotropic material with lower compressive mechanical properties compared to the tensile ones [32], it was inferred that they would brake with a compressive failure at the impacted side, or by delamination. In Chapter 2 it was shown that compressive and shear properties show strain rate dependency, therefore strain rate dependency was expected also in the 3PB tests.
To investigate the thickness effect on the force signal, plates of different thicknesses were manufactured. All the plates were manufactured using the hand layup to stack the UD plies. The stacked prepreg plates were then cured in an autoclave using the vacuum bag method. The curing cycle was set according to the guidelines provided by the material manufacturer [42]. High quality manufactured plates were required. In order to obtain smooth surfaces the stacked prepreg were placed between two carbon fibre mould plates, during the curing process. After the autoclave process, several quality inspections were performed. The thickness of all plates was measured using a Kroeplin IP 67 at nine different position, as shown in

Figure 3.5a. The fibre volume was measured using specimens taken from the nine positions shown in Figure 3.5b. The results obtained are summarised in Table 3.1.

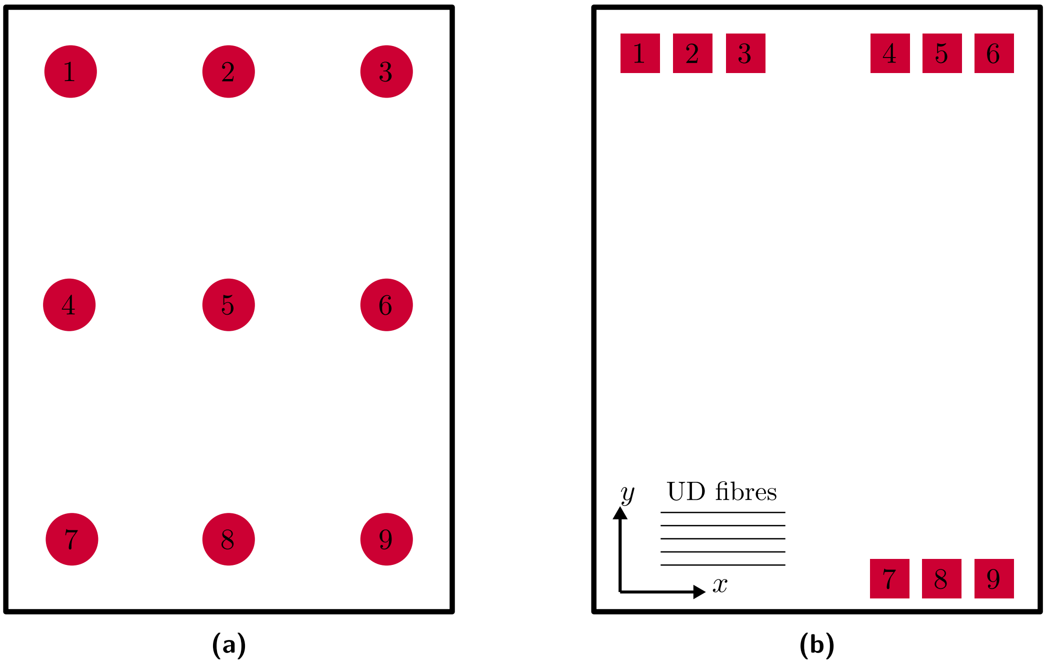

(a) **(b)**

Figure 3.5: Positions for thickness (a) and fibre volume (b) measurements.

The average fibre volume of all plates was 54.09 % and all the plates show a very similar fibre volume. This was an important requirement, as specimens with different thicknesses were tested, and the fibre volume did not have to affect the results obtained.

Table 3.1: Average measurements for plate thickness and fibre volume.

Number of UD plies	Plate Thickness [mm]	Fibre Volume [%]
10	1.49	54.29
13	1.96	54.56
17	2.54	53.52
20	2.99	53.96
23	3.41	54.44
27	4.00	54.56
30	4.50	53.83
33	4.90	54.18
37	5.52	53.45

3.2 Fixture

No fixture was already available for the servo-hydraulic testing machine used to perform the tests. The fixture design was an important step in order to carry out the test programme. In this section the fixture design and the system used to measure the force applied to the specimen are described.

3.2.1 Design

Since there are no standards for the dynamic 3-point bending tests performed with servo-hydraulic testing machines, the guidelines provided by the DIN EN ISO 14125 [31] standard for quasi-static tests were used for the fixture design. The typical test setup is shown in Figure 3.6, where h is the specimen thickness, L is the support span, R_1 is the impactor radius, and R_2 is the radius of the supports.

The support span must be adjustable as it can change according to specimens layup, material, and thickness. The radius of the fixture components (the impactor and the two supports) are defined according to Table 3.2. The impactor radius is fixed and independent from the specimen thickness, while the radius of the supports depends on it. Normally, for quasi-static tests, specimens with 2 mm thickness are used for 3PB and 4PB tests in the AUDI laboratory. However, the fixture had to allow testing specimens of different thicknesses, as specimens with a wide range of thicknesses were tested. Furthermore, the fixture had to be long-lasting as it would not be used only for the tests performed during this thesis, but also for any future test needed by the laboratory. Lightness and strength were other important properties, as a light fixture would have a low impact on the testing machine performance and reduce inertia effects on the force signal, and it was important for it not to break under the applied load.

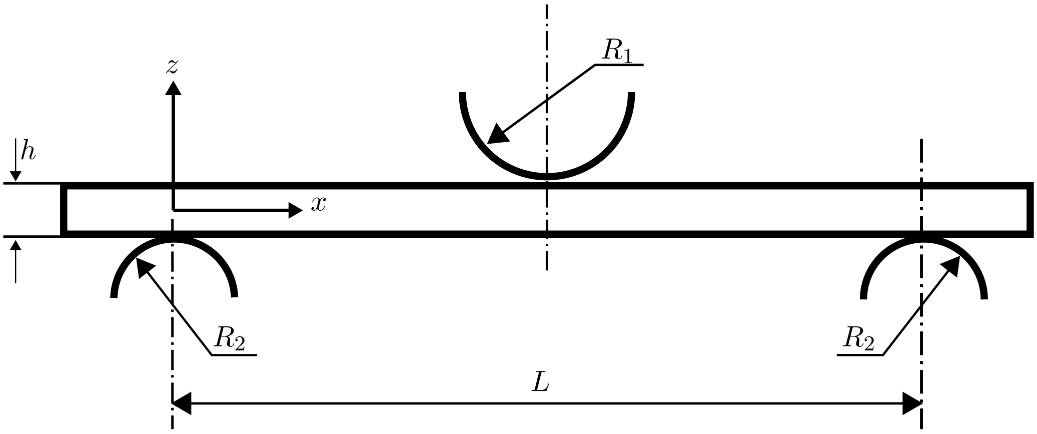

Figure 3.6: 3-point bending setup [31].

Since it was not possible to use the existing piezoelectric load cell used, as it was fixed to the fixture used to measure the applied load for tensile tests, it was decided to use strain gauges on the impactor and on the two supports to obtain the force signal. Strain gauges are widely used to measure strains on specimens during material testing. Hallett [37] and Wiegand [38] have successfully measured the applied load during dynamic 3PB tests using linear strain gauges on their fixture. The use of strain gauges was therefore considered a reasonable and cost effective solution.

Table 3.2: Impactor and supports radius dimensions [31].

Dimensions [mm]	Value [mm]
R_1	5 ± 0.2
R_2 for $h \leq 3$	2 ± 0.2
R_2 for $h > 3$	5 ± 0.2

The fixture requirements can be summarised as follow:

- allowing testing a wide range of specimen geometries
- durable
- light
- strong
- cost effective
- allowing using strain gauges to measure the applied load
- local force measuring near the specimen

The final fixture design is shown in Figure 3.7. The impactor is screwed to an adapter, which allows fixation to the piston of the servo-hydraulic testing machine. The two supports are fixed to a base plate using four T-nuts for each support. The base plates and the use of T-nuts allow to move the two supports, so that the support span can be changed depending on the test requirements.

The impactor and the two supports were manufactured using TOOLOX 44 steel. It is a pre-hardened steel usually used for tools and components that necessitate high strength [43]. Although it undergoes the hardening treatment before the manufacturing processes needed for the fixture components, TOOLOX 44 has a good workability, so it was possible to manufacture the three parts using machining processes.

The impactor and the two supports have the same geometry. They all have a radius of 5 mm, which in the ISO norm allows to test specimens with thickness higher than 3 mm. The radius choice was forced because a necking region in the fixture was needed to bond the strain gauges so as to allow a correct recording of the applied load. To avoid plasticity in the impactor and supports under the maximum applicable load by the testing machine (100 kN), a minimum radius of 5 mm was needed at the necking area. This resulted in the impossibility to manufacture supports with the smaller radius suggested by the norm. The use of TOOLOX 44 and the fact that the three parts had the same shape allowed having a cost effective design without affecting the fixture durability and strength.

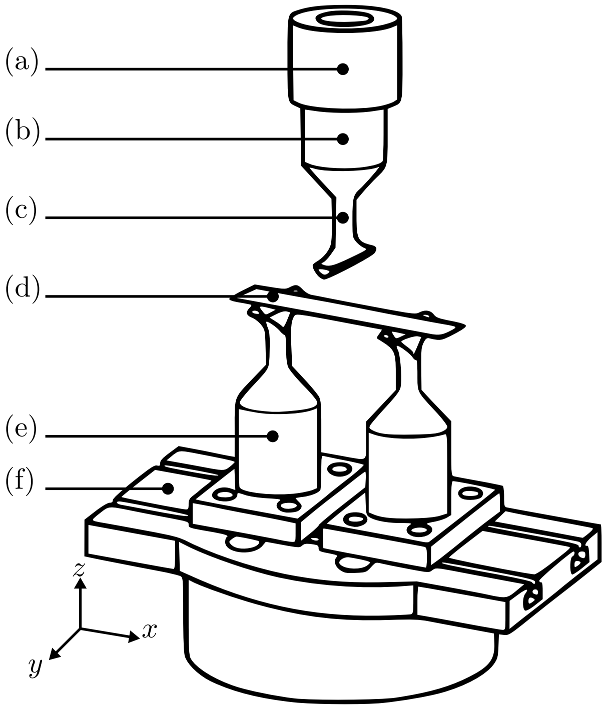

(a)	Adapter to servo-hydraulic piston
(b)	Impactor
(c)	Necking area - strain concentration
(d)	Specimen
(e)	Supports
(f)	Base plate

Figure 3.7: Fixture design.

3.2.2 Force Measurement System

For this application strain gauges of the type BTMC-1-D16-003LE from Tokyo Sokky Kenkyujo were used [44]. They are strain gauges that mainly find their application in measuring the strain in pre-loaded bolts. They are normally inserted in pre-drilled holes and fixed in position using an adhesive.

A hole with a diameter of 1.6 mm was made in the impactor and support design to place the strain gauge, as shown in Figure 3.8a. The hole length was such that the strain gauge centre corresponded to the centre of the necking area, as shown in Figure 3.8b.

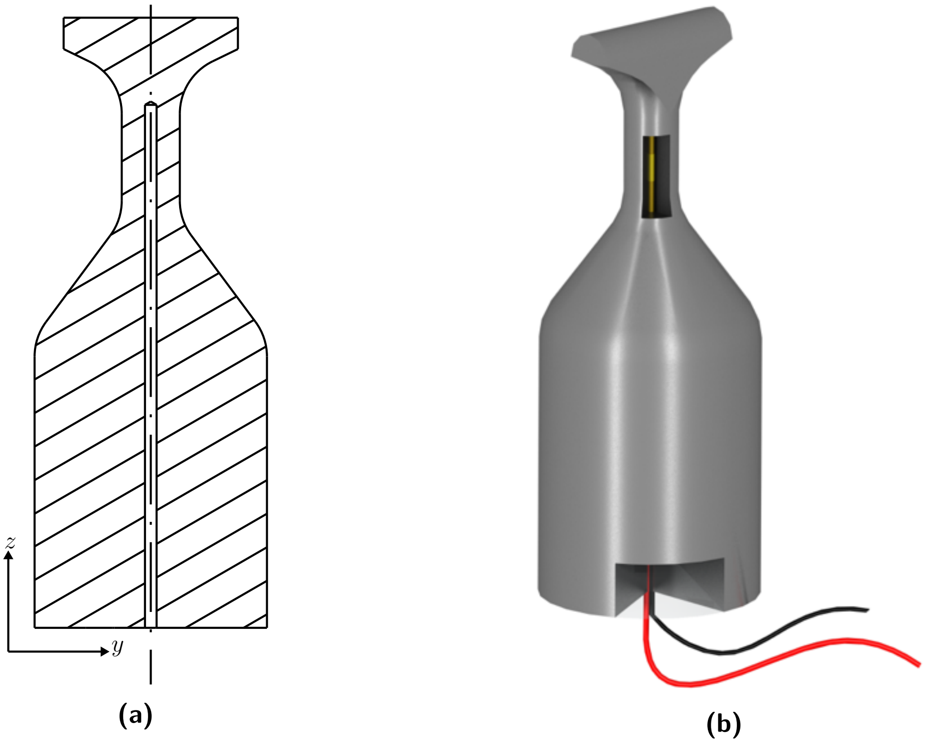

Figure 3.8: Impactor cut view (a) and strain gauge position (b).

To amplify the signal coming from the strain gauges a VISHAY Signal Conditioning Amplifier [45] was used. Each fixture component was connected to a separate amplification unit. The amplification unit provides the connection to the ground and has a built-in Wheatstone bridge circuit. For all the three fixture components the quarter Wheatstone bridge configuration was selected, it is shown in Figure 3.9. Since the strain gauge had a resistance of 120 Ω, the bridge configuration with all resistors of equal resistance was selected. The amplification units provided the bridge excitation voltage U_{in} and the amplification factor A_{WB}.

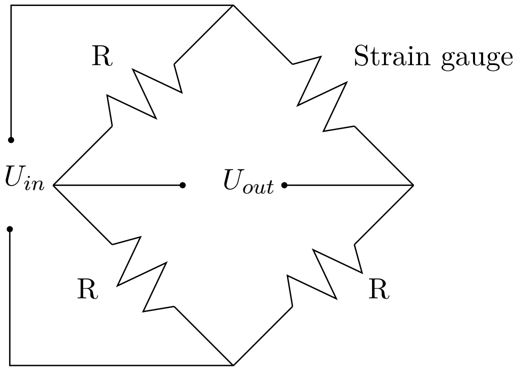

Figure 3.9: Quarter Wheatstone bridge configuration.

Through the Wheatstone bridge theory it was possible to convert the measured voltage into the applied load. The output voltage is defined by the equation

$$U_{out} = \frac{1}{4}\, U_{in}\ A_{WB}\ k\ B\ \varepsilon \tag{3.1}$$

where k is the gauge factor, B is the bridge factor (which is equal to 1 for the quarter bridge configuration), and ε is the strain in the necking area. The strain ε is the only unknown variable in the equation, as the output voltage is the quantity measured during testing. The strain is related to the applied stress σ through the steel modulus of elasticity E, according to Hook's law for isotropic material. The applied stress is therefore obtained as

$$\sigma = E\ \varepsilon \quad \rightarrow \quad \sigma = \frac{4\ U_{out}\ E}{U_{in}\ A_{WB}\ k\ B} \tag{3.2}$$

knowing the reference area A of the necking region the applied load is

$$F = \sigma\ A \quad \rightarrow \quad F = \frac{4\ E\ A}{U_{in}\ A_{WB}\ k\ B} U_{out} = S\ U_{out} \tag{3.3}$$

where S is a constant for a determined setup and is the conversion factor that allows computing the applied load from the measured output voltage. S was used as initial conversion factor, before starting the test programme the impactor and the support were calibrated to obtain a more reliable conversion factor. The calibration process followed the norm ISO 7500-1 [46], which defines how to calibrate the force-measuring system for uniaxial testing machines. The procedure used is described in Appendix 6.2.

It was important to synchronize the data acquisition of the force signals with the high-speed cameras one. To obtain this it was necessary to connect the output signals coming from the VISHAY amplifier to the data logger, as shown in Figure 3.10. This was mandatory in order to be able to combine the data obtained from the analysis of the picture taken with the force measurements. The sampled signals are then sent to the laptop for data post processing.

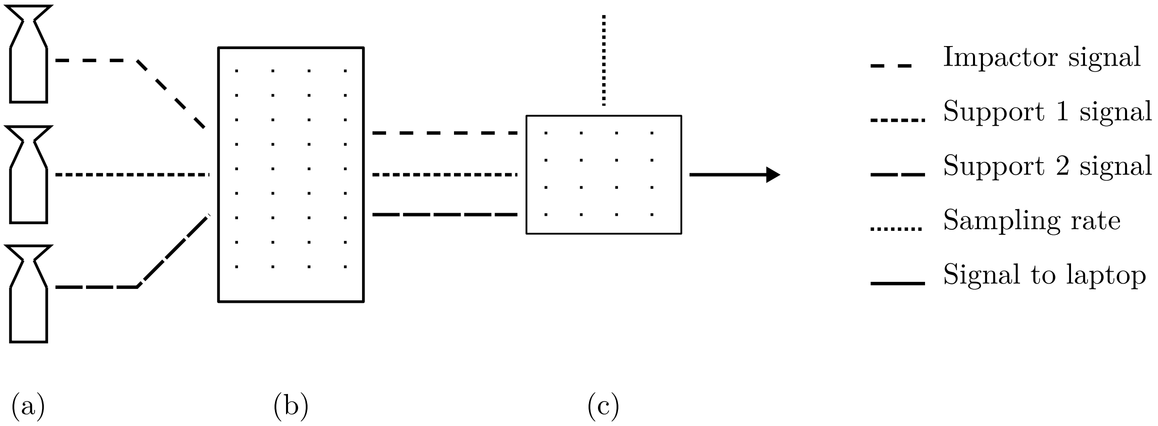

Figure 3.10: Signal processing between the impactor and supports (a), the VISHAY amplifier (b) and the data logger (c).

3.3 Test Results

In this section the test results are presented.

3.3.1 Specimen Geometry and Testing Parameters

Specimens were cut from the manufactured plates using a circular and water cooled diamond saw. High precision cuts along the longitudinal direction were obtained. This was important, because the DIC needed a smooth and plane surface to work properly.
Two different specimen geometries were tested, as displayed in Figure 3.11. They differed in terms of specimen length: specimen geometry A had a length of 100 mm, while specimen geometry B had a length of 80 mm.

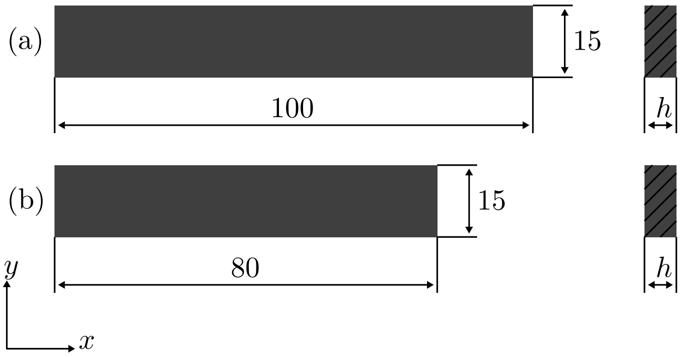

Figure 3.11: Specimen geometry tested with the support span of $80\,\mathrm{mm}$ (A) and $60\,\mathrm{mm}$ (B).

Geometry A was chosen because it is the shape suggested for quasi-static tests for UD laminates. It was tested with a support span of 80 mm, which allowed the shear effect on the specimen to be negligible [36]. This type of specimens were expected to have a compressive failure. The smaller specimen geometry was tested with a support span of 60 mm. Such support span is the smallest that can be obtained with the designed fixture. It was decided to reduce the support span, because trial tests had shown oscillations in the force signal for tests at high piston velocities. This was mainly due to the detachment of the specimen from the impactor during testing. It was therefore assumed that a setup which induces an increase in the tested specimen global stiffness would reduce the specimen detachment from the impactor. This would have led to a better force signal. In this case the specimen global stiffness is defined a the stiffness of a simply supported beam, which depends on the specimen material, the support span and the specimen cross-section geometry. A detailed explanation is given in Section 4.2.1.
Both geometries have the same width. It was not the purpose of this study to investigate the effect of the specimen width on the output parameters. So, the specimen geometry was kept as similar as possible to the one normally tested in the laboratory under quasi-static conditions. Therefore, the value for the specimen width was chosen from the quasi-static norm [31], which for UD laminates it is equal to 15 mm.

For each geometry, specimens with nine different thicknesses were manufactured. The nominal thicknesses range was from 1.5 mm to 5.5 mm with an increasing step of 0.5 mm. As the specimen were obtained from the plates described in Section 3.1.3, the actual specimen thickness is the one reported in Table 3.1 (section 3.1.3).

Tests were performed at several testing velocities. The lowest testing was the quasi-static one, where the impactor moved with a velocity of 3.3×10^{-5}m/s (equivalent to 2 mm/min). The highest testing velocity was 10 m/s. In total seven different testing velocities were used when testing specimens with geometry A, while four different testing velocities were used when testing specimens with geometry B. A summary of the testing parameters for the two different configurations is shown in Table 3.3. Emphasis was given to high testing velocities, because it was also to be investigated which would be the velocity threshold above which the results would not be reliable.

Table 3.3: Testing configurations.

Testing Configuration 1			Testing Configuration 2		
Specimen Geometry	Support Span [mm]	Testing Velocity [m/s]	Specimen Geometry	Support Span [mm]	Testing Velocity [m/s]
A	80	3.3×10^{-5}	B	60	3.3×10^{-5}
		0.1			
		0.5			0.5
		3			
		5			5
		8			
		10			10

3.3.2 Force Signal

The output signal coming from the strain gauges showed some fluctuations. One source of oscillation in the signal was the noise induced by the testing equipment and the setup. This resulted in small fluctuations in the signal as shown in Figure 3.12a. The other source was due to vibrations of the specimen. When the impactor hits the specimen, it slightly bounces and contact is lost between the specimen and the impactor. This behaviour induces the signal oscillations visible in Figure 3.12b. The force-displacement curves shown in Figure 3.12 were cut off at the failure point, as after initial failure a drop in the load was observed. It was therefore decided to filter the signal using a LOESS filter. The LOESS filter allows to define a smooth curve that fits the force signal. For this particular application a span of 25% was the one that best fitted the data at all testing velocities.

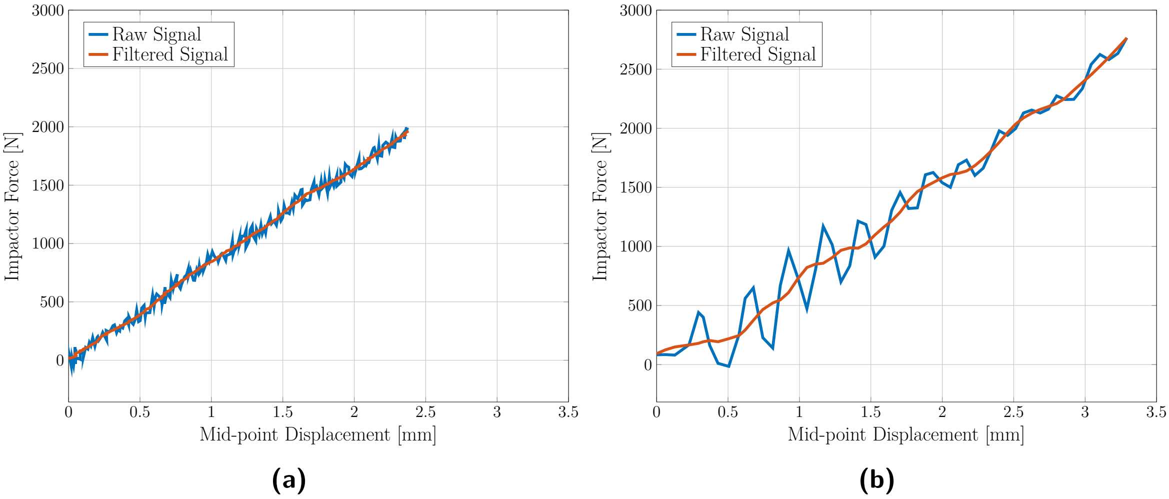

Figure 3.12: Filtered force signal for a 4 mm thick specimen with geometry A tested in (a) quasi-static conditions and (b) at 3 m/s.

3.3.3 Contact Impactor-Specimen

Specimen vibrations affect the force signal coming from the strain gauge bonded in the fixture. It was important to observe the contact evolution through time to determine whether detachment occurred between the impactor and the specimen. To this purpose, the impactor was provided with measuring points and the specimen-mid point displacement was measured from the DIC analysis (Section 3.1.2). Figure 3.13 is representative of the effect of the testing velocity on a fixed specimen geometry and specimen thickness. The plots are referred to specimens 4 mm thick with geometry A. At low testing velocities there is no detachment between impactor and specimen. The two curves overlap, as shown in Figure 3.13a and Figure 3.13b. As the testing velocity increases there is a detachment just after the initial impact, as shown in Figure 3.13c and Figure 3.13d. The specimen midpoint displacement is higher compared to the impactor one. The specimen then vibrates, as the specimen curve shows some slight oscillations. This behaviour is more accentuated at the highest speed tested. The initial specimen detachment increases as the testing speed increases.

Figure 3.14 and 3.15 are representative of the displacement measurements for tests performed at the same testing speed and specimen geometry, but with different thickness. Four thicknesses are here presented to display the general behaviour of the curves. Figure 3.14 shows the results obtained for the tests on specimen geometry A at a testing speed of 8 m/s, while in Figure 3.15 the geometry tested was the B, and the testing speed was 10 m/s. When comparing the results obtained with the same specimen geometry, it was observed that the initial detachment between impactor and specimen decreased with the increase of the specimen thickness. Furthermore, when the 60 mm support span was used no detachment was observed for the thick specimens even at the highest testing velocity (Figure 3.15d). This is thought to be due to the increase of the stiffness of the simply supported beam (the specimen) when the support span is reduced and the thickness is increased.

The use of the specimen midpoint allowed to capture the specimen detachment from the impactor, therefore the data obtained form it was the one used in all the analysis which involve the specimen displacement.

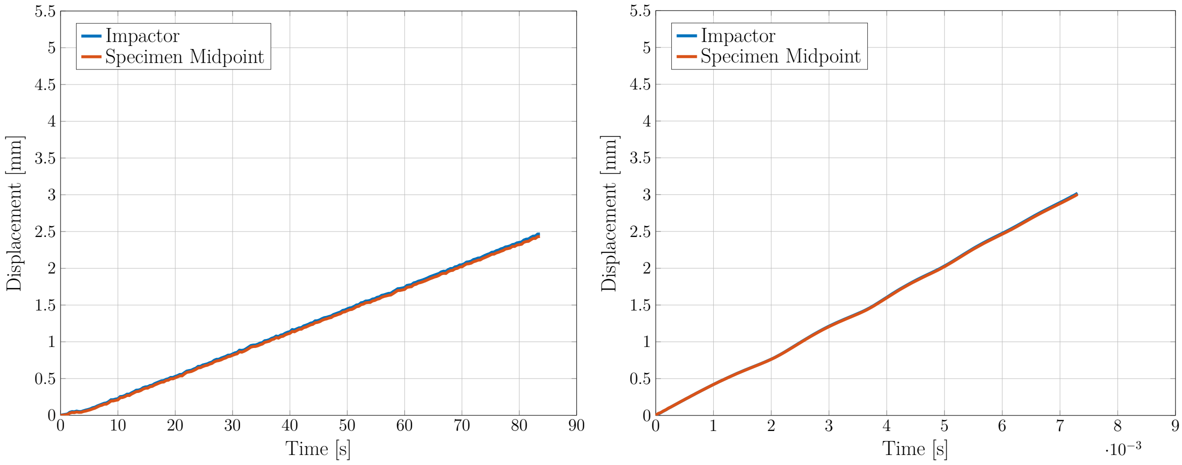

(a) 3.3×10^{-5}m/s **(b)** 0.5 m/s

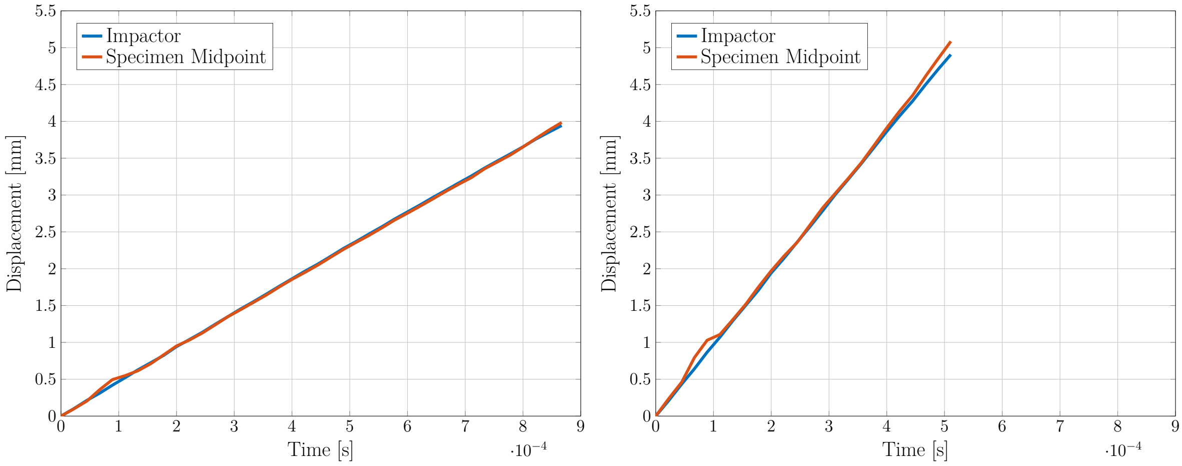

(c) 5 m/s **(d)** 10 m/s

Figure 3.13: Comparison between impactor and specimen midpoint displacement for 4 mm thick specimen with geometry A.

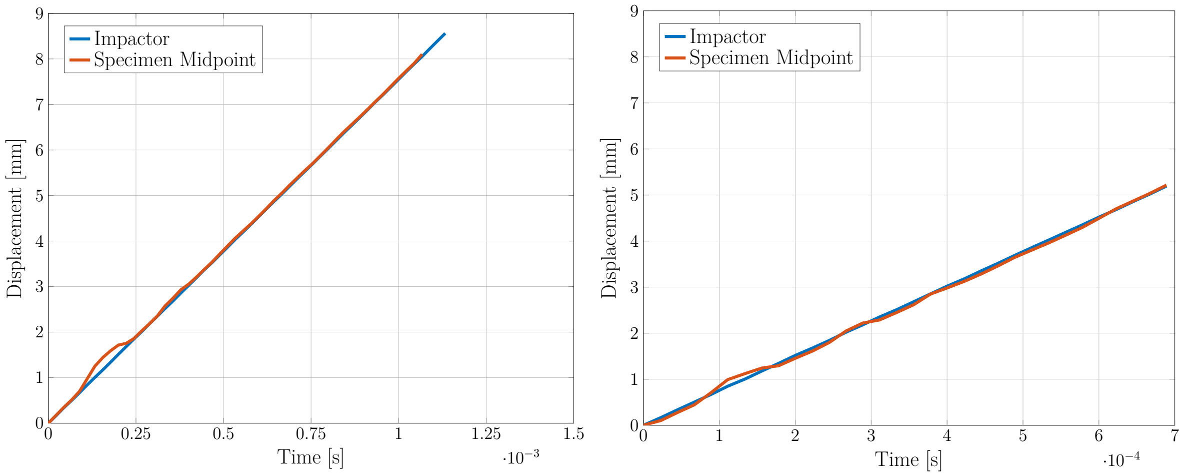

(a) $t = 2\,\mathrm{mm}$ **(b)** $t = 3\,\mathrm{mm}$

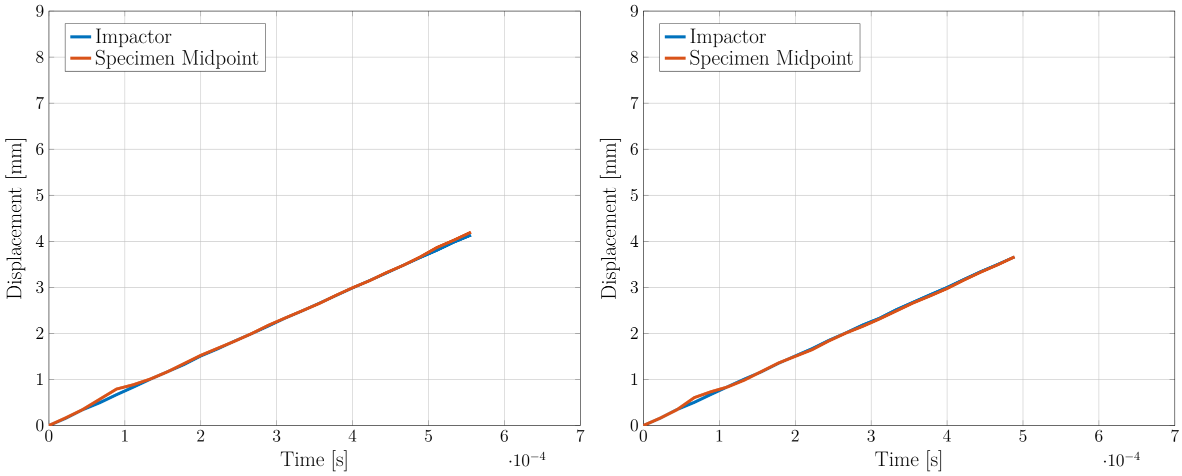

(c) $t = 4\,\mathrm{mm}$ **(d)** $t = 5\,\mathrm{mm}$

Figure 3.14: Comparison between impactor and specimen midpoint displacement for specimen geometry A tested at $8\,\mathrm{m/s}$.

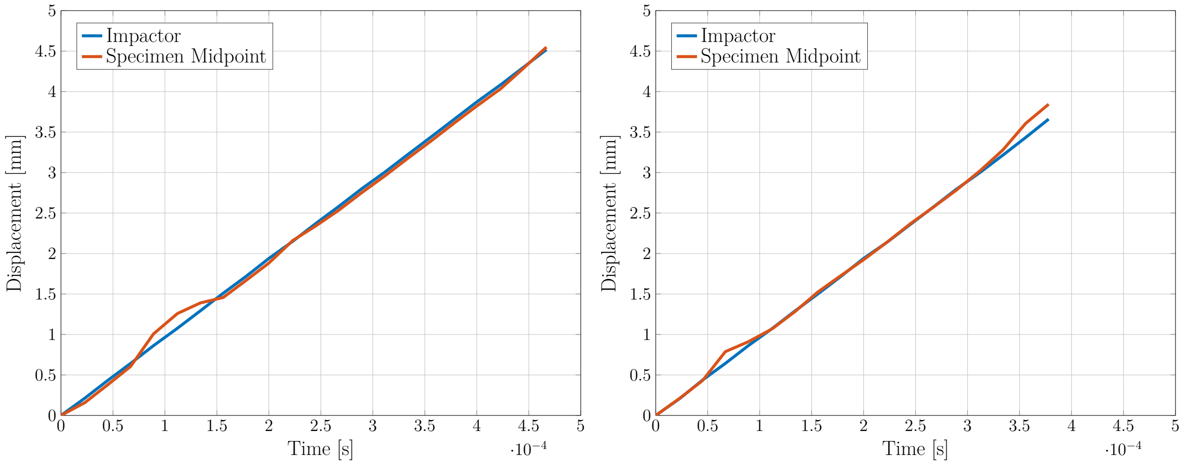

(a) $t = 2\,\mathrm{mm}$ **(b)** $t = 3\,\mathrm{mm}$

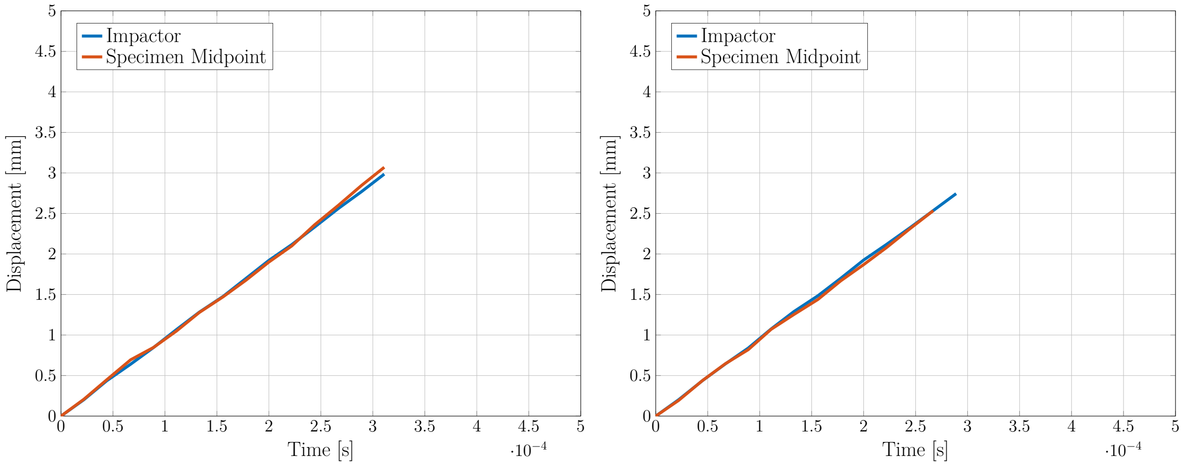

(c) $t = 4\,\mathrm{mm}$ **(d)** $t = 5\,\mathrm{mm}$

Figure 3.15: Comparison between impactor and specimen midpoint displacement for specimen geometry B tested at $10\,\mathrm{m/s}$.

3.3.4 Fracture Mechanism

All the specimens tested had a compressive failure. The initial failure was fibre kinking on the compression side of the specimens, in correspondence of the contact area with the impactor. Initial failure on the compressive side of the specimen was also reported by Wiegand [38]. This is because the region of the specimen below the impactor is the one where the material is subject to the highest stresses and strains. Moreover, being UD carbon/epoxy composites anisotropic material with lower compressive properties compared to the tensile one [32], compressive failure was expected. For the specimens with a thicknesses of 1.5 and 2 mm, once fibre kinking occurred the specimen nearly instantaneously split in two parts. Specimens with thickness of 2.5, 3 and 3.5 mm tested with both support spans and specimens with thickness of 4 mm tested with a support span of 60 mm showed a fibre tensile final failure. An example is shown in Figure 3.16. After the initial fibre kinking the fracture propagates through the specimen thickness. This event results in a reduction in the applied load or in a plateau where the applied load remains constant. Once the tensile failure strain is reached on the tensile surface of the specimen, tensile fibre breakage occurs. The result is a sharper decrease in the load signal. Specimen with thickness of 4.5, 5 and 5.5 mm tested with both support spans and specimens with thickness of 4 mm tested with a support span of 80 mm showed delamination as final failure mode. An example is shown in Figure 3.17. Once fibre kinking occurs on the compression side, the applied load remains constant while the fracture propagates through the thickness. At the occurrence of delamination the load signal goes instantaneously to zero as the specimen is split in two parts. This behaviour is due to the fact that, as the ratio between specimen thickness and support span decreases, the influence of shear stresses increases [36, 47]. The failure behaviour is summarised in Table 3.4.

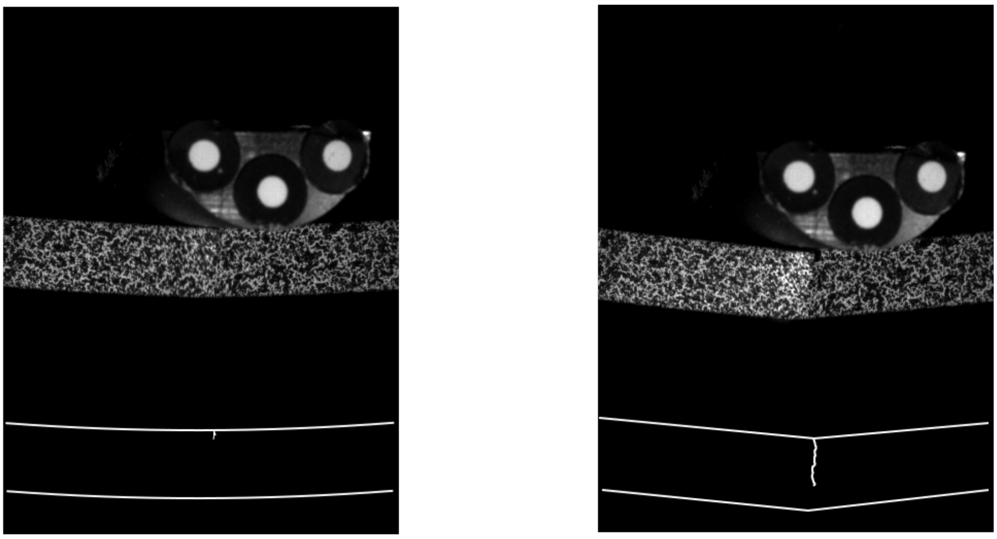

(a) Fibre kinking

(b) Compressive failure through the thickness

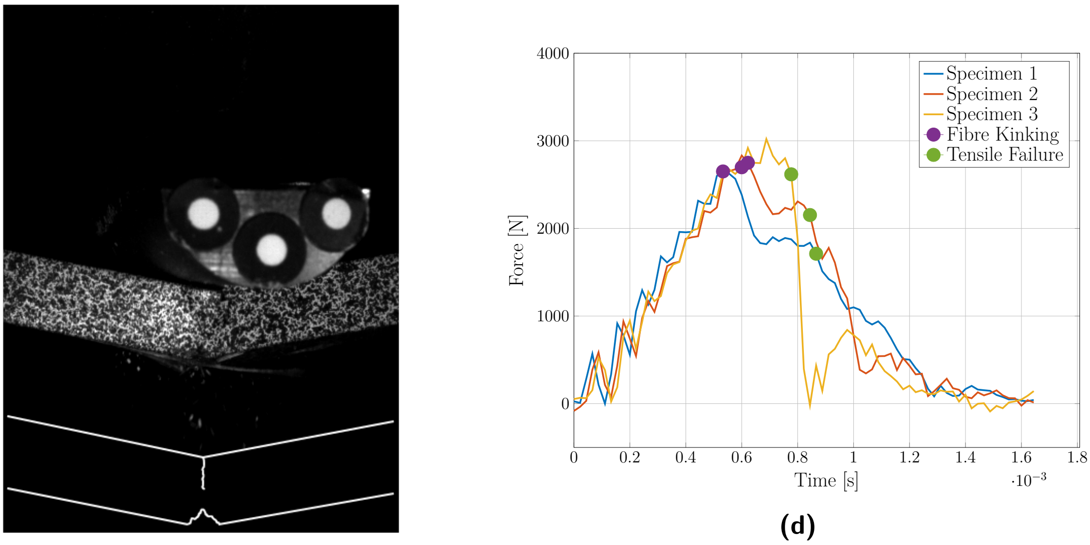

(c) Tensile fibre failure

(d)

Figure 3.16: Failure mechanism of $3.5\,\mathrm{mm}$ thick specimen tested with a support span of $60\,\mathrm{mm}$ at a velocity of $5\,\mathrm{m/s}$

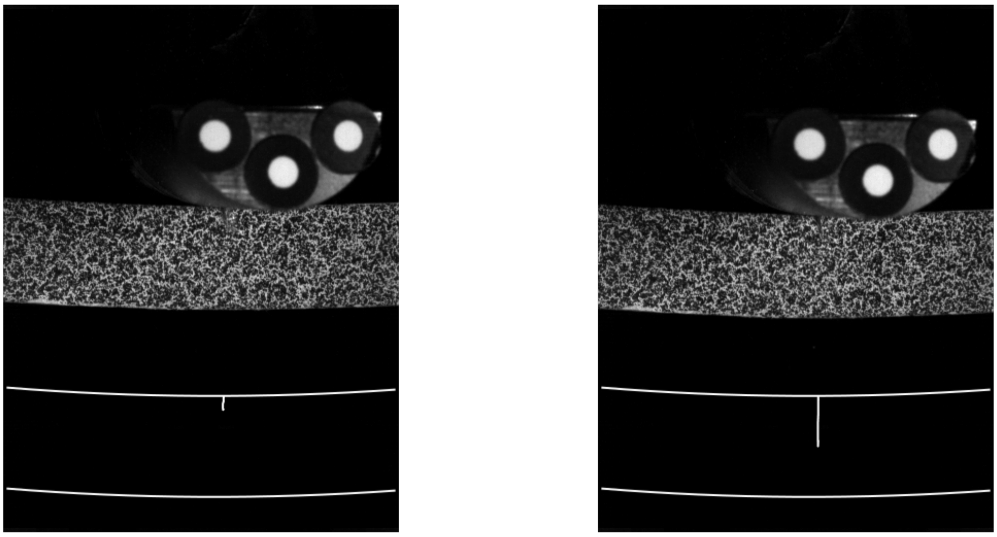

(a) Fibre kinking

(b) Compressive failure through the thickness

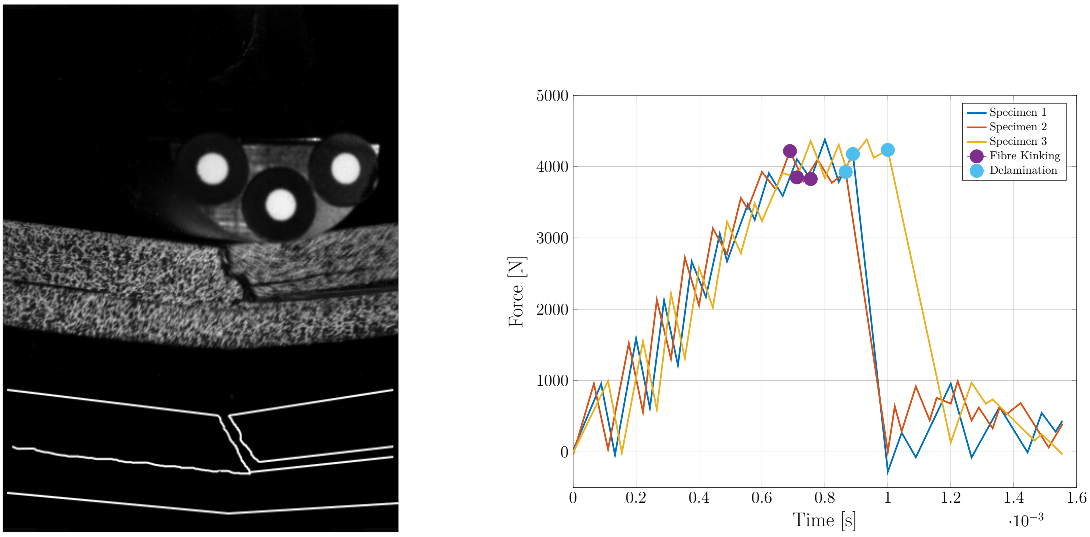

(d)

(c) Delamination

Figure 3.17: Failure mechanism of $5\,\mathrm{mm}$ thick specimen tested with a support span of $80\,\mathrm{mm}$ at a velocity of $5\,\mathrm{m/s}$

Table 3.4: Specimen failure mechanism.

Thickness [mm]	Support Span [mm]	Failure Initial	Failure Final
1.5	80 60	Fibre kinking	/
2.0	80 60	Fibre kinking	/
2.5	80 60	Fibre kinking	Tensile fibre failure
3.0	80 60	Fibre kinking	Tensile fibre failure
3.5	80 60	Fibre kinking	Tensile fibre failure
4.0	80 60	Fibre kinking	Delamination Tensile fibre failure
4.5	80 60	Fibre kinking	Delamination
5.0	80 60	Fibre kinking	Delamination
5.5	80 60	Fibre kinking	Delamination

3.3.5 Maximum Force

The test results were analysed in terms of force and displacement when fibre kinking occurred; at this point the maximum load was reached. A total of three replicates were tested under each configuration. The pictures and the data coming from the strain gauges were combined together using the DIC software ARAMIS®, which also allowed computing the parameters of interest from the pictures. As output the software gave a .csv file for each test performed. A Matlab algorithm was implemented in order to analyse the data coming from all the tests and to create the desired plots.

The maximum force coming from the smoothed force signal is summarised in Figure 3.18. In particular, Figure 3.18a summarises the data from the tests performed with the 80 mm support span, while Figure 3.18b displays the data from the tests performed with the 60 mm support span. For each specimen thickness, the bar plots display the maximum load reached at every velocity tested. As three replicates were performed, the displayed value is the average of the three tests and the error is given as the standard deviation. Even though the designed fixture is not suitable to test thin laminates, specimens with thickness from 1.5 to 3 mm were tested because this thickness range is the most used for material characterisation at the Audi laboratory. These specimens are the ones which show high variation in maximum force and there is no delineated trend in the maximum force as the testing velocity increases. This is mainly observed for tests with the larger support span. As general trend, specimens with a thickness higher that ≥ 3 mm show an increase of maximum load with increasing testing velocity. When the support span is 80 mm, this is true up to testing velocities of 5 m/s. For example, for the specimens with thickness of 4 mm and 3.5 mm, at high velocities the maximum force decreases compared to the one obtained at 5 m/s. Another outcome is that high deviation in the results is observed, as for specimen with thickness of 4.5 mm and 5.5 mm. This behaviour could be due to specimen vibrations during testing. Results obtained with the smaller support span show a more homogeneous increasing behaviour.

To better understand the increase in maximum load, Figure 3.19 shows the force normalised with respect to the corresponding quasi-static load. The lowest two thicknesses have been discarded in Figure 3.19, because they are not suitable for the designed fixture, as described above. The testing velocity highly influences the test results as the increase in maximum force is higher than 20% percent for all velocities. There is already a large gap in test results between quasi-static tests and tests performed at 0.1 m/s and 0.5 m/s. It would be of interest to investigate behaviour at lower testing velocities. Between the two support spans, the 60 mn support span is the one that shows more consistency in the results, specially for thickness higher than 3 mm.

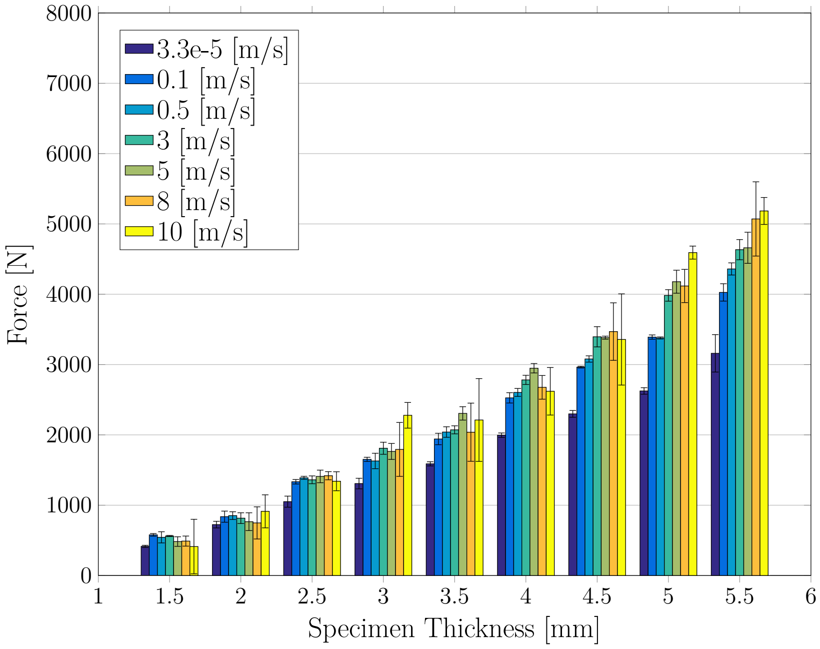

(a) Support span= 80 mm

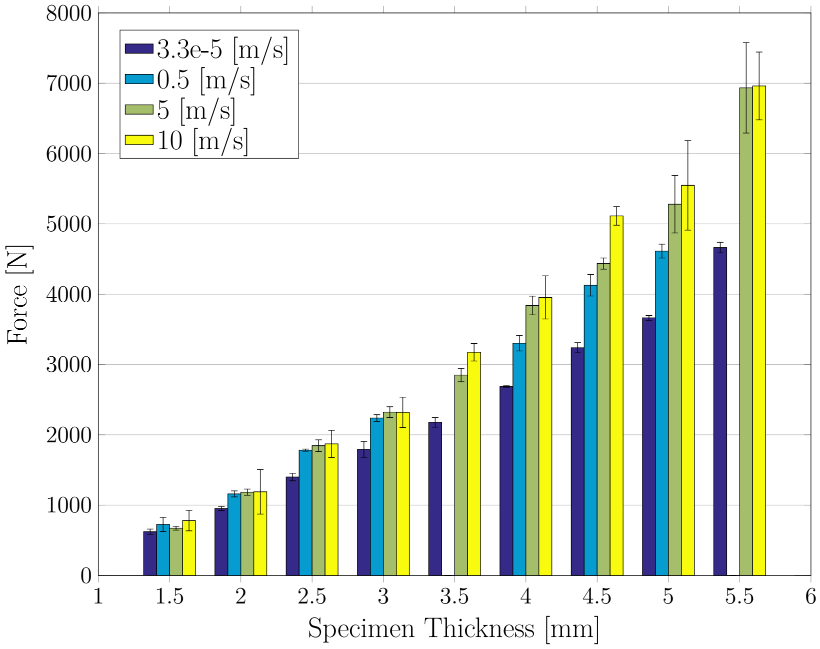

(b) Support span = 60 mm

Figure 3.18: Maximum force.

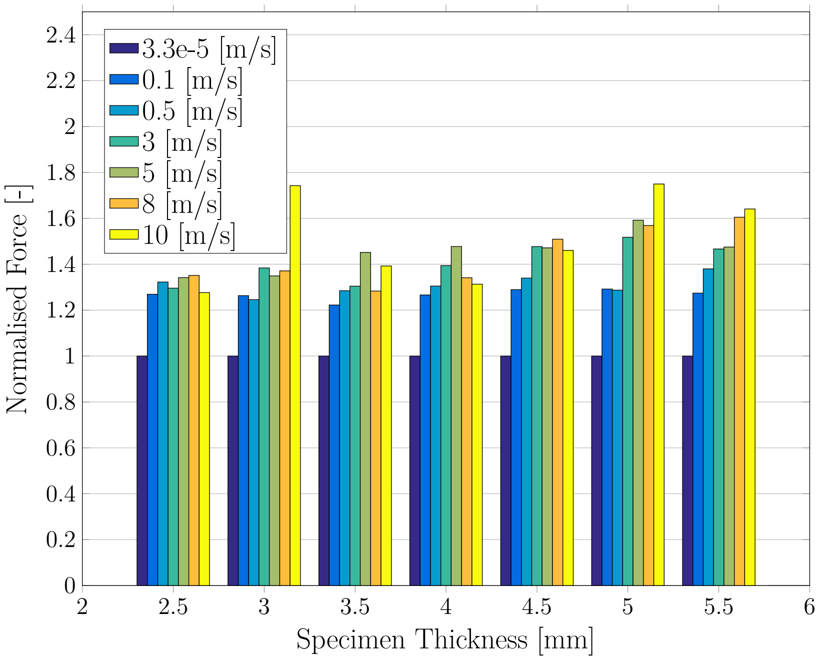

(a) Support span= $80\,\mathrm{mm}$

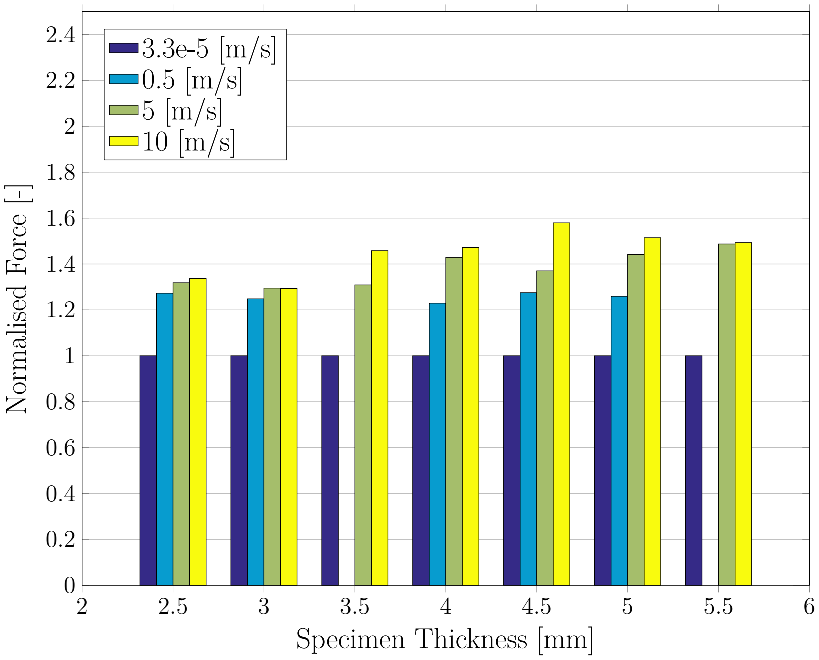

(b) Support span $= 60\,\mathrm{mm}$

Figure 3.19: Normalised maximum force.

3.3.6 Maximum Displacement

The specimen displacement was obtained from the analysis of the pictures taken with the high speed cameras. The results are shown in Figure 3.20. As expected, the mid point displacement decreases with the increase in specimen thickness. This is due to an increase in the beam stiffness. As a result, increasing the testing velocity gives an increase in maximum displacement. For thicknesses higher than 3.5 mm the maximum displacement for tests performed at 10 m/s is in all cases nearly twice as much as the displacement measured in quasi-static conditions. This behaviour is observed regardless of the support span.

In Figure 3.21 the relationship between the specimen midpoint displacement and the testing velocity is shown. The general trend is an increase in displacement with increasing testing velocity. In all tests performed the results show a high increase in specimen displacement between the quasi-static velocity and low testing velocity of 0.1 m/s for support span of 80 mm, and between the quasi-static velocity and low testing velocity of 0.5 m/s for support span of 80 mm. The increase between the other testing velocities is not as steep, and the curves have a tendency to flatten. This behaviour suggests a logarithmic relationship between the specimen mid point displacement at failure and the testing velocity.

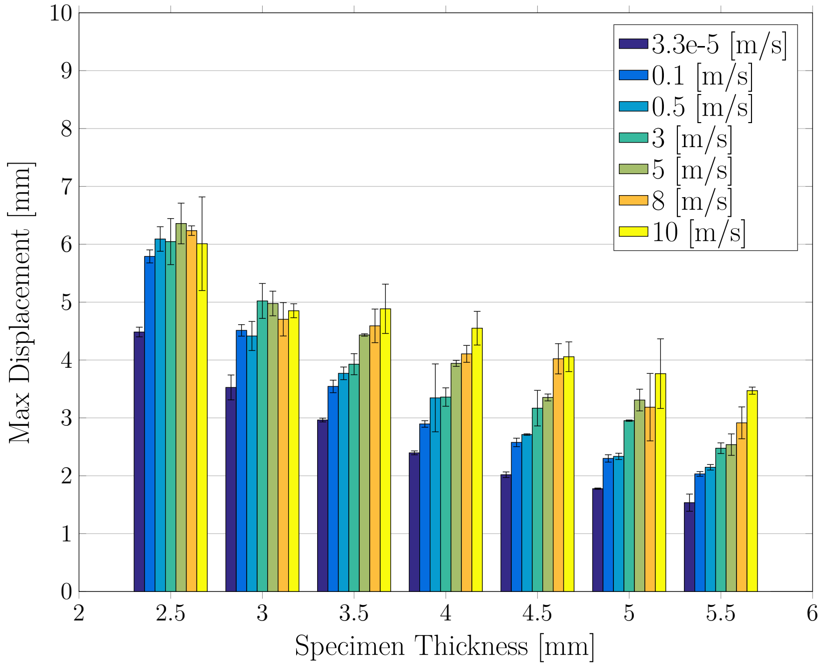

(a) Support span= 80 mm

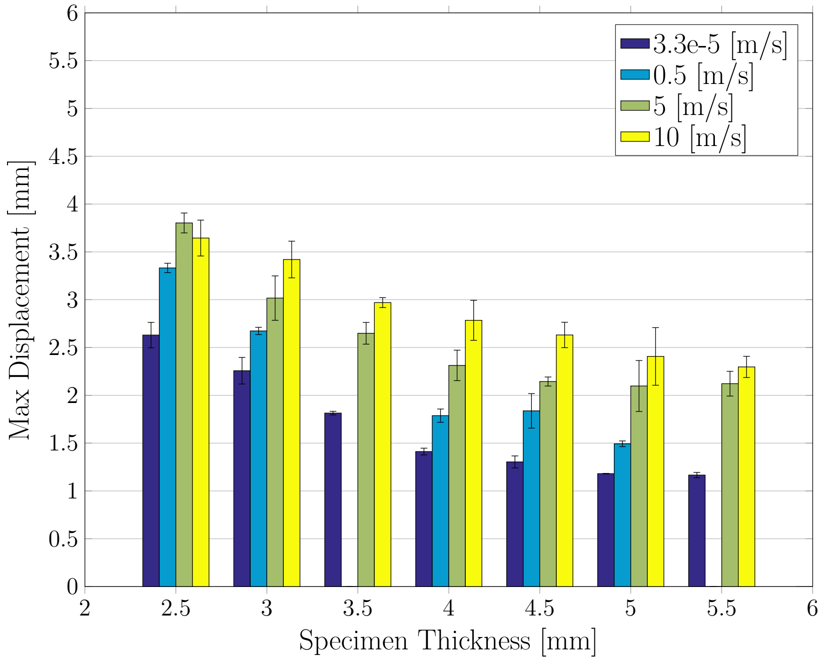

(b) Support span = 60 mm

Figure 3.20: Maximum displacement.

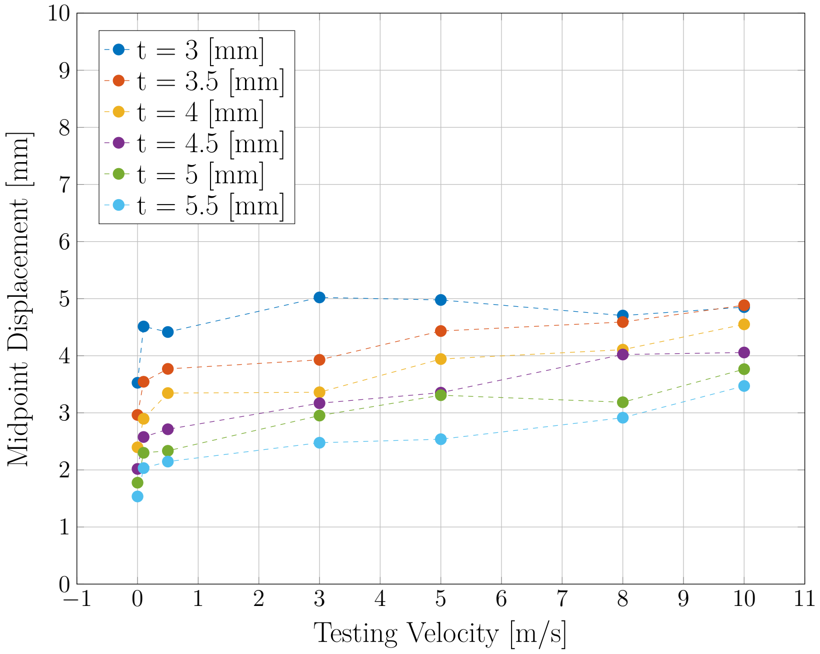

(a) Support span = 80 mm

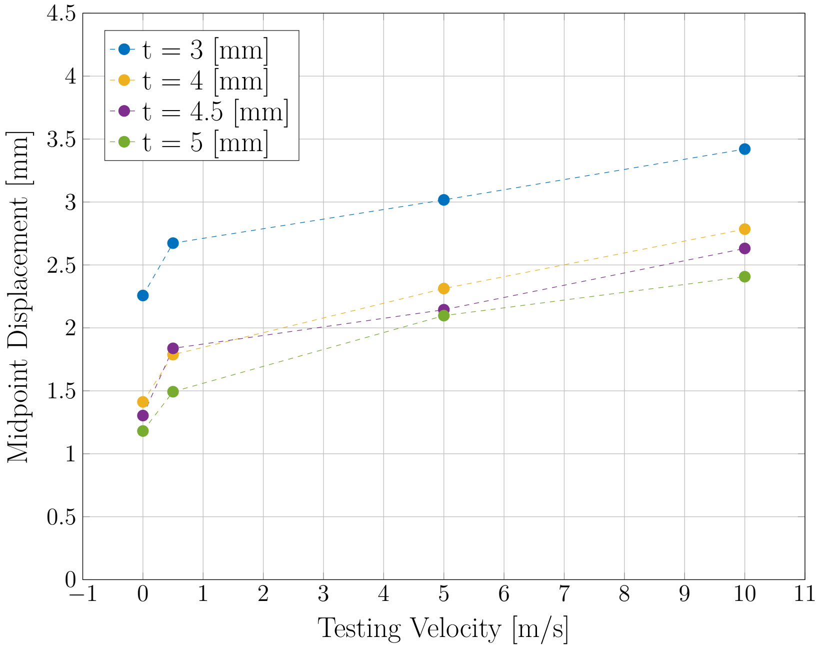

(b) Support span = 60 mm

Figure 3.21: Specimen displacement vs. testing velocity.

3.3.7 Coefficient of Variation

To assess the variability of the test results the coefficient of variation (CV) was computed for the maximum force and the maximum midpoint displacement at failure. The CV allows to determine the dispersion of a data set relative to the sample mean. This coefficient is obtained as the ratio between the sample standard deviation and the sample mean

$$\mathrm{CV} = \frac{\text{Standard Deviation}}{\text{Mean}} \tag{3.4}$$

The CV can be used instead of the standard deviation. By normalising the standard deviation with respect to the corresponding mean, it is possible to compare data with different means. It is a unitless quantity, thus also quantities with different units can be compared using this coefficient.

The coefficients of variation computed are displayed in in the bar plots in Figure 3.22, which is representative of the CVs for the maximum force and the maximum midpoint displacement at failure at both support spans. For both the maximum force and the midpoint displacement at failure, most of the CVs were lower that 0.1. Higher values are reached for some test setups especially at the highest testing velocity. Concerning the force measurements, it was generally observed the larger support span gives a higher variation of test results in particular at high testing speeds. A particular trend was not observed in the CVs obtained from the displacement measurements. Higher peaks were observed for test results obtained with the support span of 80 mm.

To better understand the influence of the specimen thickness on the test results, the average of the CVs obtained for testing velocities tested at both support spans was computed for each specimen thickness. The testing velocities considered were therefore 3.3×10^{-5}, 0.5, 5 and 10 m/s. The results are shown in Figure 3.23. For both support spans the CV decreases with increasing thickness. However, after reaching a minimum value, it increases again. The minimum was obtained at the thickness value of 5 for tests with the support span of 80 mm, and at a thickness value between 3.5 mm and 4.5 mm or tests with the support span of 60 mm. No general trend was observed for the CVs related to the displacement results. At each thickness the coefficients of variation from both support spans were comparable.

To determine the influence of the support span on the test results, the average of the CVs obtained for all the specimen thicknesses at the common testing velocities for both support spans was computed for each support span. The results are shown in Figure 3.24. The reduction in the support span had a higher influence to the CVs related to the force measurements, compared to the ones obtained from the displacement measurement. The CV for the force measurements reduced from 0.094 at 80 mm to 0.094 at 60 mm. This was probably due to the increase in the global stiffness with a lower support span, which leads to lower specimen vibrations. The CV for the displacement measurements remained in both cases in the range between 0.05 and 0.06.

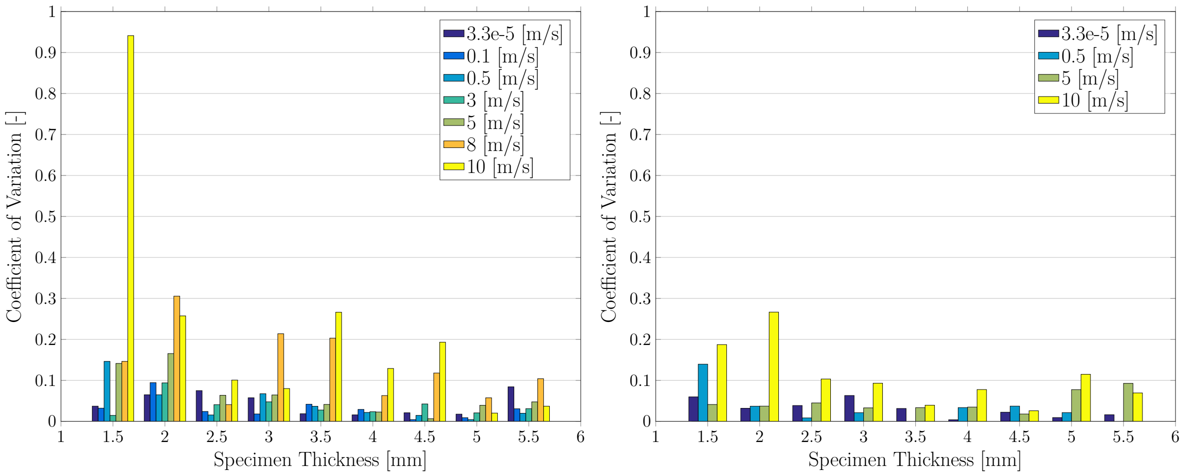

(a) Support span $= 80\,\mathrm{mm}$ - Force **(b)** Support span $= 60\,\mathrm{mm}$ - Force

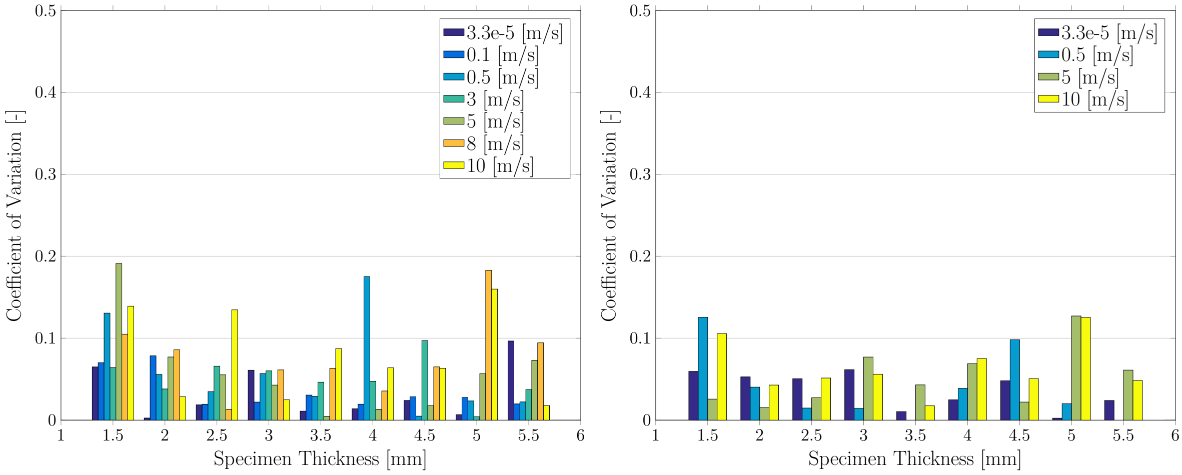

(c) Support span $= 80\,\mathrm{mm}$ - Displacement **(d)** Support span $= 60\,\mathrm{mm}$ - Displacement

Figure 3.22: Coefficient of variation of the maximum force (a, b) and maximum displacement (c, d) at failure

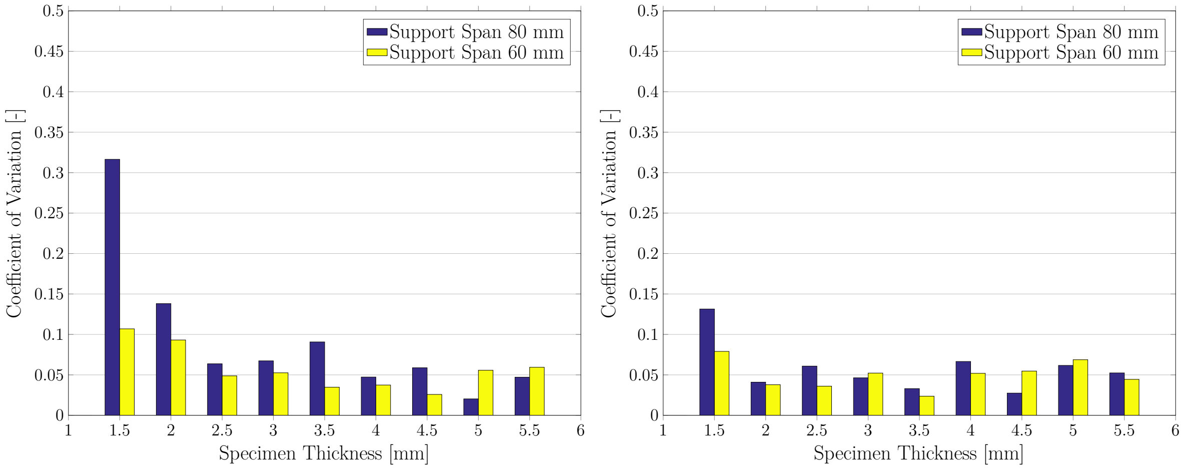

(a) Force **(b)** Displacement

Figure 3.23: Mean values of the coefficient of variation of the maximum force (a) and maximum displacement (b) at failure for the testing velocities common to both support spans.

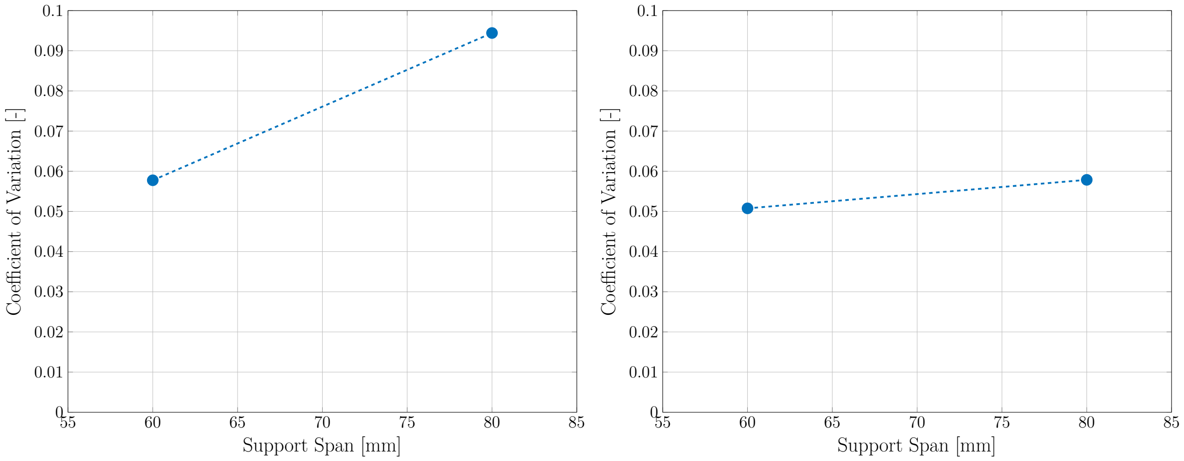

(a) Force **(b)** Displacement

Figure 3.24: Mean values of all the coefficient of variation of the maximum force (a) and maximum displacement (b) at failure for the testing velocities common to both support spans.

3.4 Conclusions

In this section the conclusions based on the results presented in this chapter are drawn. The testing equipment consisting in the testing high-rate servo-hydraulic testing machine, the high-speed cameras, and the DIC software used for data analysis have been presented. The new designed fixture for dynamic 3-point bending tests has been described in detail. Finally, the test results have been displayed and analysed.

The designed fixture allowed correctly measuring the load applied by the impactor on the specimen at every testing speed. It was necessary to filter the output signal, as it showed oscillations due to noise in the setup. The use of high-speed cameras, combined with the DIC software ARAMIS®, allowed to easily obtain the specimen midpoint displacement and the impactor displacement and velocity. Thanks to this data it was possible to notice that after the initial impact the contact is lost between specimen and impactor, as shown in Figure 3.14 and Figure 3.15. This induced vibrations on the specimen. In order to reduce this effect it is possible to increase the specimen thickness or to reduce the support span. The latter solution is the most effective, because it increases the specimen global stiffness. As a result, the detachment between specimen and impactor, and the specimen vibrations are reduced.

All specimens tested failed starting with with fibre kinking on the compression side of the specimen. The location is in the area of contact with the impactor, as it is the region of the specimen where the highest strains are reached. Depending on the specimen thickness, the final failure can be tensile fibre failure or delamination. Generally, there is no increase in load after initial fibre kinking, therefore this point was chosen as specimen failure; maximum load and displacement are the ones measured when fibre kinking occurs. Table 3.4 (Section 3.3.4) is a summary of the failure modes.

Both the maximum load at failure and the specimen midpoint displacement at failure increase at every testing velocity compared to the values obtained at quasi-static tests. The increase in the maximum load for every combination of specimen thickness and support span compared to the relative quasi-static one is always above 20%. The general trend is the increasing maximum load at failure for increasing testing speed. This behaviour is especially observed in tests performed with the support span of 60 mm, which minimises the specimen detachment from the impactor and therefore the specimen vibrations. The reason is due to the fact that, if the specimen is considered as a simply supported beam, with the lower support span the beam stiffness increases if compared to the larger support span. The specimen midpoint displacement at failure always increased with increasing testing speed. It was found that the midpoint displacement showed an increase when plotted versus the testing velocity, as shown in Figure 3.21.

The coefficient of variation analysis did not show a specific trend regarding the results obtained from the displacement measurement. Of more interest are the ones obtained for the force measurements. As shown in Figure 3.23a, it seems that for both support spans the CVs reach a minimum. The minimum value is obtained for specimen 5 mm thick at the support span of 80 mm, and for specimen 4.5 mm thick at the support span of 60 mm. The support span also influences the CV. A lower CV is obtained for tests performed with the support span of 60 mm one. It seems that the best setup is obtained when the specimen has a thickness between 3.5 mm and 4.5 mm, and the support span is 60 mm. This setup allowed to obtain a low coefficient of variation.

Chapter 4

Estimation of the Maximum Testing Velocity

In this chapter the tool developed to determine the maximum testing speed which can be used for testing with a specific setup is presented. Section 4.1 presents the reason that led to the implementation of the Matlab tool. Section 4.2 describes the approach used to compute the global stiffness of a simply supported beam and the method used to determine the goodness of the test results. Section 4.3 shows the behaviour of the Coefficient of Determination R^2 as function of some testing parameters. Section 4.4 presents how the maximum testing velocity for any value of global stiffness is obtained. Finally, the conclusions based on the content of this chapter are presented in Section 4.6.

4.1 Motivation

The test performed and the results presented in Chapter 3 showed a high dependency of maximum force and maximum midpoint displacement on the testing velocity. It was concluded that, for the unidirectional carbon/epoxy composite tested, the best configuration would be the one that has a support span of 60 mm and a thickness between 4 and 4.5 mm. These configurations were the ones that gave low standard deviation in the test results and minimised the specimen detachment from the impactor.

The testing velocity influences the reliability of the test results. As shown in Figure 4.1a and Figure 4.2a, the CV showed an increasing trend with increasing testing velocity. As shown in Figure 4.5 in Section 4.2.2, the force-displacement plot had a linear increasing behaviour. It was therefore possible to interpolate such curve with a linear regression to assess such linear trend. The goodness of the fitting curve was measured by the coefficient of determination (CD) R^2. Figure 4.1b and Figure 4.2b show the influence of the testing velocity on the CD. For both support span, the CD decreased with increasing testing velocity. When the testing velocity increased the specimen detachment from the impactor and the specimen vibration led to higher variation in the measurements of the fracture force and to a decrease of the coefficient of determination.

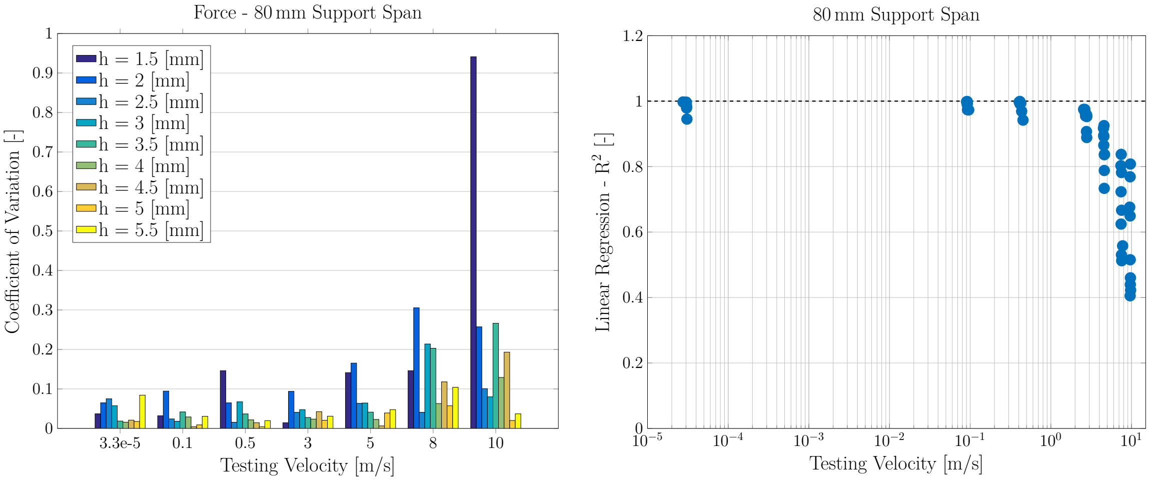

(a) **(b)**

Figure 4.1: Variation of the CV of the maximum force at failure (a) and R^2 (b) according to the testing velocity for tests performed with the support span of 80 mm.

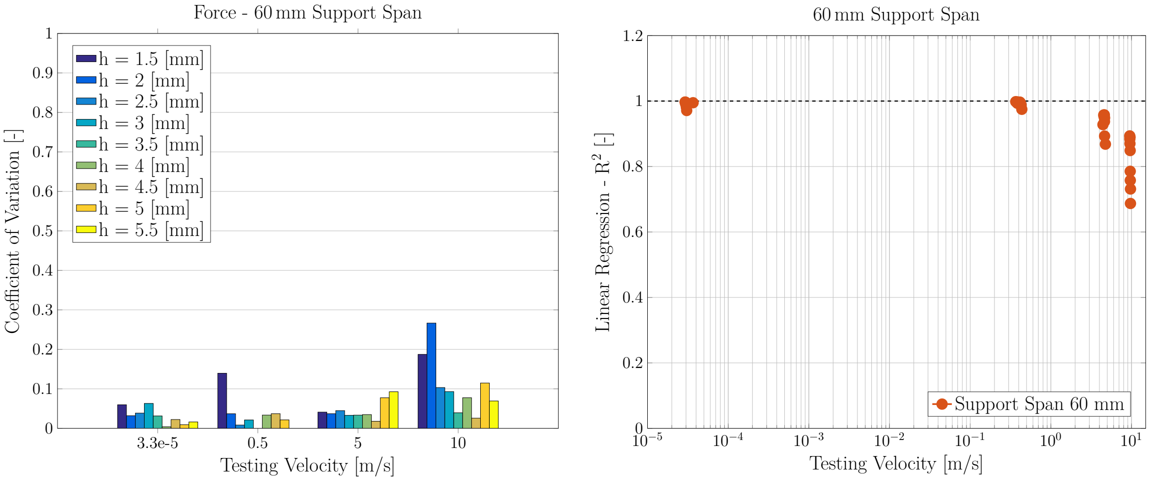

(a) **(b)**

Figure 4.2: Variation of the CV of the maximum force at failure (a) and R^2 (b) according to the testing velocity for tests performed with the support span of 60 mm.

A variety of composite materials are tested in the Audi laboratory. Each composite can vary depending on several parameters:

- layup - the layup can be UD, biaxial [0/90], quasi-isotropic $[45/-45/0/90]$, etc.;
- thickness - depending on the manufacturing method (prepreg combined with an autoclave cycle for curing or the use of resin transfer moulding process) the specimen

thickness can change from the optimal one;

- fabric type - the composite fabric can be UD, woven, non-crimp fabrics, or multiaxial;
- matrix type - the composite matrix can be thermoset or thermoplastic

For these reasons it might not be possible to create a specimen which has the optimal geometry for the test setups. It was therefore required to create a method which would allow estimating the maximum testing speed to be used for different combinations of test parameters.

4.2 Approach

In this section the approach used to estimate the maximum testing velocity which leads to reliable test results is presented.

4.2.1 Global Beam Stiffness

In order to compare specimens with different testing parameters, the specimen was considered as a simply supported beam. This allowed correctly modelling the specimen boundary conditions. The load applied by the impactor is considered as a concentrated force acting at the beam midpoint, as shown in Figure 4.3.

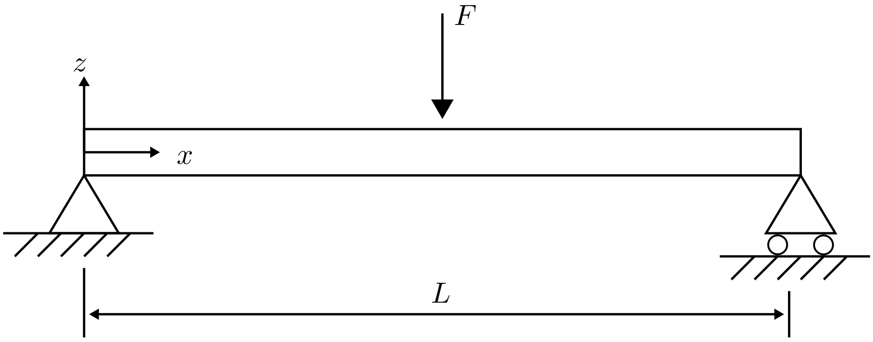

Figure 4.3: Simply supported beam.

Due to the simply supported conditions, it is possible to determine the beam global stiffness, which depends on the support span, the specimen thickness, and the specimen layup. To determine the beam global stiffness it is required to compute the beam displacement.

Under the applied load the beam deforms, as shown in Figure 4.4. The beam midpoint corresponds to the point of maximum displacement. Such displacement can be computed using the classical beam theory (CBT).

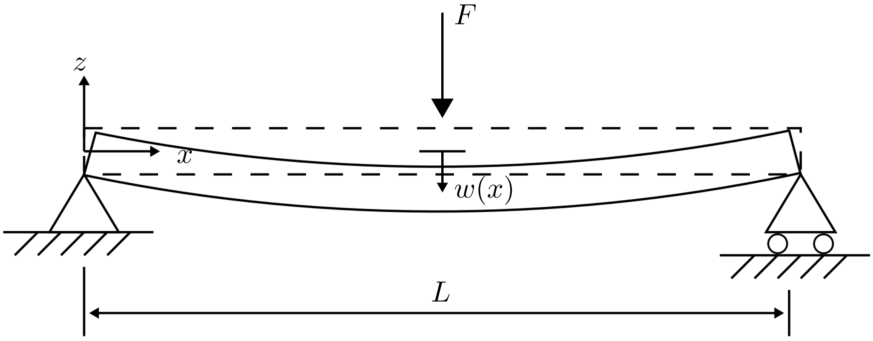

Figure 4.4: Deformed simply supported beam.

The displacement $w(x)$ for any point along the beam length from CBT is obtained as

$$w\left(x\right)=\left[\frac{x^3}{12\left(EI\right)_{beam}}\right]F_{max} \tag{4.1}$$

where $(EI)_{beam}$ is a property of the beam, which depends on the beam thickness, width and layup, and F_{max} is the maximum load reached at the specimen failure.

The maximum displacement is obtained at the beam midpoint. Substituting $L/2$ into Equation 4.1 the maximum displacement is obtained as

$$w\left(x=\frac{L}{2}\right)=w_{max}=\left[\frac{L^3}{48\left(EI\right)_{beam}}\right]F_{max} \tag{4.2}$$

The above equation can be inverted in order to make the force explicit. The maximum force will thus depend on the displacement and on a constant parameter as shown in the equation below

$$F_{max}=\left[\frac{48\left(EI\right)_{beam}}{L^3}\right]w_{max}\quad\rightarrow\quad F_{max}=K_{beam}\,w_{max} \tag{4.3}$$

The term K_{beam} has the units [N/mm]. It is an indicator of the beam global stiffness. It takes into account the boundary condition and the way the load is applied, and the specimen parameters through the term $(EI)_{beam}$. For composites such term includes material and geometrical properties of the beam. To compute it, the equation provided by Kassapoglou [48] was used and it is shown below.

$$\left(EI\right)_{beam}=E_b\left[\frac{b\ h^3}{12}+b\ h\ d\right] \tag{4.4}$$

The above equation is referred to beams which consist of several members, for example I or L stiffeners. The term E_b is the bending stiffness of the specimen which depends only on the specimen layup and the material properties, b is the beam width, h is the beam thickness. The term d is the distance of the member neutral axis from the stiffener neutral axis. For a UD laminate with a rectangular cross-section such term is zero. The specimen bending stiffness is obtained as

$$E_b = \frac{12}{h^3\ d_{11}} \tag{4.5}$$

where d_{11} is the entry (3,3) of the inverted ABD matrix.
By combining Equations 4.3, 4.4 and 4.5 the beam global stiffness is

$$K_{beam} = \frac{48\ b}{d_{11}\ L^3} \tag{4.6}$$

Equation 4.6 is the one used to compute the stiffness for each specimen tested. This allowed comparing the test results from different configurations with respect to a unique term.

4.2.2 Linear Regression of the Force-Displacement Curve

The test results of 3PB tests of UD carbon fibre composites show a linear relation between force and displacement, this is because of the linear tensile and compressive behaviour of the carbon fibres. Also the tests performed in this study showed this behaviour, as seen in Figure 4.5. However, as the testing velocity increases, the data show oscillations and an initial peak is observed. The peak is the outcome of the impact between the impactor and the specimen. It affects the linearity of the force-displacement curve.

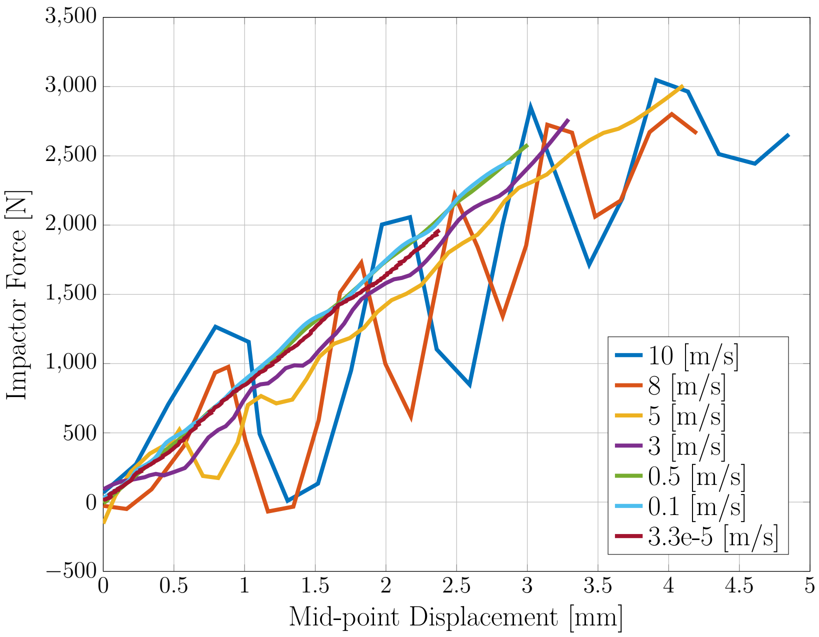

Figure 4.5: Support span= 80 mm

To assess the curves linear behaviour, a linear regression that starts from the origin was used to fit the data. The goodness of fit was determined using the coefficient of determination R^2.

$$y = m\,x \qquad\qquad R^2 = 1 - \frac{SS_{res}}{SS_{tot}} = 1 - \frac{\sum_i (y_i - f_i)^2}{\sum_i (\bar{y} - y_i)^2} \tag{4.7}$$

where, for each curve, m is the slope of the fitting line, f_i is the force value obtained from the test, y_i is the force value coming from the linear regression, and $\bar{y}$ is the average force value obtained from the test.

4.3 Coefficient of Determination - R^2

The coefficient of determination was used to assess the goodness of the fitting linear regression with respect to the force-displacement curves resulted from the tests. The R^2 parameter has a maximum value of 1, which represents a perfectly linear behaviour, and decreases as the behaviour deviates from the linear one. The effect of the testing velocity and thickness on R^2 is shown in Figure 4.6, which is representative of both support spans. The testing velocity is on a logarithmic scale; figures 4.6a and 4.6b show that as the testing speed increases the coefficient of determination decreases. A similar effect is observed on the thickness effect, as the thickness increases R^2 increases. It can be deduced that at high speed the force-displacement linear fitting is not optimal, because of specimen vibration. The higher thicknesses, when compared at the same testing velocity, have a better R^2 because of reduced detachment of the specimen from the impactor.

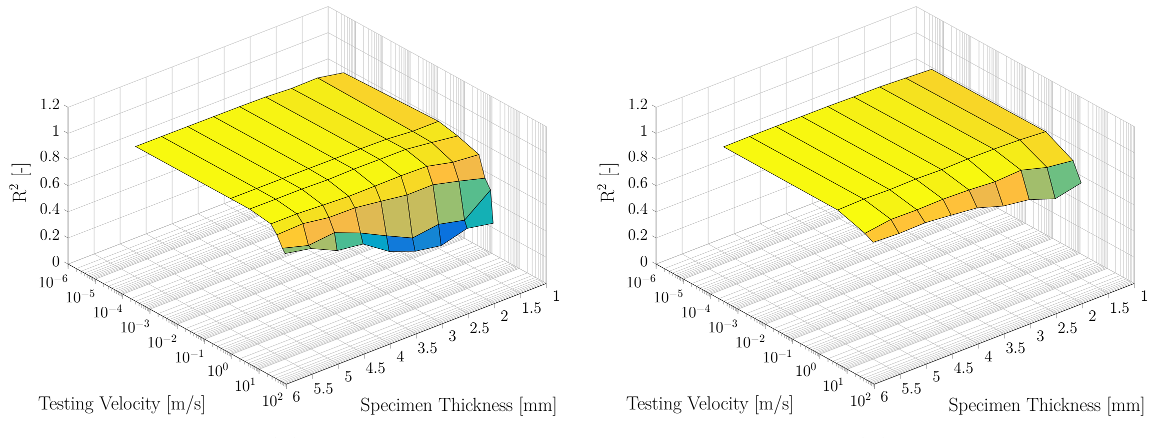

(a) **(b)**

Figure 4.6: Variation of the coefficient of determination according to testing velocity and to specimen thickness for support span of (a) 80 mm and (b) 60 mm.

Figure 4.7 is representative of the thickness effect on R^2. The general behaviour is an increase of R^2 for increasing thickness. At low testing velocity the thickness has a small influence, as R^2 is higher than 0.9 for testing velocities lower than 5 m/s at both support spans. As the testing velocity increases, the increase in thickness has a positive effect. For a support span of 80 mm tested at 10 m/s, the R^2 for the thickest specimen is nearly twice as much as the one computed for thin specimens. A similar effect is also observed in tests performed with the support span of 60 mm. In this case the increase in R^2 is not as high as in the previous case, because the reduced support span increases the beam global stiffness, giving a reduction in the specimen vibrations, already for thin specimens.

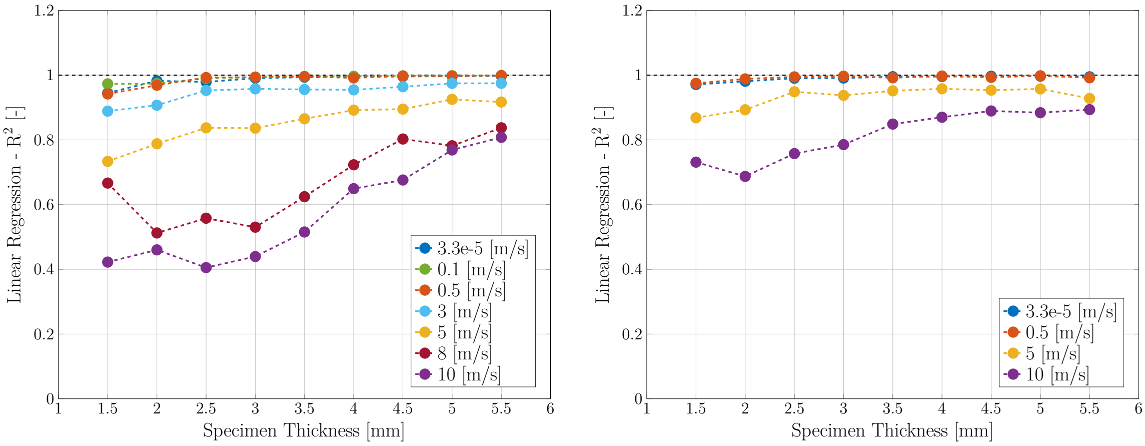

(a) **(b)**

Figure 4.7: R^2-specimen thickness relation for support span of (a) 80 mm and (b) 60 mm.

The support span therefore increases the coefficient of determination. The reduction in the support span has a positive effect at all velocities tested, as shown in Figure 4.8. The increase in R^2 was low for low testing velocities, as R^2 was already approximately 0.98 for the support span of 80 mm. A high increase in R^2 is observed for high velocities. At 10 m/s the coefficient of determination increases from 0.57 to 0.82, suggesting a better fit of the test results.

The effect of the testing velocity on R^2 is shown in Figure 4.9. The testing velocity has a low influence on the coefficient of determination up to the speed of 0.5 m/s. Starting from the results obtained from tests at 3 m/s, the computed R^2 dropped and the minimum values were reached at the highest tested velocity.
This trend shows that it can be identified a threshold value for R^2, below which the increase in testing velocity produces a drop in R^2, due to the specimen detachment and vibrations. As this leads to fluctuations in the force signal, the test results obtained cannot be considered reliable. This approach was chosen to determine the maximum testing speed, which leads to low detachment and vibrations in the specimen, for a specific value of global stiffness.

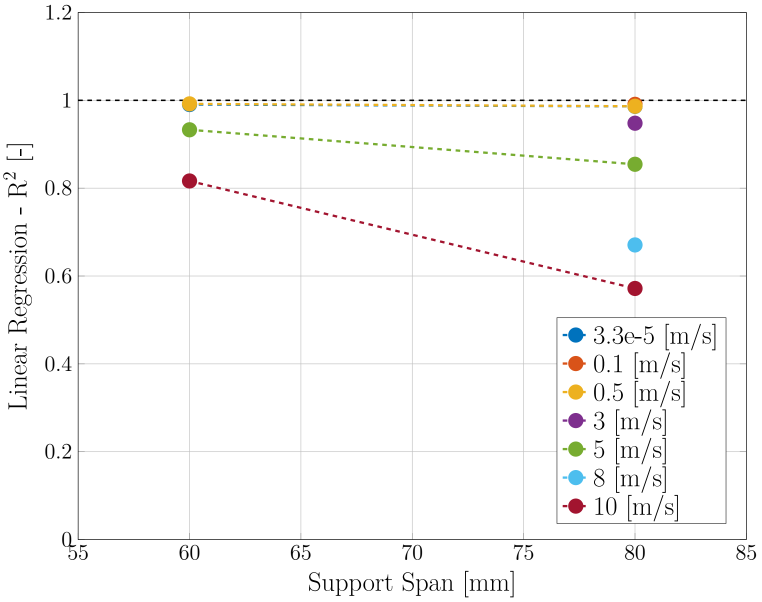

Figure 4.8: Effect of the support span on R^2.

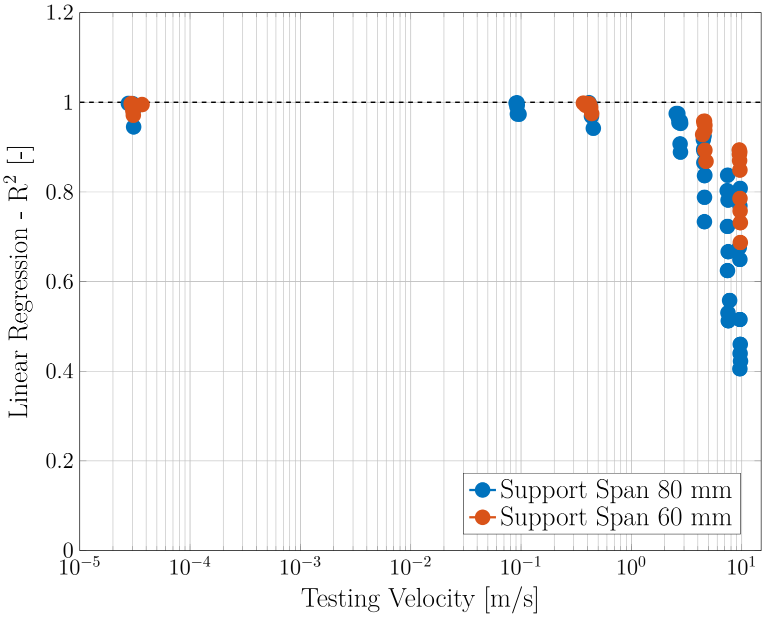

Figure 4.9: Effect of the testing velocity on R^2.

4.4 Maximum Allowed Testing Velocity

The approach described in the sections above is here used to determine the maximum allowed testing velocity for a specific specimen stiffness. Equation 4.6 was used to compute the global stiffness for each combination of support span and specimen thickness which were tested. The results are shown in Table 4.1. By reducing the support span the global stiffness of the simply supported beam increased approximately 2.4 times, when the thickness remained constant.

Table 4.1: Simply supported beam global stiffness.

Thickness [mm]	Global Stiffness - K_{beam} [N/mm]	
	Support Span 80 mm	Support Span 60 mm
1.5	52.2	123.8
2.0	114.7	271.9
2.5	256.5	608
3.0	417.7	990
3.5	635.2	1505.7
4.0	1027.6	2435.8
4.5	1409.6	3341.2
5.0	1876.2	4447.2
5.5	2644.4	6268.3

To estimate the maximum testing velocity, the R^2-testing velocity plots were created for all the values of global stiffness displayed in Table 4.1. The data points were interpolated using polynomial and exponential interpolation functions, as shown in Figure 4.10. The Matlab® built-in functions used were *polyfit* and *fit*. The function *polyfit* uses the least squares method to obtain the best fitting polynomial of the order required. The corresponding equations are:

$$\begin{aligned} &\text{Polynomial:} \quad p\left(x\right) = p_1 x^n + p_2 x^{n-1} + ... + p_n x + p_{n+1} \\ &\text{Exponential:} \quad f\left(x\right) = a\ e^{bx} + c\ e^{dx} \end{aligned} \tag{4.8}$$

The order of the fitting polynomial is n. It should be equal or lower than the total number of the data points available minus one [49]. This allows to obtain a fitting polynomial that is unique. Despite the fact that the number of data points available for the tests performed at 60 mm support span was 4, the maximum polynomial order considered was $n = 4$. The polynomial of the 4^{th} was obtained also for the tests performed at 60 mm support span, but due to the fact that it is not unique it was not considered as a possible fitting polynomial.

To determine which was the best fitting law, the plots referring to all the global stiffness tested were analysed. An example is shown in Figure 4.10, where the results obtained for the specimen thickness of 3 mm are shown for each support span.

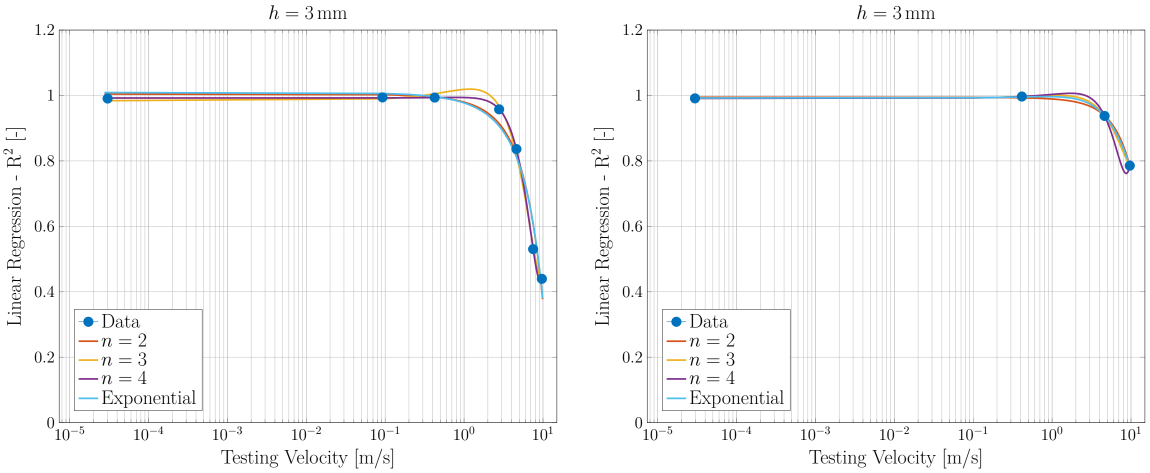

(a) **(b)**

Figure 4.10: Fitting curves for prediction of the maximum allowed testing velocity for 3 mm thick specimens with the support span of (a) 80 mm and (b) 60 mm.

Figure 4.10a is representative for tests performed with the support span of 80 mm. It is possible to see that the 2^{nd} order polynomial and the exponential fitting curve underestimate the results obtained between the testing velocities of 0.5 and 5 m/s. On the other hand, the 3^{rd} order polynomial overestimates the R^2 for testing velocities between 0.5 and 3 m/s. It gives values > 1, which are above the maximum limit of 1 that can be reached by R^2. For these reasons the 4^{th} order polynomial was chosen to interpolate the data obtained from tests performed with 80 mm support span.

Figure 4.10b is representative for tests performed with the support span of 60 mm. In this case both the 3^{rd} and the 4^{th} order polynomial reached values of R^2 grater than 1 for testing velocities between 0.5 and 5 m/s. The 2^{nd} order polynomial slightly underestimated R^2 for testing velocities around 0.5 m/s. For these reasons the exponential fitting law was chosen to interpolate the data obtained from tests performed with 60 mm support span.

The fitting curves relative to all the specimen thicknesses tested are shown in Figure 4.11. As the specimen thickness increases, the fitting curves shift upward and the decrease in R^2 is less steep. This behaviour was observed for both support spans and it shows that at a fixed testing velocity a higher R^2 can be obtained for stiffer specimens (the global stiffness is related to the specimen thickness and the support span as shown in Table 4.1). There was only one exception to this trend: the results obtained from 5.5 mm thick specimen tested with a support span of 60 mm. The corresponding fitting curve is the black line in Figure 4.11b and Figure 4.12.The latter figure shows the behaviour more in details.

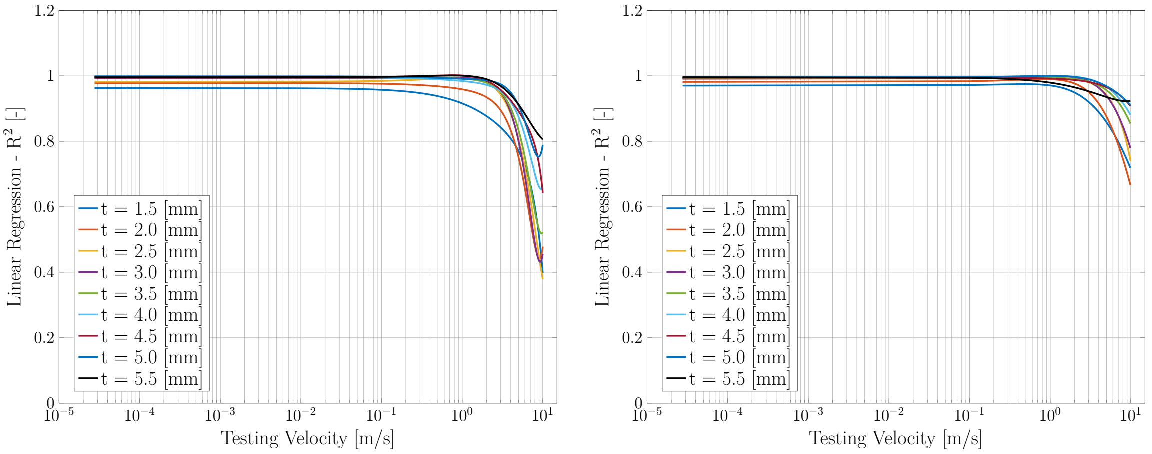

(a) **(b)**

Figure 4.11: Fitting curves for tests performed with the support span of (a) 80 mm and (b) 60 mm.

The reason of the different behaviour in the fitting curve for the 5.5 mm tick specimen is the fact that already at 5 m/s the R^2 value computed was 0.93, which was lower than the ones obtained for specimens with a thickness of 4, 4.5 and 5 mm. On the other hand, the R^2 value at 10 m/s is the highest exactly for the 5.5 mm thick specimen. The pictures taken during testing were analysed to determine the cause, however the failure mechanism observed was failure initiated by compressive fibre kinking as for the other tests. It was thought that this drop was due to shear effect in the specimen or damage on the top surface due to the initial impact with the fixture impactor. For this reason further investigations would be required to properly assess the different trend shown by this specific test setup.

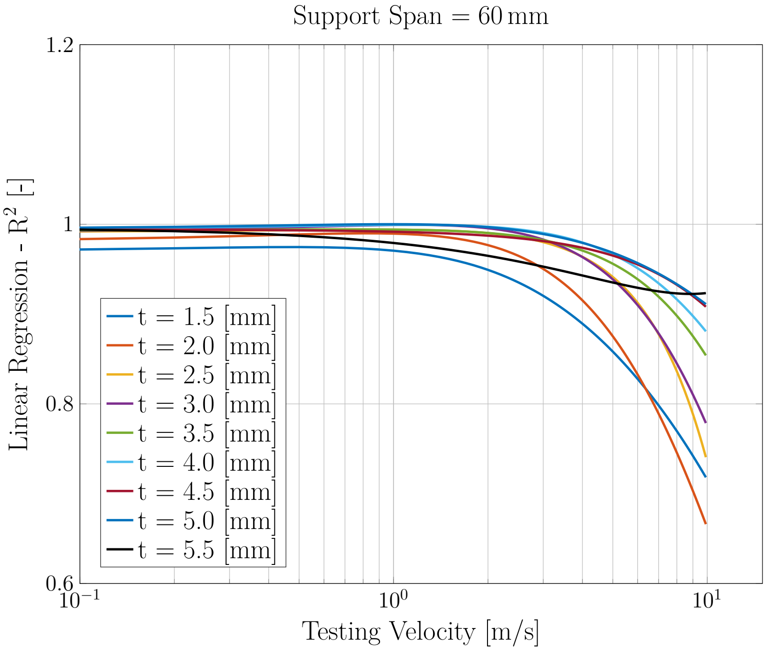

Figure 4.12: Fitting curves for tests performed with the support span of 60 mm.

From the fitted curves shown in Figure 4.11, it is possible to obtain the testing velocity corresponding to a specific value of R^2. The higher is the value of R^2, and the less affected by the specimen vibrations and the initial detachment from the impactor are the test results. Given the test results, it is suggested to choose a value between 0.95 and 0.97. The choice depends on the level of reliability which the user wants to achieve. An example is here provided, where a minimum R^2 value of 0.95 was selected. The first step is to obtain the testing velocity corresponding to $R^2 = 0.95$ from the fitting curves showed in Figure 4.11. This process is shown in Figure 4.13, which is specific for the fitting curves obtained from the 3 mm thick specimen tested with both support spans. Given the R^2 value required the corresponding testing velocity was obtained from Matlab®. The closest value to $R^2 = 0.95$ is searched in the fitting curve dataset and the corresponding testing velocity is obtained.

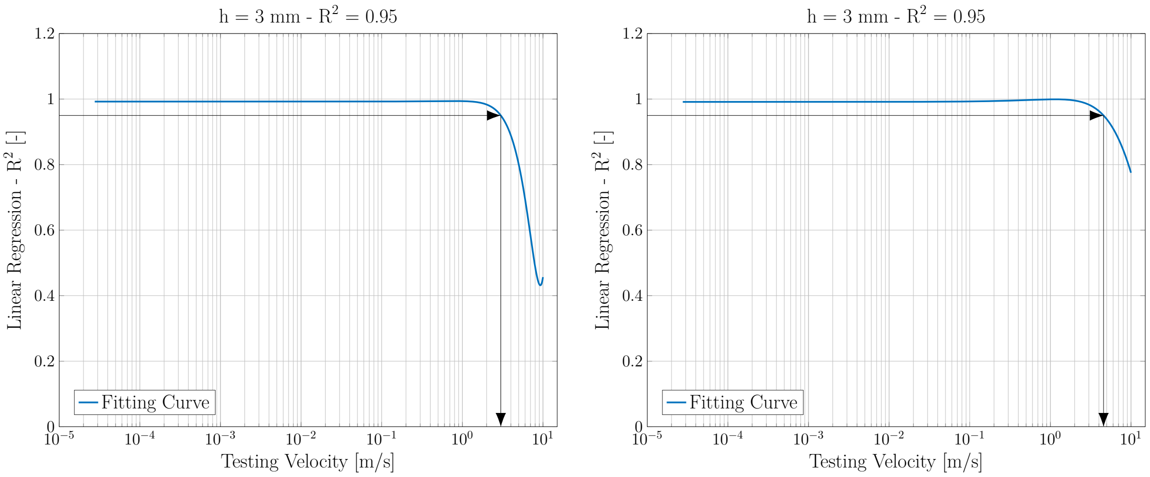

(a) **(b)**

Figure 4.13: Estimation of the maximum testing velocity at a value of $R^2 = 0.95$, for 3 mm thick specimens with the support span of (a) 80 mm and (b) 60 mm.

For a defined value of R^2, the process described above was performed for every combination of specimen thickness and support span tested. In total eighteen data points are obtained, nine relative to the tests performed with the 80 mm support span and other nine relative to the tests performed with the 60 mm support span. As for each test setup it was possible to compute a value of global stiffness (as shown in Table 4.1), the obtained velocities were plotted in correspondence of the specimen global stiffness, as shown in Figure 4.14. The data points were fitted using the polynomial and exponential function described in Equation 4.8. Polynomials up to the 3$^{\text{rd}}$ order were considered, as polynomials of higher order did not gave a good fit of the available data. This is already displayed by the 3$^{\text{rd}}$ polynomial in Figure 4.14a.

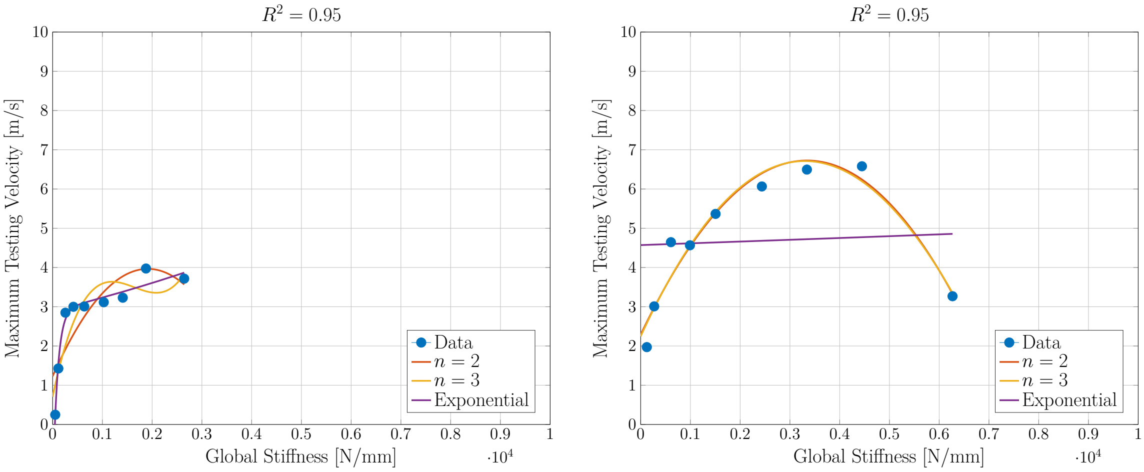

(a) **(b)**

Figure 4.14: Fitting curves for prediction of the maximum allowed testing velocity depending on the specimen global stiffness for the support span of (a) 80 mm and (b) 60 mm at $R^2 = 0.95$.

For both support spans the maximum testing velocity increases as the global stiffness increases. However, the 60 mm support span results show a decrease in testing velocity for the specimen with the highest stiffness. This behaviour is shown because, as previously explained, at 5 m/s the value of R^2 was already 0.93.
From Figure 4.14b it looks like that there is a global stiffness value (a cutoff value) after which the estimated testing velocity decreases. This is not shown in the test performed with the 80 mm support span, probably because the specimens tested did not reach the stiffness value after which the decrease in estimated testing velocity would be observed. Further investigation are required to determine such a global stiffness threshold and fully characterise the curves behaviour.
If the data point relative to the highest stiffness in Figure 4.14b is omitted from the interpolation, the exponential fitting for the data relative to the support span of 60 mm resembles the graph displayed in Figure 4.14a. This is shown in Figure 4.15.

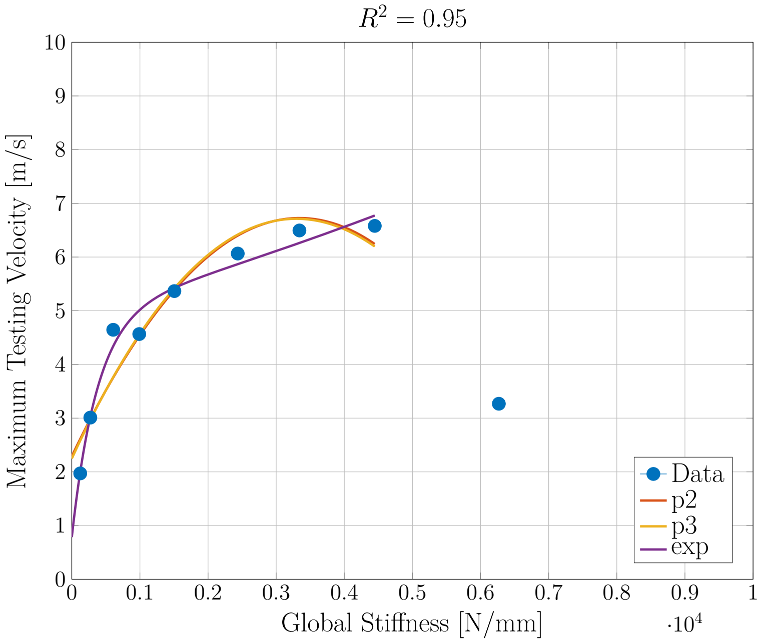

Figure 4.15: Fitting curves for prediction of the maximum allowed testing velocity depending on the specimen global stiffness for the support span of 60 mm at $R^2 = 0.95$.

The combined results are shown in Figure 4.16. The figure displays the curves used to estimate the maximum testing velocity referred to the R^2 value of 0.95 (Figure 4.16a) and 0.97 (Figure 4.16b). The exponential law was used to fit the data obtained with both support spans. For low values of global stiffness the two curves nearly overlap. After the global stiffness value of approximately 300 N/mm, the two curves depart from one another. The reduction in support span allowed obtaining higher testing velocities among specimens with comparable global stiffness. As expected, the increase in R^2 produces a reduction in maximum testing velocity. This is the result of the more strict regression parameter.
A cutoff global stiffness value is increasing with the reduction of the support span. With the data available, the maximum testing velocity looks linearly increasing with the cutoff global

stiffness. To determine whether this relationship is linear or non-linear tests with a third different support span should be performed, for example with a support span of 70 or 40 mm.

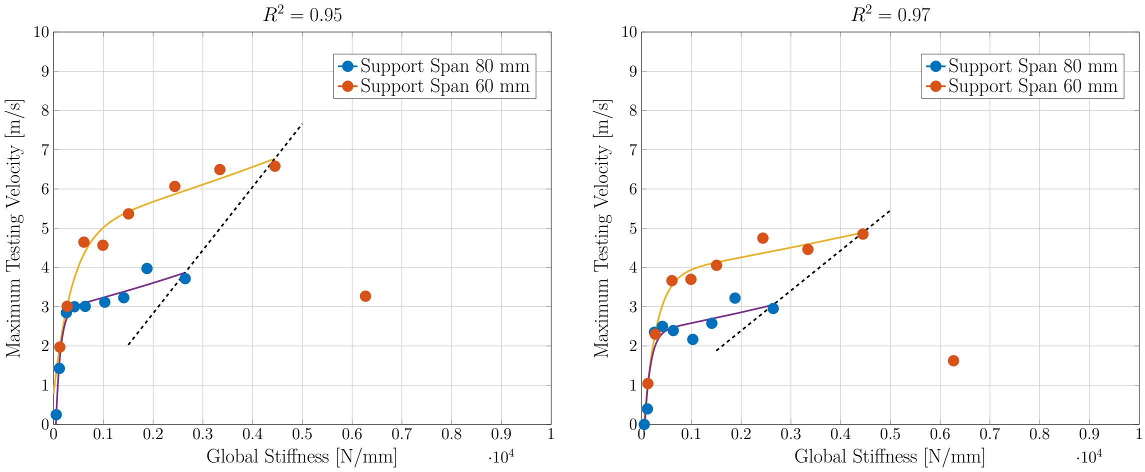

(a) **(b)**

Figure 4.16: Estimated maximum testing velocity for (a) $R^2 = 0.95$ and (b) $R^2 = 0.97$.

4.5 Matlab Graphical User Interface

The procedure described in the previous sections was implemented in a Matlab® code. A graphical user interface (GUI) was implemented so that the user could easily interact with the code. The GUI is shown in Figure 4.17 below.

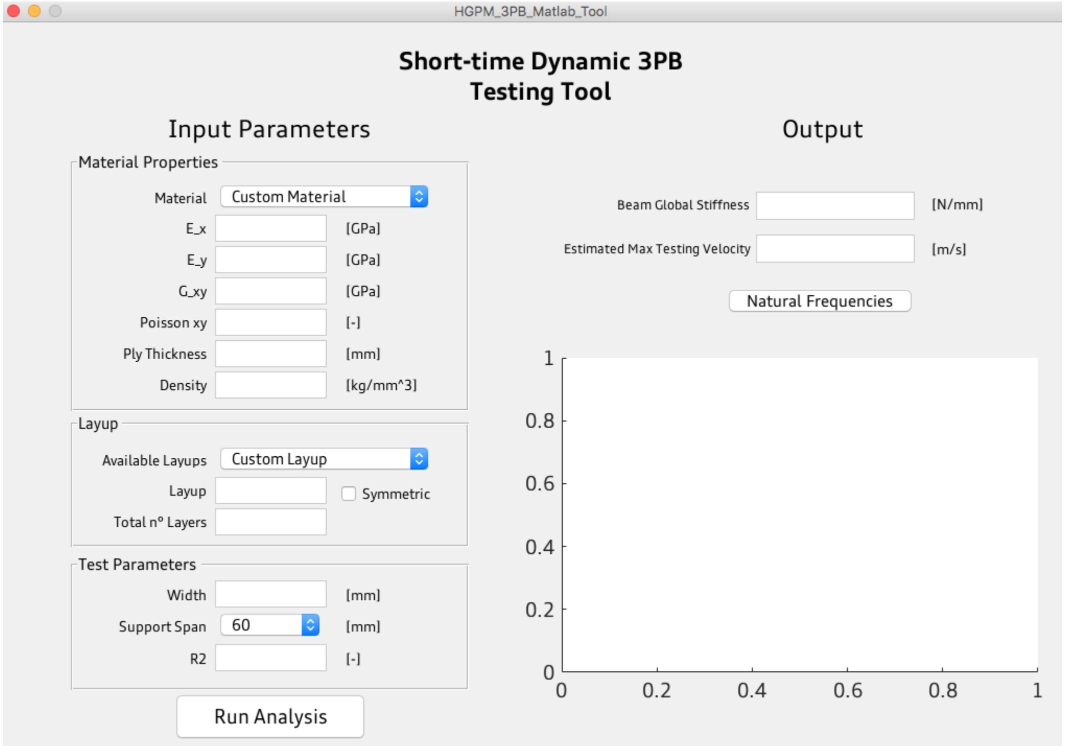

Material: Custom Material

Available Layups: Custom Layup

Support Span: 60 [mm]

HGPM_3PB_Matlab_Tool
Short-time Dynamic 3PB Testing Tool
Input Parameters
Output
Material Properties
E_x [GPa]
E_y [GPa]
G_xy [GPa]
Poisson xy [-]
Ply Thickness [mm]
Density [kg/mm^3]
Layup
Layup
☐ Symmetric
Total n° Layers
Test Parameters
Width [mm]
R2 [-]
Run Analysis
Beam Global Stiffness [N/mm]
Estimated Max Testing Velocity [m/s]
Natural Frequencies
0
0.2
0.4
0.6
0.8
1

Figure 4.17: Matlab graphical user interface.

The GUI requires the user to give as an input the material properties, the specimen layup and some testing parameters. As several materials are used in Audi, of which the material properties are already known, a material database has been created. The material can be chosen using a drop down menu and the material properties are automatically filled by the code and shown in the corresponding box. If the material is not in the database, a custom material can be selected. This option allows the user to input the material properties directly in the corresponding box.

In the section "Layup" the specimen layup is defined. Some types of layups are already built-in in the code. They are the UD, the cross-ply $[0/90]_{nS}$ and $[45/-45]_{nS}$, and the quasi-isotropic $[45/-45/0/90]_{nS}$ layup. In case of cross-ply and quasi-isotropic layups, the resulting layup is always symmetric. If the layup to be tested does not fit in such categories, the "Custom" option can be selected. This option allows to enter non-symmetric layups with the plies oriented at any angle.

Finally, test parameters such as the specimen width, the support span, and the minimum R^2 required are chosen. Regarding the support span, it is possible to choose between 60 or 80 mm. This is done so that the corresponding fitting curve as shown in Figure 4.16 can be

used by the code to estimate the maximum testing velocity.
Each parameter given as an input in the GUI is checked to ensure that it fits in the allowed range. In case one of the input parameter does not fit in the allowed range, an error message is displayed on the screen. The message also tells which of the input parameter must be changed in order to run the code.

An example of the output of the GUI is shown in Figure 4.18. In the case shown the material selected was the same as the one used for the tests performed in this study. The layup consisted of 25 layers of UD, the specimen width selected was 15 mm with a support span of 60 mm. The minimum R^2 was chosen was 0.95. The GUI gives as the beam global stiffness, computed using Equation 4.6, and the estimated maximum testing velocity. Also the graph maximum testing velocity-beam global stiffness is provided, which shows the position of the new test setup through a vertical line.

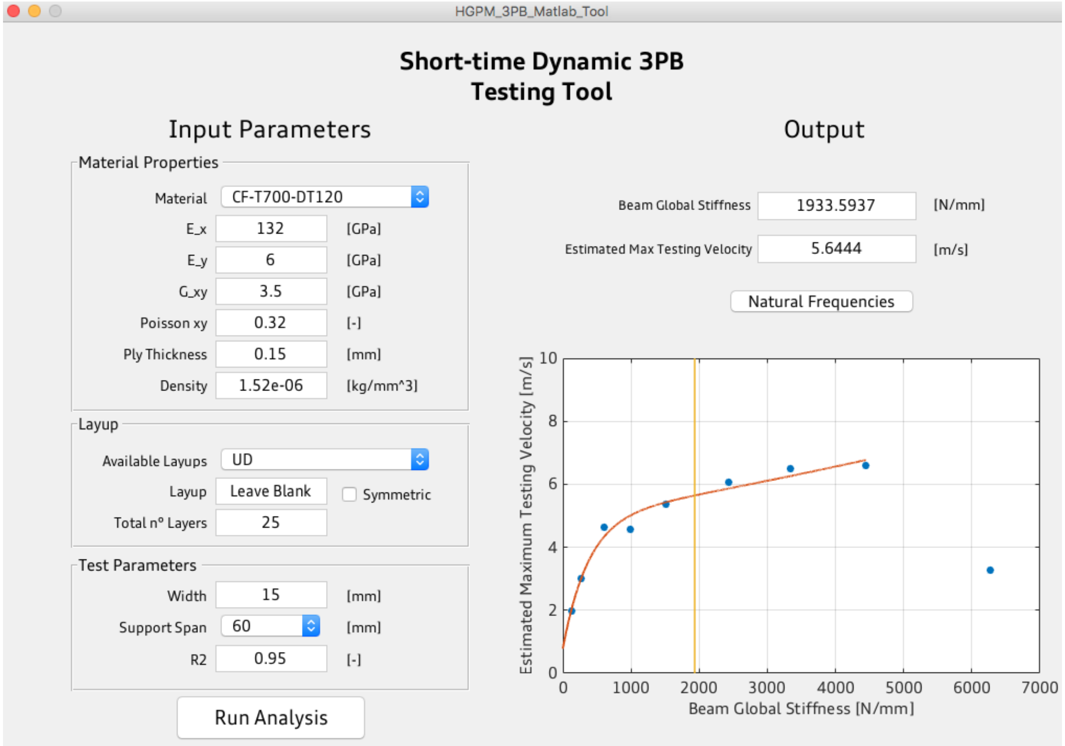
HGPM_3PB_Matlab_Tool

Short-time Dynamic 3PB Testing Tool

Input Parameters

Material Properties
Material: CF-T700-DT120
E_x: 132 [GPa]
E_y: 6 [GPa]
G_xy: 3.5 [GPa]
Poisson xy: 0.32 [-]
Ply Thickness: 0.15 [mm]
Density: 1.52e-06 [kg/mm^3]

Layup
Available Layups: UD
Layup: Leave Blank ☐ Symmetric
Total n° Layers: 25

Test Parameters
Width: 15 [mm]
Support Span: 60 [mm]
R2: 0.95 [-]

Output
Beam Global Stiffness: 1933.5937 [N/mm]
Estimated Max Testing Velocity: 5.6444 [m/s]

Run Analysis
Natural Frequencies
Estimated Maximum Testing Velocity [m/s]
0
2
4
6
8
10
0
1000
2000
3000
4000
5000
6000
7000
Beam Global Stiffness [N/mm]

Figure 4.18: Output of the Matlab GUI.

4.6 Conclusions

In this chapter the method used to estimate the maximum testing speed which leads to low specimen vibrations and low detachment between the specimen and the impactor has been presented.

A linear regression was used to interpolate the force-displacement curves and the goodness of the fitting line was measured through the coefficient of determination R^2. The coefficient R^2 increases with the increase of the specimen thickness. However, a higher improvement is obtained by reducing the support span, as shown in Figure 4.8. For each setup tested the beam global stiffness was computed according to Section 4.2.1, this allowed reducing the influence of several parameters in the test setup to a single parameter. The curves for estimating the maximum testing velocity are shown in Figure 4.11. Two curves are presented, because the support span has a high influence on the test results. This leads to considering separately the results obtained with the two support spans and not to combine them together. The general trend shown is an increase in the maximum testing velocity with increasing beam global stiffness. The only exception is for tests performed with specimens 5.5 mm thick with the support span of 60 mm. The low maximum testing velocity is due to the fact that a low R^2 is already obtained at the testing velocity of 5 m/s.

The analysis presented allowed to implement a Matlab® tool to estimate the maximum testing velocity for a defined test setup and a minimum value of R^2 chosen by the user. This tool aims to estimate the maximum testing velocity that provides reliable test results, avoiding to test specimens at higher testing velocities which could provide unreliable data that cannot be used for further analysis.

Chapter 5

Finite Element Simulation

This chapter discusses the procedure used to calibrate the strain rate dependent compressive properties of the material card used and the finite element model used to simulate the 3PB dynamic test. Section 5.1 introduces the material model and the element type most used by Audi to simulate composite components, Section 5.2 describes the strain rate dependent model for composite material implemented in PAM-CRASH. Section 5.2.1 presents a comparison between the two ply types that could have been used in the simulation model. Section 5.3 presents the strain strain rate dependent compressive properties imported in the simulation material card, while Section 5.4 shows the procedure used to calibrate the material card. In Section 5.5 the 3PB simulation model is described and the simulation results are presented and compared with the test results. Finally, conclusions based on the content of this chapter are drawn in Section 5.6.

5.1 Introduction

Shell elements are used by Audi simulation department to model components made of fibre reinforced plastics. This element type is well suited to model FRP components in the automotive industry. As it is possible to see in Figure 5.1, in the Audi R8 e-tron, CFRP is mainly employed for body components. Such components are smooth surfaces of a defined thickness, making them well suited to be modelled using shell elements. Since they are two-dimensional elements, shells allow defining a surface by its mid-plane and its thickness. They are also less computationally expensive compared to solid elements, as a smaller number of elements is needed in the simulation model. Thus, reliable simulation results can be obtained while keeping a low computational effort.

The software PAM-CRASH provides several material models which can be used to simulate composites. In the Audi specific case the Material Model 131 in combination with the Ply Model Type 1 is used. The material model 131 is a multi-layered and multi-material shell that allows defining the shell layup, the element elimination parameters, and the output of specific variables of interest. An element is eliminated when a certain ratio of plies has failed. The ratio is defined by the user and a value between 70 and 75 % is normally used. The material properties of a single ply which constitutes the composite are given in the corresponding material ply card.

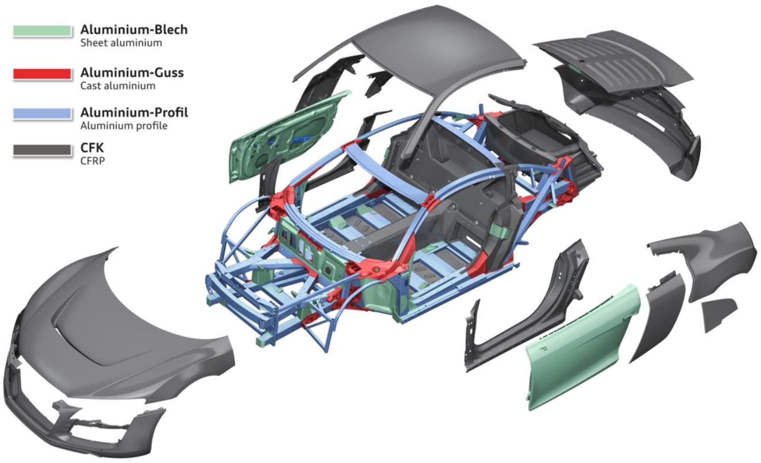

Figure 5.1: AUDI R8 e-tron body [39].

The simulation department uses square shell elements with a length of 5 mm in full vehicle crash simulations to keep the models not too computationally expensive. This fact results in restrictions in the material card validation model. The 3-point bending simulation model had therefore the following limitations:

- the use of shell elements to model the specimen
- the elements had to be squared
- the element length was restricted to 5 mm

These limitations were imposed to ensure that the material card functions correctly in a full vehicle simulation and were taken into account during the implementation of the simulation model.

5.2 Strain Rate Dependent Model in PAM-CRASH

The implementation of strain rate sensitivity in PAM-CRASH Ply Models follows the modelling described by Rozycki [50] and it is the model implemented in all ply types, with minor changes between each ply type. Studies on composites have shown that there is a strain rate threshold above which some material properties are strongly influenced by the strain rate. This allows identifying a reference curve from which the strain rate behaviour can be extrapolated. Typically, the quasi-static stress-strain curve is taken as a reference. Additionally, the increase in Young's modulus, fracture strain, and yield stress (if existing) can be described by laws of evolution.

Through the use of the concept of viscous stresses and the use of the Kelvin-Voigt material model Rozycki was able to determine the influence of the strain rate on the composites stiffness matrix. The stiffness matrix obtained is the following:

$$\begin{Bmatrix} \sigma_{11} \\ \sigma_{22} \\ \sigma_{12} \\ \sigma_{13} \\ \sigma_{23} \end{Bmatrix} = \begin{bmatrix} C_{11} & \nu_{21}^{0} C_{11} & 0 & 0 & 0 \\ \nu_{21}^{0} C_{11} & C_{22}\left(1-d_{22}\right) & 0 & 0 & 0 \\ 0 & 0 & C_{12}\left(1-d_{12}\right) & 0 & 0 \\ 0 & 0 & 0 & G_{13}^{0} & 0 \\ 0 & 0 & 0 & 0 & G_{23}^{0} \end{bmatrix} \begin{Bmatrix} \varepsilon_{11}^{e} \\ \varepsilon_{22}^{e} \\ 2\varepsilon_{12}^{e} \\ 2\varepsilon_{13}^{e} \\ 2\varepsilon_{23}^{e} \end{Bmatrix} \tag{5.1}$$

where ε_{ij}^{e} and σ_{ij} are respectively the elastic strains and the stresses in the laminate directions, C_{ij} is the strain rate dependent material modulus in the ij direction, and G_{ij} is the shear modulus.

The terms C_{ij} depend on the strain rate through the use of viscosity functions $F_{ij}\left(\dot{\varepsilon}\right)$. Such functions affect the elastic moduli through the law $C_{ij} = C_{ij}^{0}\left(1 + F_{ij}\left(\dot{\varepsilon}\right)\right)$. The term C_{ij}^{0} is the corresponding elastic modulus, for example $C_{ij}^{0} = E_{11}$.

Another function F_{11}^{R} is introduced to allow the longitudinal fibre fracture strain to be strain rate dependent. This function influences both the longitudinal tensile and compressive fracture strain in the same form as the elastic moduli are influenced by the strain rate.

To define the viscosity functions F_{ij} fitting laws are used to interpolate the data coming from strain rate dependent coupon tests. The available fitting laws are

$$\begin{aligned} \text{Power law:} \quad F_{ij}\left(\dot{\varepsilon}\right) &= D_{ij} \left(\frac{\dot{\varepsilon}}{\dot{\varepsilon}_{ij}^{ref}}\right)^{n_{ij}} \\ \text{Linear law:} \quad F_{ij}\left(\dot{\varepsilon}\right) &= D_{ij} \left(\frac{\dot{\varepsilon}}{\dot{\varepsilon}_{ij}^{ref}}\right) + n_{ij} \\ \text{Neperian logarithmic law:} \quad F_{ij}\left(\dot{\varepsilon}\right) &= D_{ij} \ln\left(\frac{\dot{\varepsilon}}{\dot{\varepsilon}_{ij}^{ref}}\right) + \ln\left(n_{ij}\right) \end{aligned} \tag{5.2}$$

where $\dot{\varepsilon}$ is the strain rate induced by the loading conditions and $\dot{\varepsilon}_{ij}^{ref}$ is the strain rate threshold of the reference curve chosen for the extrapolation of the rate dependent behaviour of the mechanical properties. The two constants D_{ij} and n_{ij} are the parameters that characterise the fitting law. The least square method between the fitting law and the test results can be used to obtain the optimal parameters.

5.2.1 Choice of the Ply Model Type

Among the ply types available in PAM-CRASH only Ply Model Type 1, 2 and 7 have the possibility to take into account the strain rate dependency of the material mechanical properties. Ply Model Type 2 is used to model isotropic elastic-plastic damaging plies, therefore it was not suitable to model the UD composite used in this study. Ply Model Type 1 is used to model UD plies. Ply Model Type 7 is implemented for fabric composites, but material properties can be input so that it behaves as a quasi-UD ply. As the strain rate dependent model implemented in Ply Model Type 1 showed some limitations, also Ply Model Type 7 was considered as a possible candidate to implement the material card that would be used for the simulation models. Advantages and disadvantages of the two ply types are discussed hereafter.

In Ply Model Type 1 there is no separation between the strain rate behaviour in the longitudinal direction for tensile and compressive behaviour. The same viscosity function is applied for tensile properties as well as compressive properties. Therefore, the evolution in the fibre direction of the Young's modulus and of the longitudinal fracture strain is assumed identical for both tensile and compressive behaviour. Furthermore, the same fitting law type from Equation 5.2 has to be chosen to fit the two groups of data. It has been shown in Section 2.1.1 that, for UD carbon/epoxy systems, there is no strain rate effect on the tensile modulus and fracture strain in the longitudinal direction. However, the compressive fracture strain is affected by the strain rate, as shown in Section 2.1.2.
Ply Model Type 7 allows defining separately the fitting law for the tensile and the compressive Young's modulus. On the other hand, there is no possibility to make the fracture strain in fibre longitudinal direction strain rate dependent. In Table 5.1 the advantages and disadvantages found concerning each ply type are presented.

Ply model type 7 was missing one of the key features to model the strain rate dependent behaviour of UD composites: the possibility of modelling the strain rate effect on the longitudinal fibre fracture strain. For this reason it was discarded and Ply Model Type 1 was chosen to create the material card used in the simulation models.
From test results (see Section 5.3), also the longitudinal compressive modulus was not affected by the strain rate. So the problem of having the same strain rate dependent behaviour for tensile and compressive longitudinal modulus was solved.
The strain rate compressive tests performed in a previous study [14] showed an increase in fracture strength and strain with increasing strain rate. To ensure that no strain rate effect would be modelled in the longitudinal tensile direction, the Yamada-Sun [51] failure criterion in combination with the Puck [52] failure criterion was used. The Yamada-Sun failure criterion implemented in PAM-CRASH ensures that the fibre failure occurs at a specific strain value. In this case, the tensile fracture strain obtained from tensile quasi-static tests was used as the tensile failure strain for the Yamada-Sun criterion.

Table 5.1: Advantages and disadvantages for Ply Model Type 1 and 7.

	Ply Model Type 1	Ply Model Type 7
UD	✓	can be modified accordingly
Non crimp fabric	✓	✓
Woven fabric	x	✓
Strain rate dependency		
Tensile modulus	✓	✓
Compressive modulus	✓	✓
Shear modulus	✓	✓
Longitudinal fibres fracture strain	✓	x
Yield stress	✓	✓
Separate fitting law for tensile and compressive modulus	x	✓
Same fitting law for modulus and fracture strain	✓	non applicable

The Yamada-Sun criterion defines failure when

$$\left(\frac{\sigma_{11}}{X}\right)^2 + \left(\frac{\tau_{12}}{S}\right)^2 = 1 \qquad \text{where} \qquad \begin{array}{lll} X = X^t & \text{if} & \sigma_{11} > 0 \\ X = X^c & \text{if} & \sigma_{11} < 0 \end{array} \tag{5.3}$$

where σ_{11} is the stress in a ply in the longitudinal fibre direction, τ_{12} is the in-plane shear stress, S is the shear strength. The term X represents the strength of the ply in the fibre direction, the tensile or compressive strength is used depending on the value of the stress in the longitudinal fibre direction.

The Puck [52] failure criterion is a more complex failure criterion. It splits the ply failure into fibre failure and inter fibre failure (matrix dominated failure). The inter fibre failure depends on the inclination of the failure plane. A simplification of the failure criterion can be obtained when in-plane loads are considered and the inter fibre failure plane is assumed parallel to the longitudinal fibre direction. The equations for the failure criterion are the following:

$$\begin{array}{llll} \text{Fibre:} & \left(\frac{\sigma_{11}}{X}\right)^2 = 1 & \text{where} & \begin{array}{lll} X = X^t & \text{if} & \sigma_{11} > 0 \\ X = X^c & \text{if} & \sigma_{11} < 0 \end{array} \\ \text{Inter Fibres:} & \left(\frac{\sigma_{22}}{Y}\right)^2 + \left(\frac{\tau_{12}}{S}\right)^2 = 1 & \text{where} & \begin{array}{lll} Y = Y^t & \text{if} & \sigma_{22} > 0 \\ Y = Y^c & \text{if} & \sigma_{22} < 0 \end{array} \end{array} \tag{5.4}$$

where σ_{22} is the stress in a ply in the transverse to fibre direction and Y represents the strength of the ply in the transverse to fibre direction, the tensile or compressive strength is used depending on the value of σ_{22}.

5.3 Strain Rate Dependent Compressive Properties

In the previous chapters the work presented dealt only with strain rate dependent 3PB tests. None of the results could be used as input parameters for the material card, but they were used for the validation of the strain rate dependent 3PB simulation model. Additional strain rate dependent compression tests were performed to be used as input data for the material card.

The strain rate dependent compressive properties for the material used in this research were obtained in a previous study performed by Schmack et al. [14]. The study investigated the effect of the load introduction method at various strain rates on the compressive properties of the UD carbon/epoxy T700-DT120. The longitudinal compressive tests were performed using a servo-hydraulic testing machine and strain rates of approximately $100\,\mathrm{s}^{-1}$ were reached. One fixture allowed introducing the load in the specimen through a combination of shear and uniaxial load (fixture A) following the NU-method, the other fixture allowed load introduction only through uniaxial load (fixture B). Each fixture was designed for a specific specimen geometry. The difference between the two geometries was in terms of length, width and thickness. The geometry for the specimens tested in fixture A was $90 \times 20 \times 3$ mm (specimen A), while the one tested in fixture B was $75 \times 15 \times 2$ mm (specimen B). As glass tabs were glued on the specimens, the two geometries differed also in terms of gauge length. Specimen A had a gauge length of 20 mm, whereas the gauge length for specimen B was 12 mm. The strain measurements were obtained using DIC for specimen A and using strain gauges bonded on the gauge area for specimen B.

The test results are shown in Figure 5.2, where the x-axis is in logarithmic scale. The compressive strength increased with increasing strain rate. The test results obtained by testing specimen A in fixture A showed a logarithmic increase of the compressive strength. However, at the strain rate of $3.5\,\mathrm{s}^{-1}$, a drop was observed in the test results. The drop was observed at the highest testing velocity obtainable with the testing machine. It was not possible to investigate whether at a higher strain rate the trend of the compressive strength would still continue to be logarithmic. For this reason specimens with geometry B were tested in fixture A at comparable strain rates. The results showed no drop in the compressive strength, and an increasing logarithmic trend was observed. The different behaviour shown by specimen B was probably due to the smaller gauge length, which affected the specimen global and local buckling.

The results obtained by testing specimen B in fixture B are represented by the red data in the plot. At low and high strain rates the data were in good correlation with the results obtained from the tests in fixture A. At the intermediate strain rates the compressive strength is lower compared to the one observed in fixture A. This is because the specimen buckling is more critical in fixture B, as there are no clamping jaws that fix the specimen from the sides.

The longitudinal compressive initial modulus showed a high variance, thus it was inferred that there was no significant influence on it due to strain rates. For this reason there was no need to determine a strain rate dependent fitting law for the compressive modulus in

PAM-CRASH.

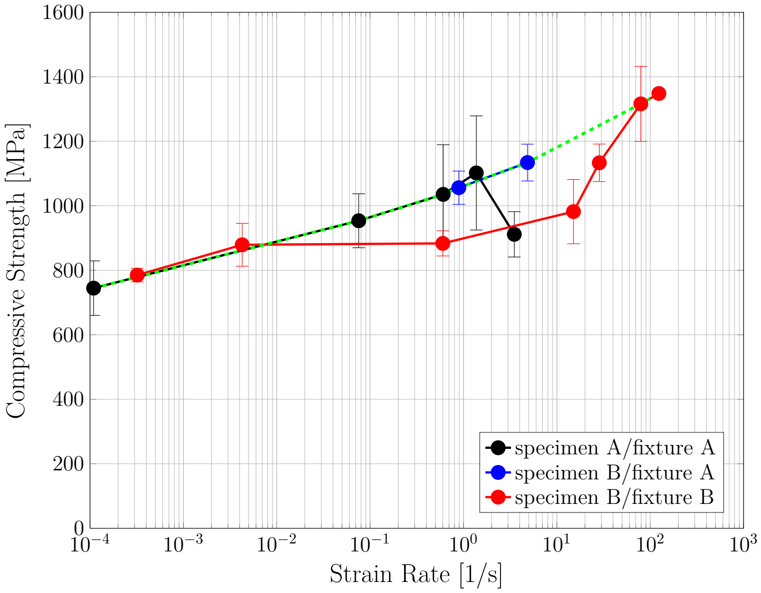

Figure 5.2: Compression test results.

5.3.1 Compressive Strain

In PAM-CRASH's Ply Model Type 1 the strain rate dependent compressive behaviour is described by fitting laws that represent the change in the compressive modulus and in the compressive fracture strain according to the strain rate. The test results showed no dependency of the compressive modulus on the strain rate. So, it was required to determine the fitting parameters for the strain rate effect on the compressive fracture strain.

The data from the strain rate dependent compressive test results which showed a linear increasing trend with the logarithm of the strain rate were chosen as the reference data used to determine the fitting law most suitable to implement the strain rate dependency of the fracture strain in the PAM-CRASH material card. Therefore, data from the three test setups previously described were chosen to be interpolated with the fitting laws from Equation 5.2. In particular, the data concerning the low strain rates were selected from the tests performed using specimen A in fixture A, the data for the intermediate strain rates were selected from the tests performed using specimen B in fixture A, and the data for the highest strain rates were selected from the tests performed using specimen B in fixture B. The test results to be fitted are shown in Figure 5.3 and summarised in Table 5.2, which also reports the fracture strain. Due to the linear stress-strain compressive behaviour of the UD carbon/epoxy, also the fracture strain increases with increasing strain rate.

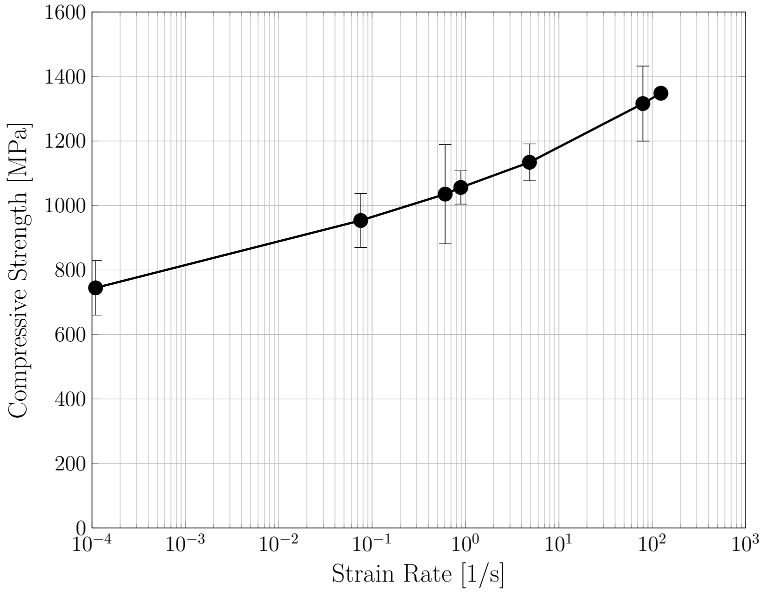

Figure 5.3: Compression test results used to determine the strain rate fitting law for the PAM-CRASH material card.

Table 5.2: Strain rate compression test results.

Strain Rate [1/s]	Fracture Strain [%]	Compressive Strength [MPa]
1.09×10^{-4}	0.87	745
0.076	1.14	954
0.6	1.24	1035
0.9	1.20	1056
4.9	1.24	1134
79	1.38	1316
124	1.45	1348

The first step required in order to determine the fitting parameters D_{ij} and n_{ij} was to create the table for the parameter analysis. Such table is described by the PAM-CRASH user manual and it is shown in Table 5.3. It was required to choose a reference strain rate $\dot{\varepsilon}_{ref}$ and a reference fracture strain ε_{ref}^{fc}. As suggested by the user manual the values obtained from the quasi-static compression tests were chosen as reference values

$$\begin{aligned} \dot{\varepsilon}_{11}^{ref} &= \dot{\varepsilon}_{qs} \\ \varepsilon_{11}^{ref} &= \varepsilon_{qs}^{fc} \end{aligned} \tag{5.5}$$

The normalised strain rate and the normalised fracture strain were then computed for all the tested velocities.
Given the reference strain rate, the reference fracture strain, and the fitting parameters D_{ij} and n_{ij} the software is able to compute the fracture strain at any strain rate using the equation

$$\varepsilon_{11}^{fc}\left(\dot{\varepsilon}\right) = \varepsilon_{qs}^{fc}\left(1 + F_{11}^{R}\left(\dot{\varepsilon}\right)\right) \tag{5.6}$$

where $F_{11}^{R}\left(\dot{\varepsilon}\right)$ is the fitting law from Equation 5.2 chosen to interpolate the tests data.

Table 5.3: Strain rate parameter analysis for UD compression tests.

PAM-CRASH Definition			Compression Tests		
Strain Rate [1/s]	Normalised Strain Rate [-]	Normalised Fracture Strain [-]	Strain Rate [1/s]	Normalised Strain Rate [-]	Normalised Fracture Strain [-]
$\dot{\varepsilon}_{qs} = \dot{\varepsilon}_{11}^{ref}$	$\frac{\dot{\varepsilon}_{qs}}{\dot{\varepsilon}_{11}^{ref}}$	$\frac{\varepsilon_{qs}}{\varepsilon_{11}^{ref}}$-1	0.0001	1	0
$\dot{\varepsilon}_{2^{nd}\ velocity}$	$\frac{\dot{\varepsilon}_{2^{nd}\ velocity}}{\dot{\varepsilon}_{11}^{ref}}$	$\frac{\varepsilon_{2^{nd}\ velocity}}{\varepsilon_{11}^{ref}}$-1	0.07	700	0.32
$\dot{\varepsilon}_{3^{rd}\ velocity}$	$\frac{\dot{\varepsilon}_{3^{rd}\ velocity}}{\dot{\varepsilon}_{11}^{ref}}$	$\frac{\varepsilon_{3^{rd}\ velocity}}{\varepsilon_{11}^{ref}}$-1	0.6	6E3	0.43
etc.	etc.	etc.	etc.	etc.	etc.

Once the table for the parameter analysis was obtained, the normalised fracture strain was plotted versus the normalised strain rate. Such plot was used to determine the parameters D_{ij} and n_{ij} for the fitting laws. All three fitting laws (power, linear and neperian logarithmic) were considered when fitting the data. In order to obtain the best fit the least squares method was used to determine the optimal coefficients. For the fracture strain ε_{11}^{fc}, the coefficients of the fitting laws are referred as D_{11}^{R} and n_{11}^{R}. Figure 5.4 shows the fitting laws results obtained through the method of the least squares and in Table 5.4 the corresponding coefficients are presented.

The power law agrees quite well with the test results at the intermediate and highest strain rate values, but the strain at the quasi static velocity is overestimated. Since the power law does not have a constant term it is not possible to obtain a normalised fracture strain equal to zero at the quasi-static strain rate. In order to have that the term D_{11}^{R} should be equal to zero, but this would give $F_{11}^{R}\left(\dot{\varepsilon}\right) = 0$ for any value of strain rate. The linear law is only able to properly fit the normalised fracture strain at the quasi-static and at the highest strain rate. For strain rates in between these two values the linear law underestimates the testing results. As already seen in Figure 5.3, the test results showed a logarithmic behaviour. The neperian logarithmic law was the one that gave the best fitting result. It is able to correctly estimate the normalised fracture strain at the quasi-static strain rate and a good fit is obtained for the test results at higher strain rate. This fitting law was chosen as the one to be used in the PAM-CRASH material card. The corresponding coefficient used were $D_{11}^R = 0.0476$ and $n_{11}^R = 1$.

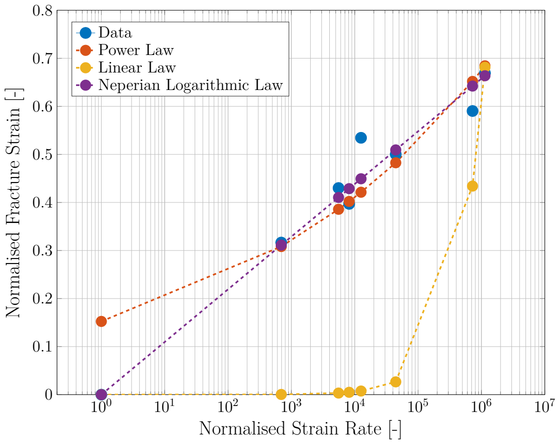

Figure 5.4: Interpolation of the compressive fracture strain.

Table 5.4: Coefficients for the fitting laws.

Fitting Law	D_{11}^R	n_{11}^R
Power	0.1524	0.1077
Linear	6×10^{-7}	0
Neperian Logarithmic	0.0476	1

To asses the prediction of the fracture strain Equation 5.6 was used to predict the fracture strain. The term $F_{11}^R(\dot{\varepsilon})$ was substituted by the selected fitting law

$$\varepsilon^{fc}(\dot{\varepsilon}) = \varepsilon_{qs}^{fc}\left(1 + F_{11}^R(\dot{\varepsilon})\right) = \varepsilon_{qs}^{fc}\left(1 + D_{11}^R \ln\left(\frac{\dot{\varepsilon}}{\dot{\varepsilon}_{qs}}\right) + \ln\left(n_{11}^R\right)\right) \tag{5.7}$$

The results of Equation 5.7 are shown in Figure 5.5, where Figure 5.5a has a logarithmic x-axis and Figure 5.5b has a normal scale x-axis. The prediction using the neperian logarithmic law shows a good correlation with the test results.

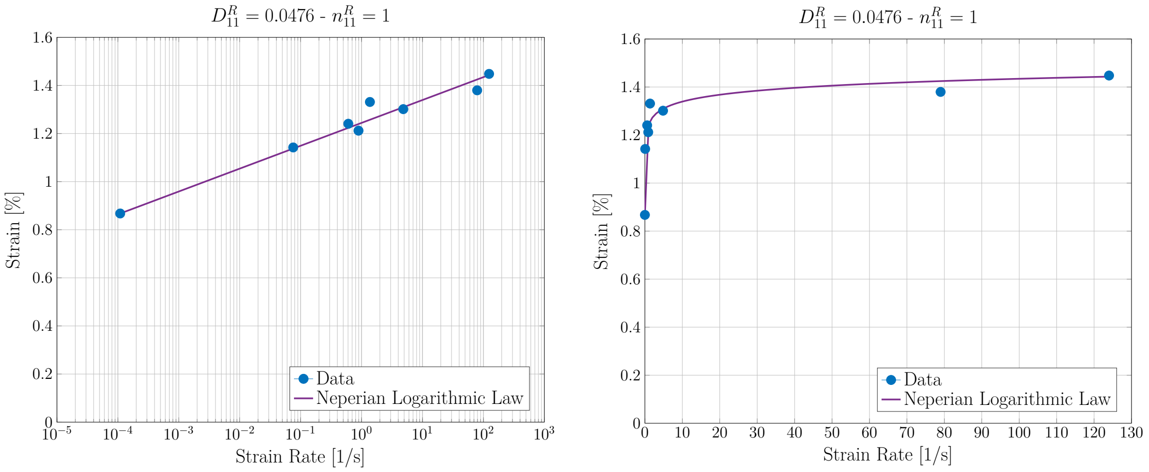

(a) **(b)**

Figure 5.5: Neperian logarithmic law used to fit the test results in (a) logarithmic and (b) normal scale x-axis.

5.4 Calibration of the Strain Rate Properties

The single element model was used to calibrate the compressive strain rate dependent properties. This method is widely used and has been described in Section 2.2.2. In this thesis the single element model consisted of a square shell element of size 10×10 mm, as shown in Figure 5.6. This are the dimensions, defined by the simulation department, for all single element models used to calibrate material cards. It was claimed that there was no influence of the element size on the calibration procedure, therefore the single element model dimensions were not changed. On the other hand, the restriction of 5 mm element size for the 3PB validation model was still enforced.
The element layup used was $[0]_4$. Each ply had a thickness of 0.25 mm, therefore the thickness of the single element was 1 mm. Particular attention was given to the element boundary conditions, so that the correct compression behaviour could be simulated. The boundary conditions were applied as displacement boundary conditions to the four nodes of the element and they are summarised in Table 5.5. Such boundary conditions allowed nodes 3 and 4 to move in the x direction and compress or extend the element. The nodes 2 and 3 were allowed moving in the y direction so that the Poisson's effect (contraction and expansion transverse to the loading direction) were correctly modelled. The load was introduced in the element by applying a prescribed velocity to the nodes 3 and 4, as shown by the green arrows in Figure 5.6 which is representative of the compression load case. For the tensile load case the prescribed velocity was applied in the opposite direction. The velocity was fixed to 0.01 m/s and to define the strain rate to be simulated the parameter RATESCALE was changed accordingly. Such parameter allows to gradually increase the applied velocity from 0 to the desired value. Thus, it was possible to obtain a stable model. For example, to simulate a strain rate of $10\,\mathrm{s}^{-1}$, the RATESCALE was set equal to 10.

In PAM-CRASH ply model type 1, the failure under compression is defined by two strain values. The first one is the initial failure strain ε_i^{fc}, which is the strain value at which the stress-strain compression curve starts decreasing. The second one is the ultimate failure strain ε_u^{fc}, which is the strain value where complete failure is obtained. Figure 5.7a is representative of this behaviour. As it is possible to see, between these two strain values the damage parameter increases. As shown in Figure 5.7b it was observed that if the parameter ε_u^{fc} was omitted in the material card, after the initial failure the element would still be able to carry load and the stress would increase. This was not representative of the test results, at failure test results showed sudden drop in the stress-strain curve. Therefore, the ultimate failure strain was chosen very close to the initial failure strain. This allowed obtaining a more reliable failure point. A drop in the stress-strain curve was observed once the initial failure strain was reached.

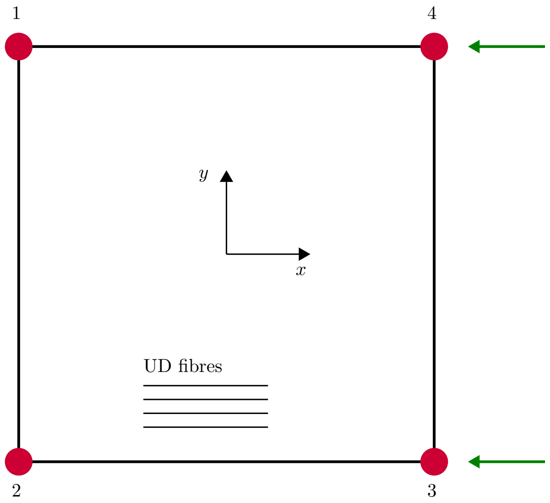

Figure 5.6: Single element calibration model.

Table 5.5: Single element calibration model boundary conditions.

Node ID	Boundary Conditions		
	x	y	z
1	fixed	fixed	fixed
2	fixed	free	fixed
3	free	free	fixed
4	free	fixed	fixed

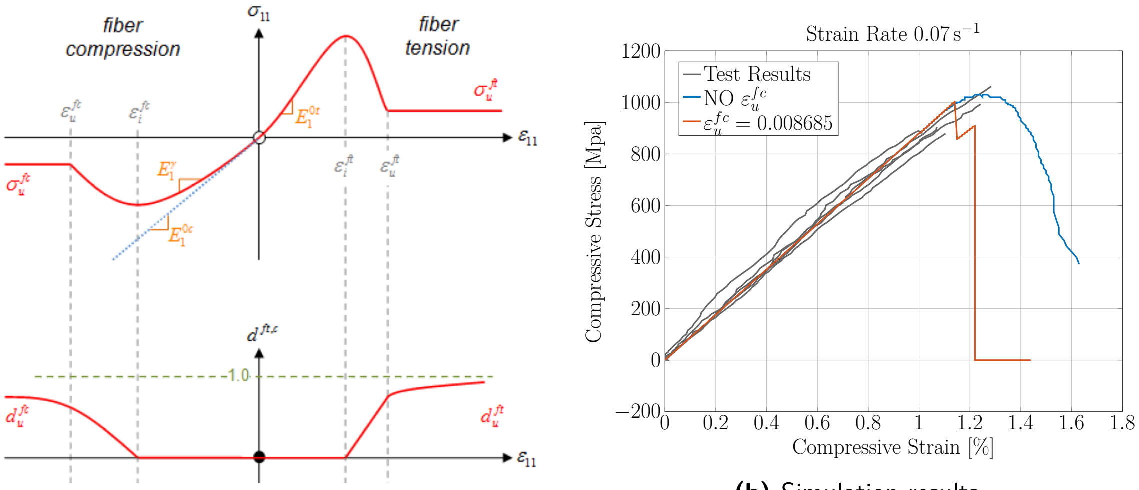

(a) Compressive and tensile fibre damage [27].

(b) Simulation results.

Figure 5.7: Effect of the initial and ultimate failure strain on the single element calibration model.

The stress-strain curves obtained from the single element calibration model are shown in Figure 5.8. Both the curves obtained for the compression and the tensile simulation are displayed. From Figure 5.8a it is possible to see that the compressive strength and failure strain increased with increasing strain rate. The curves showed the same inclination as no strain rate effect was imposed on the compressive and tensile modulus. Figure 5.8b shows the results obtained for the tensile properties. Thanks to the use of the Yamada-Sun criterion the simulation of the tensile tests showed no strain rate effects on the tensile modulus and on the tensile fracture strain.

The single element calibration compressive results are shown in Figure 5.9 and summarised in Table 5.6. It is possible to see from Figure 5.9a that the simulation results slightly overestimate the compressive strength at the low strain rates and slightly underestimate it at the high strain rates. As expected both the failure strain and the compressive strength show a linear increasing behaviour with the logarithm of the strain rate. In Table 5.6 the relative error is also computed for both the compressive failure strain and the compressive strength. It was always lower or approximately equal to 5 %. The differences in the simulation and test results are due to the scatter in the compressive Young's modulus as presented by Schmack et al. [14]. It was therefore decided for the simulation to keep the compressive Youngs modulus independent from the strain rate and equal to 88 GPa. Another source of error was the fact that in some cases the strain rate was not exactly the same between the simulation and the test results, giving a slightly different response in the simulation.

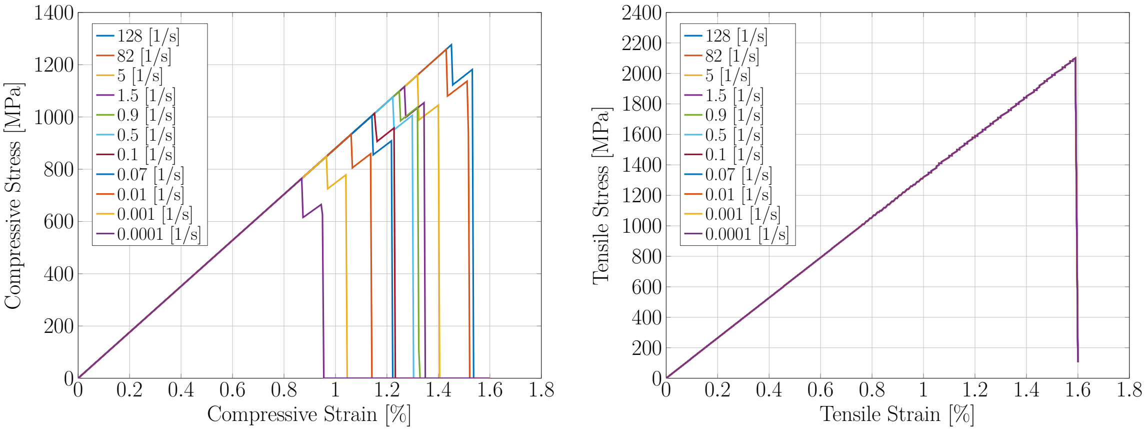

(a) Compression

(b) Tension

Figure 5.8: Stress-strain curves of the single element calibration model

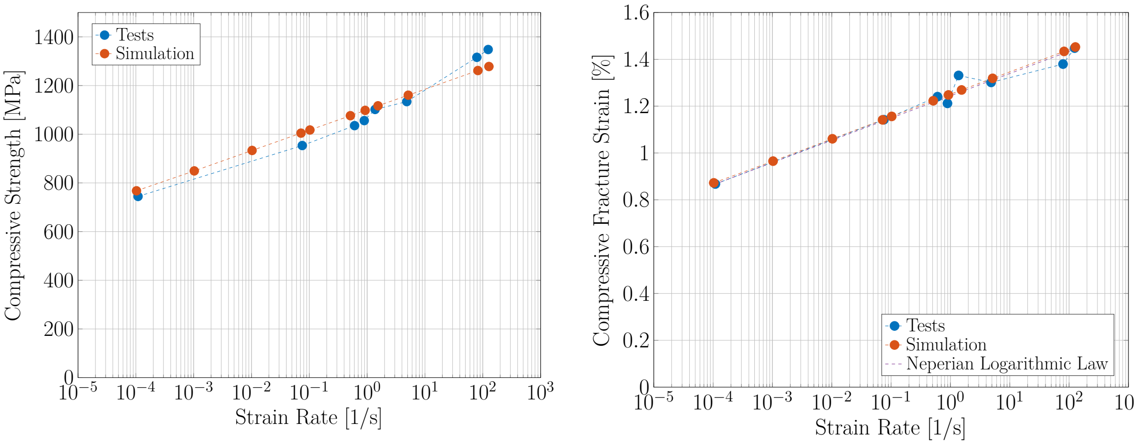

(a) Compressive strength

(b) Compressive fracture strain

Figure 5.9: Comparison of the compressive fracture strain and strength between the simulation and the test results.

Table 5.6: Comparison of test results and material card calibration.

Test			Simulation			Relative Error	
Strain Rate [s^{-1}]	Failure Strain [%]	Compressive Strength [MPa]	Strain Rate [s^{-1}]	Failure Strain [%]	Compressive Strength [MPa]	Failure Strain [%]	Compressive Strength [%]
0.000109	0.868	745	0.000102	0.872	768	0.56	3.09
0.07	1.142	954	0.07	1.142	1005	0.05	5.35
0.61	1.241	1035	0.51	1.223	1076	-1.42	3.96
0.89	1.212	1056	0.92	1.248	1098	2.97	3.98
1.37	1.331	1102	1.54	1.269	1117	-4.66	1.36
4.85	1.301	1134	5.14	1.319	1160	1.38	2.29
79	1.380	1326	82	1.434	1262	3.91	-4.83
124	1.448	1348	128	1.453	1278	0.35	-5.19

5.5 3-Point-Bending Simulation Model

The 3-point-bending simulation model was created using the bending model currently used by Audi for quasi-static simulations as a reference. The quasi-static model was used to understand the implementation of such a model and to select the correct parameters for modelling the contact between the specimen and the fixture components (the impactor and the two supports), and to obtain the required outputs.

The simulation model created is shown in Figure 5.10. The two supports and the impactor were modelled by only defining their outer surface. They were designed as cylinders with the radius of 5 mm. Therefore, shell elements were used to mesh these parts. The material used for the impactor and the two supports was steel, with a Young's modulus of 210 MPa and a poisson ratio of 0.3. The specimen was meshed using square shell elements with a side of 5 mm. Therefore, the specimen mesh resulted in 60 elements and 84 nodes. As material model 131 was used the number of integration points through the thickness was one for each ply. Thus the number of integration points changed according to each specimen thickness, as with increasing thickness the number of plies increased.

The boundary conditions were of importance to correctly simulate the bending test. The two supports were fixed in their position, while the specimen was placed on the top of them. The specimen was free to move in the space, as it was necessary for it to slide on supports during the test simulation. The specimen was placed in the middle of the supports and, as it was defined only by its mid-plane surface, it was placed at distance equal to half its thickness from the supports. This ensured that the specimen was in the simply supported conditions at the start of the simulation. The impactor was only allowed to move in the vertical direction z. To define its motion a velocity was imposed to it so that it would move towards the specimen. The testing velocity of the impactor could be changed, so that it would be possible to replicate all the tests performed. Model convergence was obtained for strain rate testing conditions using an INIT_MASS_SCALL value of 0.0002.

To make the positioning of the model components easier, a python code was used to define the components position according to the reference system origin. The code is shown in Figure 5.11. By defining the specimen thickness and the support span, the position of the supports, the specimen, and the impactor was changed accordingly.

Simulations were performed for all combinations of specimen thickness, support span and impactor velocity used during testing. The results were analysed in terms of contact force between the impactor and the specimen, and in term of maximum displacement of the node at the specimen mid-point.

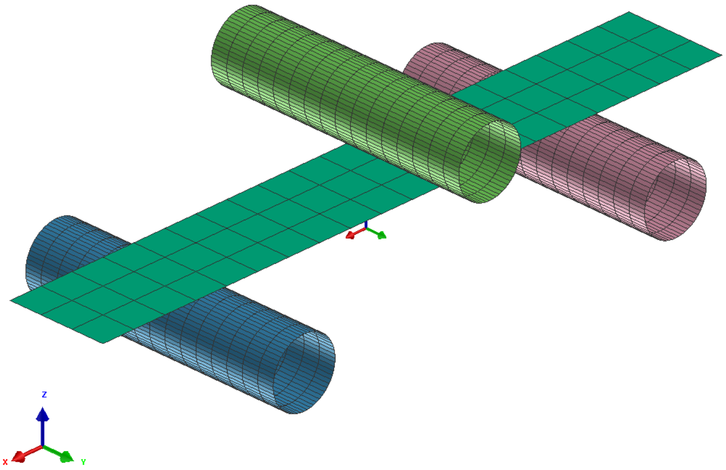

Figure 5.10: The 3PB simulation model implemented.

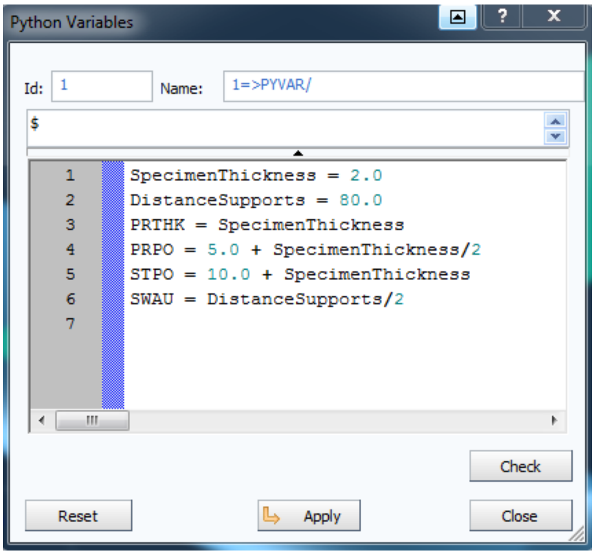

Id: 1

Name: 1=>PYVAR/

```
SpecimenThickness = 2.0
DistanceSupports = 80.0
PRTHK = SpecimenThickness
PRPO = 5.0 + SpecimenThickness/2
STPO = 10.0 + SpecimenThickness
SWAU = DistanceSupports/2
```

Figure 5.11: Python code for the parametric model.

5.5.1 Maximum Force

The simulation of the quasi-static tests imposed the impactor to move with a velocity of 3.3×10^{-5} m/s. Due to this low velocity and the small time step of the model this resulted in a very high computation time. It was tried to use the RATESCALE parameter to reduce the simulation time by increasing the piston velocity, without altering the testing strain rates. This solution did not lead to successful results.

The maximum contact force between the specimen and the impactor is summarised in Figure 5.12. In particular, Figure 5.12a summarises the data from the simulations performed with the 80 mm support span, while Figure 5.12b displays the data from the simulations performed with the 60 mm support span. For each specimen thickness, the bar plots display the maximum load reached at every velocity tested. As expected, the simulation results show an increase in maximum force with the increase in specimen thickness, this is due to the increase of the specimen global stiffness. With the increase of the impactor velocity the simulation results show an increase of the maximum force at failure, only for some specimen thickness the results at the two highest velocities are not following the increasing trend. This behaviour was also observed during test results and it was inferred that is was due to increasing specimen vibrations with increasing testing velocity.

5.5.2 Maximum Displacement

The maximum specimen midpoint displacement at failure is summarised in Figure 5.13. Figure 5.13 is representative of the data from the simulations performed with the 80 mm support span, while Figure 5.13b displays the data from the tests performed with the 60 mm support span. The simulation results show a decrease in maximum displacement with the increase of the specimen thickness. As already observed for the maximum force, also the specimen midpoint displacement increases with the increase of the testing speed.

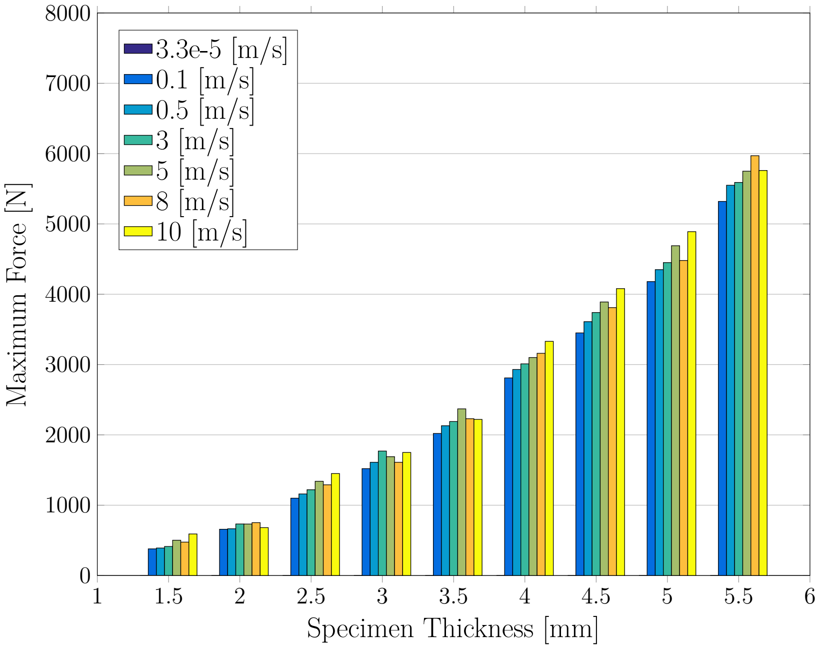

(a) Support span= $80\,\mathrm{mm}$

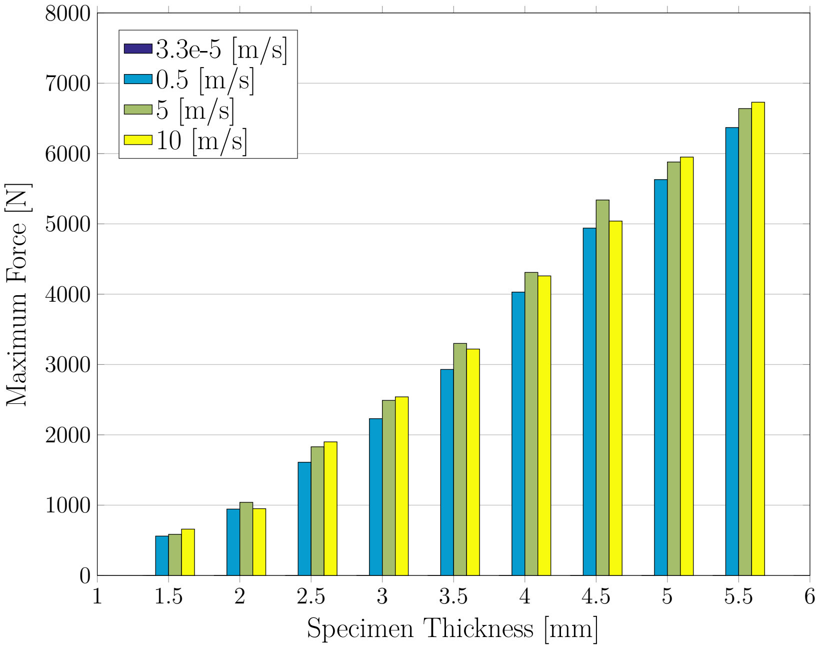

(b) Support span $= 60\,\mathrm{mm}$

Figure 5.12: Maximum force from the 3PB simulation model.

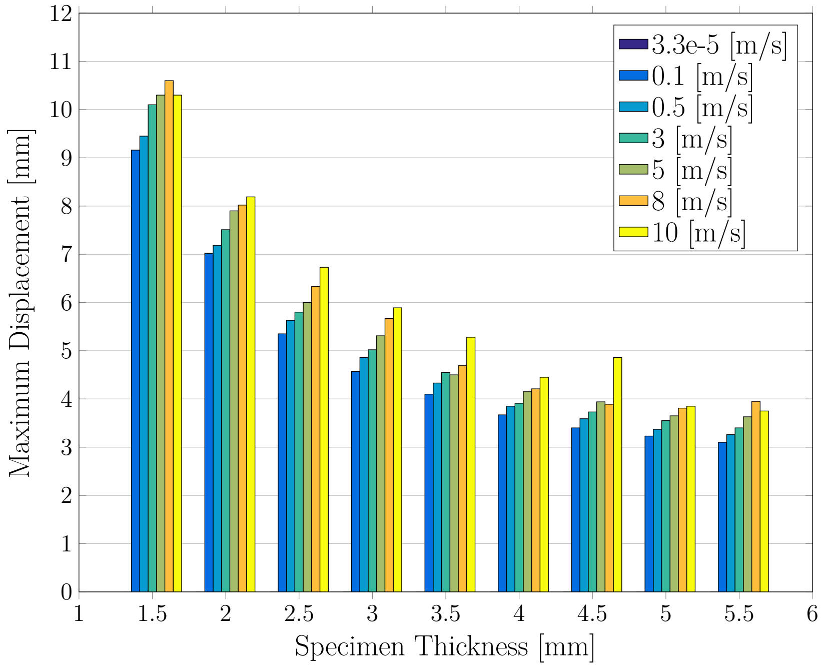

(a) Support span= $80\,\mathrm{mm}$

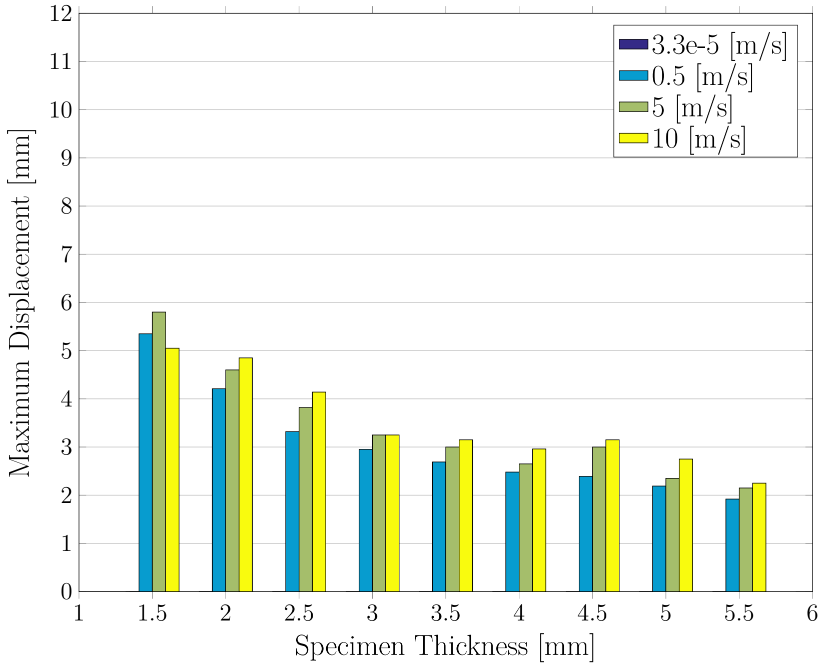

(b) Support span $= 60\,\mathrm{mm}$

Figure 5.13: Maximum displacement from the 3PB simulation model.

5.5.3 Comparison with Test Results

The maximum force and the maximum displacement obtained from the simulations were compared with the results obtained from tests, which were presented in Chapter 3. The comparison is here presented in terms of relative error between the simulation and the tests. The relative error was computed as

$$\text{relative error} = \frac{\text{simulation result} - \text{test result}}{\text{test result}}$$

Figure 5.14 is representative of the relative error of the maximum force, while Figure 5.15 is representative of the relative error of the maximum midpoint displacement. The relative error for both the maximum force and the maximum displacement is lower for the support span of 60 mm. For both support spans, a general trend was observed: the simulation results for both the maximum force and the maximum displacement are lower than the test results for low specimen thickness values, and the the simulation results for both quantities analysed are higher than the test results for specimen thickness values higher or equal to 3.5 mm. This behaviour demonstrates that the specimen stiffness of the simulation model is different from the one of the specimen tested. A reason could be that the stiffness value estimated from the strain rate dependent compression test used to calibrate the material card was underestimated. Furthermore, a reason for the difference between the simulation and the test results could be the fact that the simulation did not take into account the strain rate dependency of the shear properties. This limitation and the high computation time for the quasi-static test should be addressed in future works.

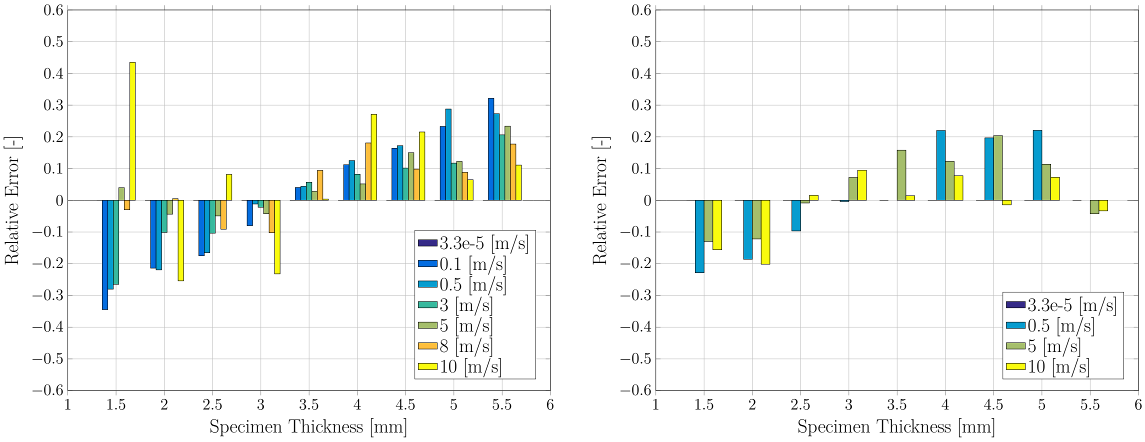

(a) Support span $= 80\,\mathrm{mm}$

(b) Support span $= 60\,\mathrm{mm}$

Figure 5.14: Relative error between simulation and test results for the maximum force.

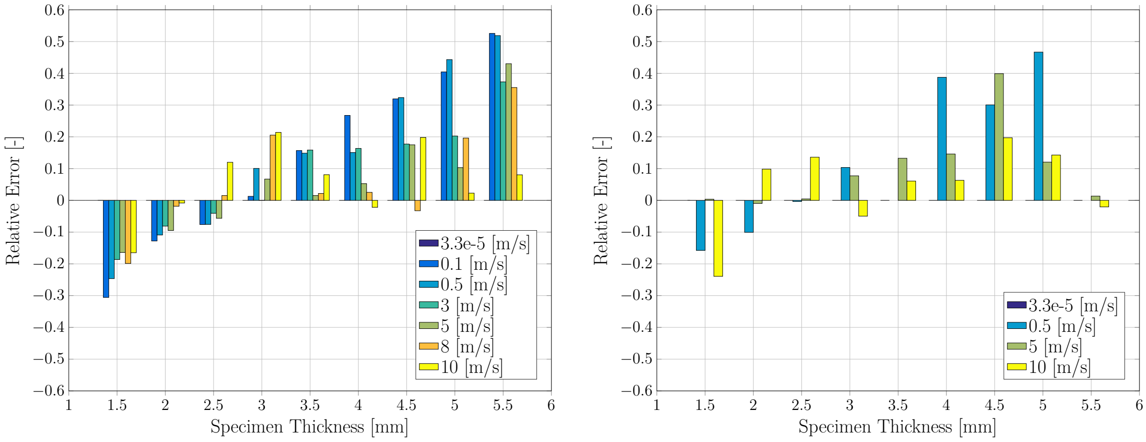

(a) Support span = 80 mm **(b)** Support span = 60 mm

Figure 5.15: Relative error between simulation and test results for the maximum displacement.

5.6 Conclusions

In this section the conclusions based on the content of this chapter are drawn. The implementation of the strain rate dependent properties in the composite material card has been described in detail. The single element calibration of the strain rate dependent compressive properties has been presented. Finally, the 3PB simulation model has been described and its results have been compared with the test results.

Ply model type 1 was used in the simulation to model the UD composite material. Despite the fact that it does not make a distinction between the tensile and the compressive strain rate dependent behaviour, the use of the Yamada-Sun failure criterion already implemented in PAM-CRASH allowed enforcing the tensile failure at the quasi-static failure strain, as shown in Figure 5.8b. The Neperian logarithmic law was used to fit the strain rate dependent compressive failure strain obtained from tests. This allowed obtaining the fitting coefficients needed by the material card in order to take into account the strain rate effect on the compressive fracture strain. The single element calibration showed a good accordance with the test results, both in terms of compressive fracture strain and strength, as shown in Figure 5.9.

The 3PB simulation model was implemented. For each combination of specimen thickness and support span the simulation results showed a general increasing trend of the maximum force and maximum displacement at failure. It can be inferred that the model correctly represents the increase in maximum force and maximum displacement with increasing impactor velocity. On the other hand, by comparing the simulation results with the test results, it was observed that the simulation model underestimated the maximum force and the maximum displacement for the low thicknesses, while the two quantities were overestimated for specimen thicknesses higher or equal to 3.5 mm. This behaviour suggests a lower specimen stiffness of the simulation model. It could be due to a low estimate of the compressive modulus from the strain rate dependent compressive tests used to calibrate the material card. The high relative

error could be also due to the fact that no strain rate effect was implemented for the shear properties.
Issues were encountered with the simulation of the quasi-static tests. Due to the low impactor velocity and the low time step required for the model convergence, the simulation resulted in being highly computational expensive. This issue and the import of the shear strain rate properties in the material card should be addressed in a future work to improve the 3PB simulation model.

In conclusion, this work was the first inside Audi which has taken into consideration strain rate dependent compression properties of the composite material used. The work has shown that a successful calibration of such properties was obtained. On the other hand, the strain rate dependent 3PB simulation model showed limitations and the high relative error suggests that it cannot yet be used for validation of strain rate dependent material cards. There is therefore room of improvement, for example the strain rate effect on shear properties should be taken into account. To reduce the computational time of the simulations that replicate quasi-static conditions the parameters INIT_MASS_SCALL and DYNA_MASS_SCALL could be increased. This would increase the simulation time steps and therefore the total time of the simulation would be reduced. Using this method the total mass of the model is increased and a convergence analysis is required to determine whether the mass increase affects the simulation results. However, it is important that the increase in the time step does not affect the model convergence for the high testing velocity.

Chapter 6

Conclusions and Recommendations

6.1 Conclusions

This thesis has studied strain rate dependent material properties of a UD carbon/epoxy composite. The focus has been on the flexural properties of the composite under dynamic 3PB tests. Such properties have been investigated both through tests and simulations. This section concludes the study by answering the research questions initially presented in Section 2.4.

1- *Since UD CFRPs show strain rate dependent compressive and shear behaviour, is this behaviour also displayed during strain rate dependent 3-point bending tests?*

This first research question can be answered positively, as it was observed that the load and midpoint displacement at failure increased with increasing testing velocity. Tests were performed using a servo-hydraulic testing machine from INSTRON. As the laboratory was not provided with a fixture to perform bending tests with that machine, a fixture was designed. No accepted standards are available for rate-dependent testing of composites, therefore the fixture design followed the guidelines given by the quasi static norm DIN EN ISO 14125 [31]. The resulting design was a fixture with a radius of 5 mm which used strain gauges in the impactor and the two supports to measure the load applied on the tested specimen. The specimens were painted with a greyscale stochastic pattern, which allowed tracking the specimen midpoint displacement in the post processing of the pictures taken by two high speed cameras, using the DIC software ARAMIS®.

The combined use of the specimen midpoint displacement and the load signal obtained from the fixture allowed analysing the specimen response in terms of force-midpoint displacement curves. Of importance was the choice of the failure point at which the maximum load and the maximum midpoint displacement were measured. The analysis of pictures taken with the high speed cameras showed that, failure started with fibre kinking on the compressive side for all the specimens. This point corresponded to a flattening of the force-displacement curve. Depending on the specimen thickness, the final failure was either tensile fibre failure or delamination. As the load did not increase after initial fibre kinking, the maximum load and the maximum midpoint displacement were measured when fibre kinking occurred. Both quantities showed an increasing trend with increasing testing velocity. For every combination of specimen thickness and support span tested the increase of maximum load of the dynamic tests compared to the corresponding quasi-static one was of at least 20 %.

Detachment between the specimen and the impactor was observed after the initial impact between the two bodies, especially at high testing speeds. This factor induced specimen vibrations which led to variation in the test results. It was observed that by increasing the specimen thickness or by reducing the support span the initial detachment reduced. The latter option was the one which led to a low detachment also at high testing speeds. This was due to a higher increase of the specimen global stiffness when reducing the support span compared to increasing the specimen thickness. The variation of the test results due to specimen vibrations was analysed using the coefficient of variance (CV). The analysis showed that for the force measurements the CV showed a minimum for both support spans tested. The minimum was reached for specimens 5 mm thick for the support span of 80 mm and for specimens 4.5 mm thick for the support span of 60 mm. In general a lower CV was obtained for tests performed with the support span of 60 mm.

As the CV showed an increasing trend with increasing testing velocity, a method to estimate the maximum testing velocity below which test results showed low variation was implemented. The implemented method showed that the coefficient of determination of a linear regression of the test results decreased with increasing testing velocity. A Matlab® GUI based on the test results was implemented to estimate the maximum testing velocity for any specimen with a specific global stiffness

2- *Can the strain rate dependent material model implemented in the finite element software PAM-CRASH describe correctly the behaviour of the material shown during testing?*

The second research question can be partially answered positively. The strain-rate dependent compressive properties were successfully imported in PAM-CRASH. The single element calibration model could correctly estimate the compressive failure strain and the compressive strength at any strain rate. Thanks to the use of the Yamada-Sun criterion available in ply model type 1, also the tensile behaviour was correctly simulated as no changes in the tensile Young's modulus and the tensile failure strain were observed. The 3PB simulation model implemented was able to correctly simulate the increasing trend of the maximum force and of the maximum displacement at failure with the increase of the testing speed. However, the maximum force and the maximum displacement were underestimated for specimens with low thickness and overestimated with specimens with high thickness. Due to the low impactor velocity for the simulation of quasi-static tests, the implemented model resulted in high computational effort. The method used to reduce the computational time did not lead to successful results.

In conclusion, this study implements a method to validate the material cards, which take into account strain rate dependent properties of composite materials. The literature review has shown that there is no accepted standard for rate-dependent testing of composites. The research performed in this thesis evaluated the 3-point bend test in order to determine the optimum parameters (specimen thickness and support span) to measure reliable data from the test setup. This thesis has then used the data obtained to validate a material card in the FE model which take into account strain rate dependent material properties. While there is scope for further improvements, the research performed in this thesis contributes to the identification of more accurate material cards to be used for simulation of vehicles crash tests. The following section provides recommendations on how the work could be further improved.

6.2 Recommendations

The research carried out in this thesis was the first performed on the topic of dynamic 3PB tests and on the implementation of simulation models that take into account strain rate dependent properties of composites at Audi AG. The analysis could be enhanced through improvements in both the test setup and the simulation model, which could be implemented with further research. The hereafter recommendations have been divided in topics of main interest.

Tests setup The calibration process of the test setup could be enhanced. The camera lenses used, the distance of the cameras from the tested specimen and the use of a small measuring volume made it difficult to obtain the cameras calibration. A reduction in the distance between the cameras and the specimen, and the use of lenses with a lower focal length would make the calibration process easier. Alternatively, cameras with a higher resolution could be used. In addition, in order to make it easier for ARAMIS® to track the impactor, measuring points with a smaller diameter could be used.

Estimation of the Maximum Testing Velocity Three further improvements could enhance the estimation of maximum testing velocity. Firstly, further investigation is required to determine the global stiffness threshold after which the estimated maximum testing velocity shows a decreasing trend. This should be done for both support spans tested. Secondly, it could be determined whether the maximum estimated testing velocity increases linearly with the reduction of the support span. In order to determine this, tests should be performed with at least a third different support span. Finally, if tests were performed with different specimen layups and composite materials, a database could be created to allow the estimation of the testing velocity for each specific material tested using the Matlab® GUI.

Simulation model Two further improvements could be made to the simulation model. Firstly, strain-rate dependency of the shear properties could be included in the material card. This would allow to fully characterise the strain-rate dependent behaviour of the composite and obtain more realistic results. Secondly, the 3PB model could be modified to reduce the computational time of quasi-static test. This could be achieved with two possible methods: one option requires adjusting the RATESCALE parameter to increase the testing speed without affecting the quasi-static testing strain-rate, the second option requires increasing the initial mass scale and the dynamic mass scale parameters which lead to a higher time step. However, the increase in parameters under the second method would lead to a higher mass to the model, therefore it would need to be checked that the simulation results are not affected by the mass increase.

References

[1] European Commission. *http://ec.europa.eu/clima/policies/transport/vehicles/cars_en*.

[2] Euro NCAP. *The European New Car Assessment Programme*, *http://www.euroncap.com/en*.

[3] Department of Defence. *Composite Materials Handbook MIL-HDBK-17-1F*, 2002.

[4] J. Harding and L. M. Welsh. A tensile testing technique for fiber-reinforced composites at impact rates of strain. *Journal of Materials Science*, 18(6):1810–1826, 1983.

[5] Y. X. Zhou, D. Z. Jiang, and Y. M. Xia. Tensile mechanical behavior of t300 and m40j fiber bundles at different strain rate. *Journal of Materials Science*, 36(4):919–922, 2001.

[6] Y. X. Zhou, Y. Wang, S. Jeelani, and Y. M. Xia. Experimental study on tensile behavior of carbon fiber and carbon fiber reinforced aluminum at different strain rate. *Applied Composite Materials*, 14(1):17–31, 2007.

[7] N. Taniguchi, T. Nishiwaki, and H. Kawada. Tensile strength of unidirectional cfrp laminate under high strain rate. *Advanced Composite Materials*, 16(2):167–180, 2007.

[8] A. Gilat, R. K. Goldberg, and G. D. Roberts. Experimental study of strain-rate-dependent behavior of carbon/epoxy composite. *Composites Science and Technology*, 62(10-11):1469–1476, 2002.

[9] D. Hull. Matrix-dominated properties of polymer matrix composite-materials. *Materials Science and Engineering: A*, 184(2):173–183, 1994.

[10] H. M. Hsiao and I. M. Daniel. Strain rate behavior of composite materials. *Composites Part B: Engineering*, 29(5):521–533, 1998.

[11] H. M. Hsiao, I. M. Daniel, and R. D. Cordes. Strain rate effects on the transverse compressive and shear behavior of unidirectional composites. *Journal of Composite Materials*, 33(17):1620–1642, 1999.

[12] M. V. Hosur, J. Alexander, U. K. Vaidya, and S. Jeelani. High strain rate compression response of carbon/epoxy laminate composites. *Composite Structures*, 52(3âĂŞ4):405–417, 2001.

[13] H. Koerber and P. P. Camanho. High strain rate characterisation of unidirectional carbon-epoxy im7-8552 in longitudinal compression. *Composites Part A: Applied Science and Manufacturing*, 42(5):462–470, 2011.

[14] T. Schmack, D. Huelsbusch, R. Righi, J. Rausch, D. Roquette, G. Deinzer, and F. Walther. Influence of load application and fixture on characteristic values at short-time dynamic compression testing of carbon fiber-epoxy composites. *Paper Presented at the 17th European Conference on Composite Materials*, 2016.

[15] H. Koerber, J. Xavier, and P. P. Camanho. High strain rate characterisation of unidirectional carbon-epoxy im7-8552 in transverse compression and in-plane shear using digital image correlation. *Mechanics of Materials*, 42(11):1004–1019, 2010.

[16] I. M. Daniel, B. T. Werner, and J. S. Fenner. Strain-rate-dependent failure criteria for composites. *Composites Science and Technology*, 71(3):357–364, 2011.

[17] H. Cui, D. Thomson, A. Pellegrino, J. Wiegand, and N. Petrinic. Effect of strain rate and fibre rotation on the in-plane shear response of Âś45Âř laminates in tension and compression tests. *Composites Science and Technology*, 135:106–115, 2016.

[18] E. V. Morozov and V. A. Thomson. Simulating the progressive crushing of fabric reinforced composite structures. *Composite Structures*, 76(1-2):130–137, 2006.

[19] B. P. Bussadori, K. Schuffenhauer, and A. Scattina. Modelling of cfrp crushing structures in explicit crash analysis. *Composites Part B-Engineering*, 60:725–735, 2014.

[20] André F. B. P. Pinto, S. M. O. Tavares, José M. A. César de Sá, and P. M. S. T. de Castro. Structural analysis of a cross car beam using finite element models. *International Journal of Structural Integrity*, 6(6):759–774, 2015.

[21] C. M. Kindervater, A. F. Johnson, D. KohlgrÃijber, M. LÃijtzenburger, and N. Pentecote. Crash and impact simulation of aircraft structures âĂŞ hybrid and fe based approaches. *Paper Presented at European Congress on Computational Methods in Applied Sciences and Engineering*, 2000.

[22] A. Chawla, S. Mukherjee, D. Mohan, D. Bose, P. Rawat, T. Nakatani, and M. Sakurai. Fe simulations of motorcycle-car frontal crashes, validations and observations. *International Journal of Crashworthiness*, 10(4):319–326, 2005.

[23] S. Xilong, W. Dengfeng, and L. Fang. Structure improvement and experiment validation for a car side impact. *Applied Mechanics and Materials*, 224:133–137, 2012.

[24] M. A. McCarthy, J. R. Xiao, N. Petrinic, A. Kamoulakos, and V. Melito. Modelling of bird strike on an aircraft wing leading edge made from fibre metal laminates âĂŞ part 1: Material modelling. *Applied Composite Materials*, 11(5):295–315, 2004.

[25] H. Daiyan, F. Grytten, E. Andreassen, H. Osnes, and O. V. Lyngstad. Numerical simulation of low-velocity impact loading of a ductile polymer material. *Materials & Design*, 42:450–458, 2012.

[26] O. Tomlin and N Reynolds. Validation of a thermoplastic composite material model for low carbon vehicle application. *Paper Presented at the 9th Eurepeand LS-DYNA Conference*, 2013.

[27] PAM-CRASH/PAM-SHOCK FE Code. Engineering systems international (esi), f-94578 rungis cedex, france.

[28] P. Ladeveze and E. LeDantec. Damage modelling of the elementary ply for laminated composites. *Composites Science and Technology*, 43(3):257âĂŞ267, 1992.

[29] J. Robinson. A single element test. *Computer Methods in Applied Mechanics and Engineering*, 7(2):191–200, 1976.

[30] F. Kunkel, F. Becker, and S. Kolling. Mechanical characterization of talc particle filled thetmoplastics. *Paper Presented at the 8th European LS-DYNA Conference*, 2011.

[31] DIN EN ISO 14125. *Fibre-reinforced plastic composites – Determination of flexural properties*, 1998.

[32] F. Mujika, N. Carbajal, A. Arrese, and I. Mondragon. Determination of tensile and compressive moduli by flexural tests. *Polymer Testing*, 25(6):766–771, 2006.

[33] B. C. W. van der Vossen. *Spatial Variability of Stiffness in Fiber Reinforced Composites in Short Beam Shear Test Specimens.* Msc, 2014.

[34] A. P. Carpentier. Advanced material characterisation based on full field deformation measurements. *PhD Thesis. The University of Texas at Arlington*, 2013.

[35] J. M. Lifshitz, F. Gov, and M. Gandelsman. Instrumented low-velocity impact of cfrp beams. *International Journal of Impact Engineering*, 16(2):201–215, 1995.

[36] S. Sánchez-Sáez, E. Barbero, and C. Navarro. Analysis of the dynamic flexural behaviour of composite beams at low temperature. *Composites Science and Technology*, 67 (11âĂŞ12):2616–2632, 2007.

[37] S. R. Hallett. Three-point beam impact tests on T300/914 carbon-fibre composites. *Composites Science and Technology*, 60(1):115–124, 2000.

[38] J. Wiegand. Constitutive modelling of composite materials under impact loading. *D.Phil Thesis. University of Oxford*, 2008.

[39] T. Schmack. *Entwicklung von Methoden fur die Hochgeschwindigkeitsprufung von Faserverbundkunststoffen.* Thesis, 2015.

[40] GOM. *ARAMIS User Manual - Software*, 2016.

[41] TORAYCA. 2016.

[42] DELTAtech. *DT120 Versatile High Toughness Epoxy Matrix - Technical Data Sheet*, 2015.

[43] SSAB. *Toolox in mechanical engineering – Data sheet*, 2016.

[44] Tokyo Sokky Kenkyujo. *BTM series Bolt strain gauges – Data sheet*, 2016.

[45] Vishay Micro-Measurements. *2300 System – Signal Conditioning Amplifiere – 2310B Instruction Manual*, 2009.

[46] ISO 7500-1. *Metallic materials âĂŤ Calibration and verification of static uniaxial testing machines âĂŤ Part 1: Tension/Compression âĂŤ Calibration and verification of the force-measuring system*, 2015.

[47] N. Carbajal and F. Mujika. Determination of compressive strength of unidirectional composites by three-point bending tests. *Polymer Testing*, 28(2):150–156, 2009.

[48] C. Kassapoglou. *Design and Analysis of Composite Structures : with Applications to Aerospace Structures*. Wiley, New York :, 2nd ed. edition, 2013.

[49] A. Quarteroni and F. Saleri. *Calcolo scientifico: esercizi e problemi risolti con MATLAB*. Springer-Verlag, Milan, 4 edition, 2008.

[50] P. Rozycki. *Contribution au développement de lois de comportement pour matériaux composites soumis à l'impact*. Phd thesis, 2000.

[51] S. E. Yamada and C. T. Sun. Analysis of laminate strength and its distribution. *Journal of Composite Materials*, 12(Jul):275–284, 1978.

[52] A. Puck and H. Schurmann. Failure analysis of frp laminates by means of physically based phenomenological models. *Composites Science and Technology*, 62(12-13):1633–1662, 2002.

Fixture Calibration

Before the test programme was undertaken, the fixture impactor and the two supports were calibrated. The ISO 7500-1 [46] norm was followed in order to calibrate the force measuring system. The fixtures were loaded in compression using a ZWICK ROELL Z100 universal testing machine. The force-time curve given by the testing machine was used as the reference load to calibrate the fixtures.
Three measurement series were performed for each fixture to calibrate it at a specific maximum applied load. The maximum applied load considered was 5 and 35 kN. For each measurement the load displayed by the testing machine and the fixture at 20, 40, 60, 80, and 100 % of the maximum force were noted down. This values allowed creating the calibration table. From these values the relative indication error for each measuring series is obtained as follows

$$\mathrm{q}_1 = \frac{((F_{fixt})_1 - (F_Z)_1)}{(F_Z)_1} \times 100 \quad \mathrm{q}_2 = \frac{((F_{fixt})_2 - (F_Z)_2)}{(F_Z)_2} \times 100 \quad \mathrm{q}_3 = \frac{((F_{fixt})_3 - (F_Z)_3)}{(F_Z)_3} \times 100 \tag{1}$$

The term F_{fixt} is referred to the force measurement given by the fixture component, while the term F_Z is referred to the force measurement given by the testing machine. The subscripts 1, 2 and 3 refer to the values from the three measuring series at each of the five force levels. The relative indication error q is obtained as the average of the three computed values

$$\mathrm{q} = \frac{\mathrm{q}_1 + \mathrm{q}_2 + \mathrm{q}_3}{3} \tag{2}$$

The relative repeatability error b_r is given as the difference between the minimum and the maximum value among q_1, q_2, and q_3.

$$b_r = \mathrm{q}_{max} - \mathrm{q}_{min} \tag{3}$$

Following the limits imposed on certain parameters by the norm, it was possible to determine the class of the fixture measuring system for each percentage of the maximum applied load. The class range is from 0.5 to 3, where 0.5 is the best class. An example of calibration table is shown in Table 2, which refers to the impactor subjected to a maximum force of 5 kN.

The force measured through the fixtures was initially obtained using the following equation, as reported in Chapter 3

$$F = \frac{4\ E\ A}{U_{in}\ A_{WB}\ k\ B} U_{out} = S\ U_{out}$$

To obtain a more reliable conversion factor S_{calib}, a scaling factor (sf) which multiplies the load measured by the fixture F_{fixt} was computed at the maximum applied load as follows

$$\frac{F_Z}{F_{fixt}} = sf \quad \rightarrow \quad F_Z = sf\ F_{fixt} = sf\ S\ U_{out} = S_{calib}\ U_{out} \tag{4}$$

The testing parameters are shown in Table 1

Table 1: Fixtures parameters for force measurements.

Fixture	Max Force [kN]	Input Voltage [V]	Amplification [-]	S_{calib} [N/V]
Impactor	5	5	10000	600.808
Support L				602.824
Support R				601.358
Impactor	35	5	1000	6024.966
Support L				6061.105
Support R				6044.511

An example of force time history for both the measurements obtained through the Zwick testing machine and the fixture is shown in Figure 1. The figure shows the three measurement series for the fixture impactor up to a maximum applied load of 5 kN. The results obtained through the impactor overlap with the measurements given by the universal testing machine.

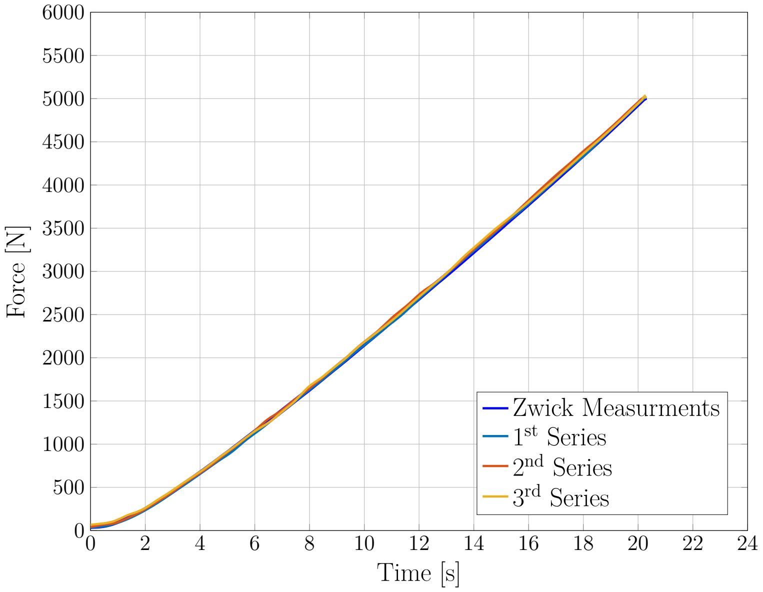

Figure 1: Force-time response for the fixture impactor and the Zwick testing machine.

Table 2: Example of calibration table for the impactor fixture.

Percentage Total Load [%]	1st Measurement Series		2nd Measurement Series		3rd Measurement Series		Mean Values		Standard Deviation	
	Zwick [kN]	Strain Gauge [kN]	Zwick [kN]	Strain Gauge [kN]	Zwick [kN]	Strain Gauge [kN]	Zwick [kN]	Strain Gauge [kN]	Zwick [kN]	Strain Gauge [kN]
0	-	-	-	-	-	-	-	-	-	-
20	-1.0017	-0.99	-1.0035	-1.00	-1.0028	-1.00	-1.0027	-1.00	0.0009	0.0019
40	-2.0023	-2.01	-2.0038	-2.01	-2.0037	-2.01	-2.0033	-2.01	0.0008	0.0043
60	-3.0013	-3.03	-3.0017	-3.01	-3.0039	-3.01	-3.0023	-3.01	0.0014	0.0107
80	-4.0067	-4.02	-4.0016	-4.04	-4.0050	-4.00	-4.0024	-4.02	0.0023	0.0200
100	-5.0015	-5.03	-5.0030	-5.01	-5.0015	-5.03	-5.0011	-5.02	0.0007	0.0084

Percentage Total Load [%]	1st Measurement Error [%]	2nd Measurement Error [%]	3rd Measurement Error [%]	Relative Indication Error - q [%]	Repeatability [%]	Class
-	-	-	-	-	-	-
20	-0.71	-0.74	-0.45	-0.63	0.29	1
40	0.58	0.51	0.14	0.41	0.44	0.5
60	0.80	0.20	0.07	0.35	0.73	1
80	0.41	0.94	-0.15	0.40	1.08	2
100	0.48	0.22	0.48	0.40	0.27	0.5

Strain Rate Computation

In material testing, the strain rate is defined as the rate of the change in the strain with respect to time. In mathematics the rate of change of a function can be obtained by computing it first derivative. Thus, the strain rate can be computed from the material strain using the following equation

$$\dot{\varepsilon}\left(t\right)=\frac{d\varepsilon\left(t\right)}{dt} \tag{5}$$

If the analytical solution for the computation of the strain in the fibre direction for the 3PB test is known, it is possible to use such equation to determine the strain rate using Equation 5. However, if the strain is obtained through discrete measurements, as it is the case for material testing, the strain rate can be obtained from the strain-time diagram by using a numerical approximation of the derivative [49]. Both solutions were used to compute the strain rate of the outer fibre which is subjected to compressive strains. This side was the one chosen as failure is observed in the compressive side, therefore it is more critical.

The ARAMIS analysis gave as output the time history of the minimum compressive strain computed from the surface component. By applying the finite difference method [49] it was possible to obtain the strain rate time history. The strain rate value relative to the test is then obtained as the average of the constant part of the strain rate-time plot.
The ISO 14125 [31] allows to compute the strain of the outer fibre at the specimen midpoint using the equation

$$\varepsilon=\frac{6\ s\ h}{L^2} \tag{6}$$

where s is the specimen midpoint displacement, h is the specimen thickness and L is the support span. Of this quantities the only one that changes through time is the specimen midpoint displacement. The equation can be rewritten as

$$\varepsilon\left(t\right)=\frac{6\ s\left(t\right)\ h}{L^2} \tag{7}$$

The above equation can then be differentiated with respect to time to obtain the strain rate

$$\dot{\varepsilon}\left(t\right)=\frac{d\varepsilon\left(t\right)}{dt}=\frac{d}{dt}\left(\frac{6\ s\left(t\right)\ h}{L^2}\right) \tag{8}$$

The only term that can be differentiated with respect to time is the midpoint displacement $s(t)$. The displacement is a measure of the position of the specimen midpoint through time.

Therefore, as the time derivative of the position is the velocity v of the specimen midpoint the equation can be rewritten as

$$\dot{\varepsilon}\left(t\right) = \frac{d\ s\left(t\right)}{dt}\left(\frac{6\ \ h}{L^2}\right) = \frac{6\ v(t)\ h}{L^2} \quad \rightarrow \quad \dot{\varepsilon} = \frac{6\ v\ h}{L^2} \tag{9}$$

Equation 9 was used to obtain the "analytical" strain rate. The value of v correspond to the average velocity during testing. According to the equation obtained the strain rate increase linearly with the increase of the testing velocity and of the testing speed. The support span influences the strain rate as $1/L^2$, a reduction by half the support span increases the strain rate by four times.

The results obtained for the strain rate on the outer fibre on the compressive side of the specimen using the two approaches described are shown in Figure 2 and Figure 3. The results obtained from the strain measured from ARAMIS are shown presented in Figure 2. In most tests the strain rate showed an increasing behaviour with increasing testing velocity, however the data shows high variation at both support spans and no particular trend could be observed.

Figure 3 is representative of the results obtained using Equation 9. The expected behaviour was shown by the results obtained. At a specific thickness the strain rate increased linearly with the testing velocity, the same was observed when the thickness increased and the testing velocity was constant. At the same thickness and testing velocity, the reduction in the support span gave a strain rate 1.78 times higher. Compared to the results obtained from the ARAMIS analysis the analytical solution gave a lower strain rate. In the ARAMIS analysis the maximum strain rates are in the order of the hundreds, while the analytical solution always predicted a strain rate lower than $100\,\mathrm{s}^{-1}$.

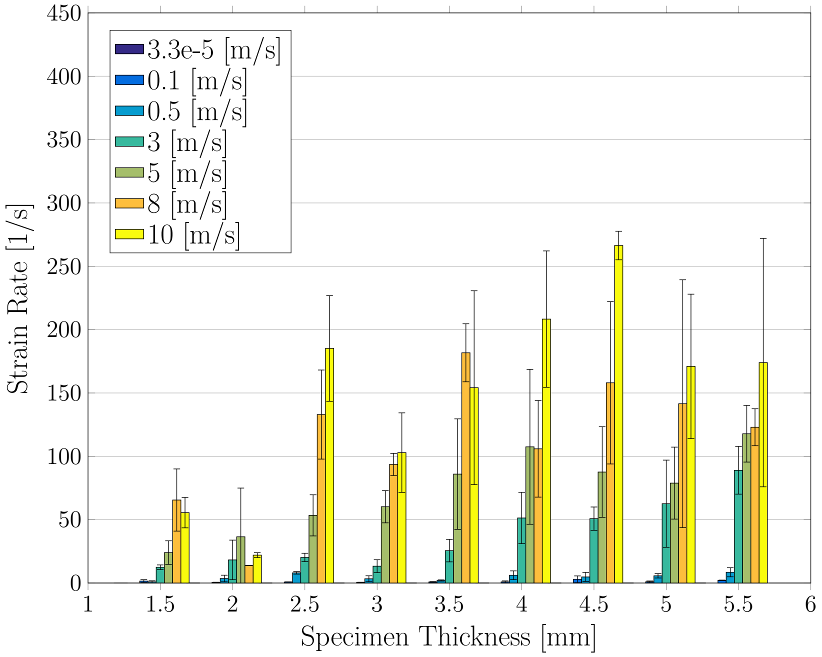

(a) Support span= 80 mm

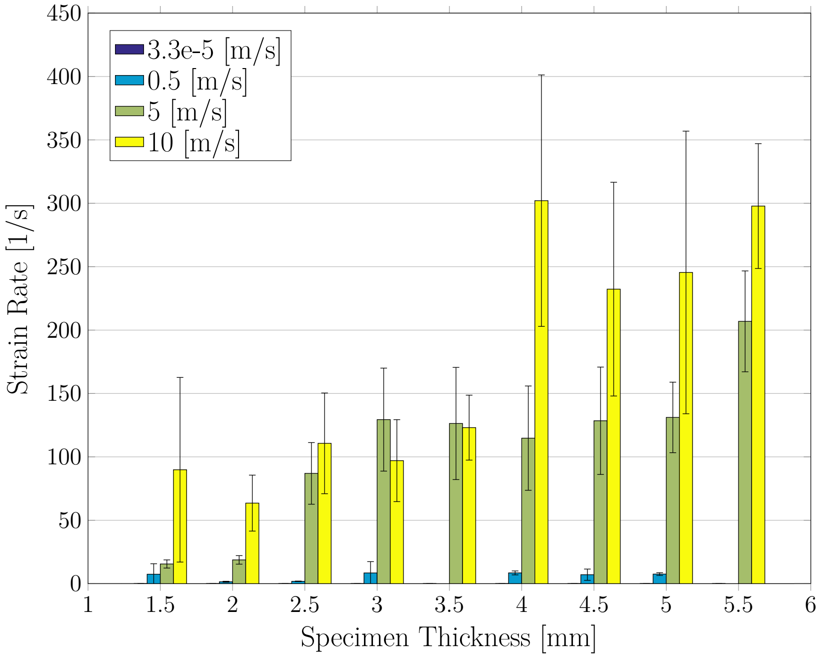

(b) Support span = 60 mm

Figure 2: Strain rate computed from the ARAMIS analysis.

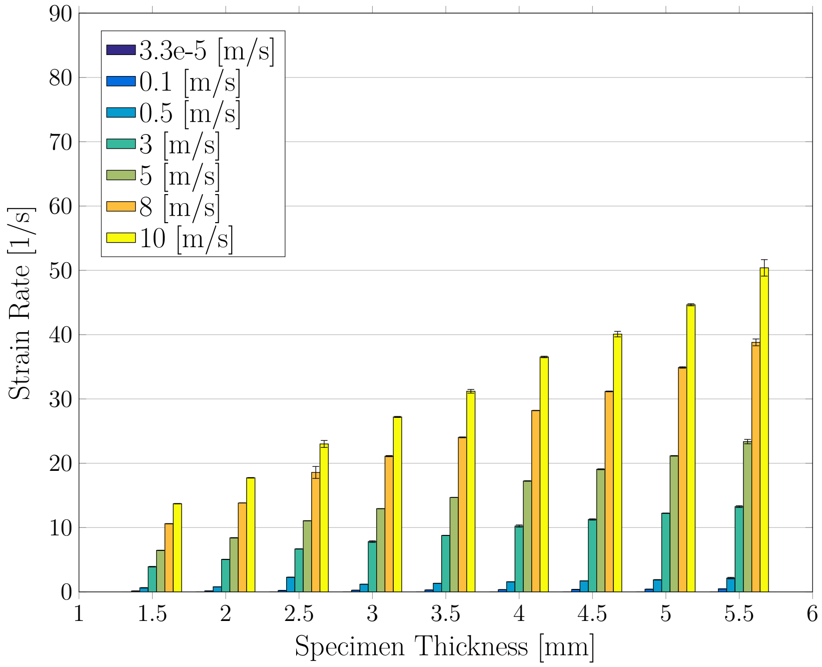

(a) Support span= $80\,\mathrm{mm}$

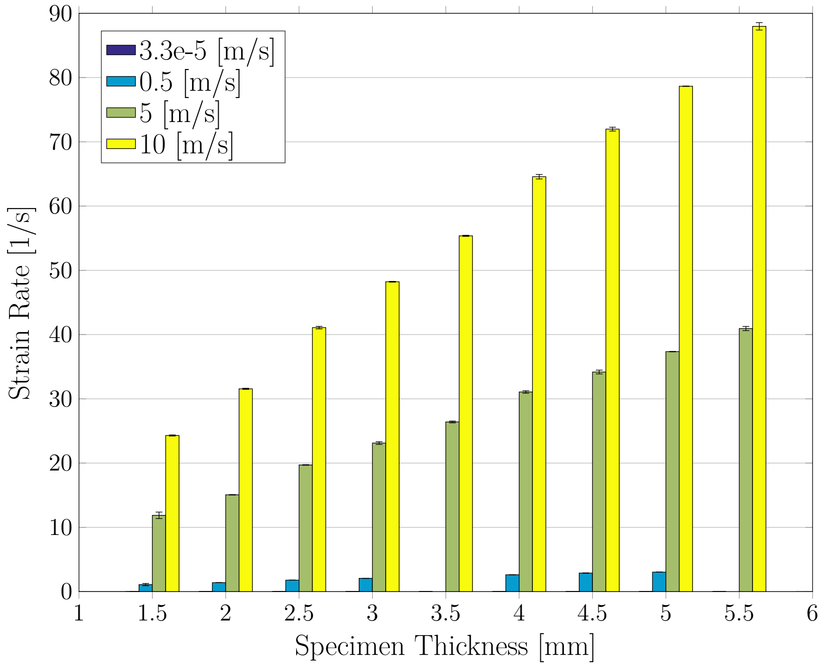

(b) Support span $= 60\,\mathrm{mm}$

Figure 3: Strain rate computed from the analytical analysis.